

---

Diploma Thesis

# Self-complementary antennas for ultrawideband radio systems

---

by

HORIA BOTEZAN

1026549

supervised by

Univ.Prof. Dr.-Ing.

CHRISTOPH MECKLENBRÄUKER

and by

Senior Scientist Dipl.-Ing. Dr.techn.

ROBERT LANGWIESER

at the Institute of Telecommunications of  
TU Wien.

June 7, 2017



# Abstract

In this work self-complementary antennas are studied. This study is restricted to ultrawideband systems. The commercially available ultrawideband systems operate in the frequency band between 3.1 and 10.6 GHz so the ultrawideband antennas are designed for this frequency band of operation. The reason why these type of antennas were chosen is because these structures exhibit a constant impedance and hence a constant reflection coefficient over all frequencies from a theoretical point of view.

In the first chapter an introduction is provided. After a short history of the ultrawideband system and the ultrawideband antennas an overview of a contemporary ultrawideband system is presented. At the end of the chapter the scientific literature that discusses ultrawideband systems relevant for this work are studied.

In the second chapter two principles are presented, preliminary to discussing self-complementary antennas. These principles are the view principle and the self-complementary principle. After the principles are clear, three types of self-complementary antennas together with design methods are presented. The three types are the plane symmetrical, the axis-symmetrical and the rotation symmetrical self-complementary antennas. A design of a microstrip balun is also presented because it is necessary for the rotation-symmetrical self-complementary antennas. These designs are improved afterwards through simulation. At the end of this chapter other ultrawideband antennas that satisfy the complementary principle are discussed.

In the last chapter the realized antenna and microstrip balun prototypes are presented, simulated, manufactured and measured. The reflection coefficient and the gain of the prototypes are measured in an indoor environment using vector network analysis. The microstrip balun is measured using the time domain reflectometry analysis. Additionally some caveats regarding the measurements are discussed, for example the parasitic influence of the SMA connector stubs and the small ground plane on the measurement accuracy. At the end of the chapter time domain measurements are carried out with the purpose of observing the dispersion of the antennas. For this purpose an ultrawideband signal according to the IEEE 802.15.4a standard is designed and realized using a programmable arbitrary waveform generator.

# Kurzfassung

In dieser Arbeit werden selbstkomplementäre Antennen untersucht. Diese Untersuchung ist auf ultrabreitbandige Systeme beschränkt. Die kommerziellen ultrabreitbandigen Systeme werden im Frequenzbereich zwischen 3.1 und 10.6 GHz betrieben. Das Design der ultrabreitbandigen Antennen ist für diesen Frequenzband durchgeführt worden. Diese Art der Antennen wurde gewählt, weil solche Strukturen eine konstante Eingangsimpedanz beziehungsweise einen konstanten Reflexionskoeffizienten im entsprechenden Frequenzband aufweisen.

In dem ersten Kapitel wird die Arbeit eingeleitet. Nach einer kurzen Geschichte der ultrabreitbandigen Systeme und ultrabreitbandigen Antennen wird eine Übersicht über aktuelle ultrabreitbandige Systeme geschaffen. Am Ende dieses Kapitels wird die für diese Arbeit relevante wissenschaftliche Literatur über ultrabreitbandige Systeme analysiert.

In dem zweiten Kapitel werden zwei Prinzipien vorgestellt. Diese sind das Prinzip bezüglich verschiedener Ansichten der Antennenfunktion und das Prinzip der Selbstkomplementarität. Nachdem diese geklärt sind, werden drei Arten selbstkomplementärer Antennen samt Methoden für das Design vorgestellt. Die drei Arten sind die plansymmetrische, die achsensymmetrische und die rotationsymmetrische selbstkomplementäre Antenne. Ein Design eines Baluns in Mikrostreifenleitung-Technologie ist ebenfalls vorgestellt, da dieses für die rotationsymmetrische selbstkomplementäre Antenne notwendig ist. Darauf hin werden diese Designs mittels Simulation verbessert. Am Ende dieses Kapitels werden andere breitbandige Antennen vorgestellt, welche das Prinzip der Selbstkomplementarität erfüllen.

Im letzten Kapitel werden Prototypen der entworfenen Antennen und des Baluns vorgestellt, simuliert, hergestellt und gemessen. Der Reflexionskoeffizient und der Gewinn der Prototypen wird mittels vektorieller Netzwerkanalyse im Innenraum gemessen. Der Balun wird mittels Reflektometrie gemessen. Zusätzlich werden in diesem Kapitel einige Beispiele betreffs der Messgenauigkeit vorgestellt. Konkret geht es um den parasitären Einfluss des SMA-Steckers und der kleinen Massenebene auf die Messgenauigkeit. Am Ende dieses Kapitels werden Messungen im Zeitbereich durchgeführt, um die Dispersion der Antennen zu beobachten. Zu diesem Zweck wird ein ultrabreitbandiges Signal gemäß dem Standard IEEE 802.15.4a entworfen und realisiert. Die Realisierung erfolgt mittels eines programmierbaren Signalgenerators.

# Contents

<b>1</b>	<b>Introduction</b>	<b>1</b>
1.1	UWB system . . . . .	1
1.2	Accomplishments with UWB technology . . . . .	5
<b>2</b>	<b>UWB antenna</b>	<b>8</b>
2.1	The view principle . . . . .	8
2.2	Complementary structures and the self-complementarity principle . . . . .	11
2.3	The antenna system . . . . .	15
2.4	Design of three self-complementary antennas . . . . .	15
2.5	Design of the feeding system . . . . .	19
2.6	Design improvement through simulation . . . . .	21
2.7	Self-complementary antennas and other types of UWB antennas . . . . .	30
<b>3</b>	<b>Realization and characterization of the designed UWB antennas</b>	<b>32</b>
3.1	Measurement caveats . . . . .	32
3.2	Reflection coefficient and gain of the realized antennas . . . . .	37
3.3	UWB test signal design and realization . . . . .	44
3.4	Time domain measurements . . . . .	45
<b>4</b>	<b>Summary</b>	<b>51</b>
<b>A</b>	<b>The duality principle and the origin of the magnetic currents</b>	<b>53</b>
<b>B</b>	<b>The mean electromagnetic energy flux</b>	<b>55</b>
<b>C</b>	<b>Reciprocity of a system comprising of two antennas</b>	<b>56</b>
<b>D</b>	<b>The architecture of the implemented virtual instrumentation application</b>	<b>60</b>
	<b>References</b>	<b>64</b>
	<b>List of acronyms</b>	<b>67</b>



# 1 Introduction

The ancestor of the ultra-wideband (UWB) system was the spark gap system which was used beginning with the year 1888. The signal from the spark was short in time thus having a wide frequency bandwidth. Around 1912 the system operators were conscious that narrow band systems were needed instead of spark gap systems in order to protect the increasing number of system operators from strong interference. The advent of frequency modulation (FM) technique in 1933 offered a technical possibility to control the widening of the signal and thus the tendency to use wide band systems reappeared. During the second world war a lot of experience was gathered with RADAR systems and worth mentioning from this period is the use of frequency hopping technique. Another important step was the research of the spread-spectrum technology which was first approved in U. S. A. for commercial use in 1985 and offered transmission capabilities near the noise level. Finally the UWB technology was first approved for commercial use again in U. S. A. in 2002 and for commercial use in Europe in 2007. An important note is that the UWB systems are commercially used without the need of a license. A good documented history of UWB can be studied in detail in [4].

Antennas have evolved in parallel with the telecommunication systems, the first antennas being spherical loaded dipoles and loop wire antennas. Interesting is that the term "antenna" was first used in 1909 apparently by Marconi at the Dutch Royal Institute of Engineers. The evolution of antennas during the time line does not offer a lot of clues because they are bounded to their contemporary systems for which they were used. The experience from each accomplished antenna design during this evolution is relevant. A good organized history of UWB antennas and a detailed description of the same are given in [1]. From [6] a good practical perspective is offered for the multitude of narrow band and wide band antennas.

## 1.1 UWB system

Before starting to design a UWB system or parts of it, it is important to be aware of the emissions that are allowed for this system. By doing so also the operating frequency band of the UWB system is established. The reference in this work for UWB regulations in U. S. A. is the first report and order from the FCC, [43], and for the UWB regulations in Europe is the CEPT report 45 from the year 2013, [42], based on the European Commission decision in 2007, [41].

In figure 1.1 the spectral masks both for U. S. A. and Europe as used in this work are presented. To interpret the figures the band width of UWB signal, for which an example can be seen in figure 1.2, is used as a reference. The definition, the -10 dB bandwidth of the UWB signal is greater or equal than 500 MHz, is used in this work. The equivalent isotropically radiated power (EIRP) is defined as the product of the power feed to an antenna and the maximum value of the antenna gain, i. e. the value in the main radiation direction of the antenna [5]. The conformal UWB system must not exceed a mean EIRP of -41.3 dBm/MHz. Using these definitions the design of the antenna is dependent of the whole UWB system design.

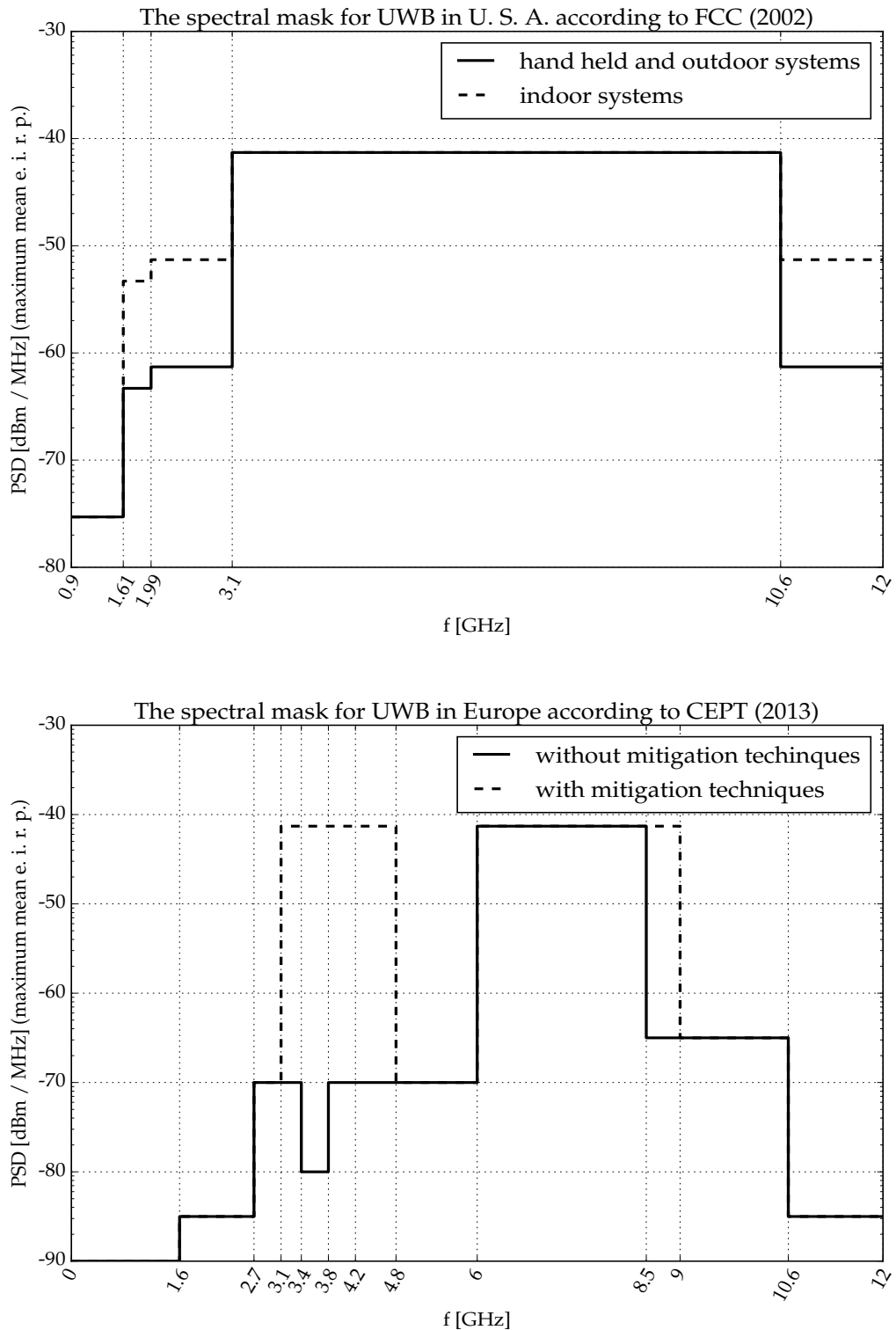


**Figure 1.1:** The spectral masks in U. S. A. and Europe.

The use of mitigation techniques in the transmitter allows for more spectral flexibility in Europe. An example of an mitigation technique is the implementation of low duty cycle as as



defined in [36].

With respect to figure 1.1 it can be concluded that the frequency band of interest in which the design of the antenna is to be performed ranges from 3.1 GHz and 10.6 GHz.

The standards that are used in this work as reference are the IEEE 802.15.4a, [35], and ETSI EN 302 065. The IEEE 802.15.4a provides specifications for physical layer (PHY) and the medium access control (MAC), which concern more the transceiver design for a UWB system, while ETSI provides specification for electromagnetic compatibility and radio matters regarding short range devices using UWB technology. The last concerns test procedures for UWB systems in the PHY.

The applications of UWB that motivated this work is the ranging application and the radar application. This allows to detect objects and movement using the small time resolution of PHY pulses of an UWB system. A common example of a pulse width is 4 ns. Recent studies focus on applying this techniques also in health care applications as documented for example in [31], in [22] and in [23]. Such applications require that the errors caused by the channel are to be kept in a tolerable range [25]. The fact that the antenna is part of the channel it contributes to the amount of errors, for example with it's gain, radiation pattern, and the dispersion caused on the UWB signal.

The interesting part of the UWB system is that ranging can be implemented as an option as recommended by 802.15.4a besides the plain data communication. As a negative consequence this can reduce the data rate of the system when this is taken into consideration for the design of a new UWB system. The ranging can be activated by using the bit in the PHY header called the ranging bit. This allows the system to use the ranging frame as illustrated in figure 1.2.

The system in figure 1.2 is given as an example of an peer-to-peer UWB system taking into consideration the minimal hardware requirements, the format of the MAC frame and the physical shape of one bit. This example is based on both mentioned standards and the majority of the scientific work based on UWB systems. A detailed explanation for this example is thus omitted here. For this work it is important to note the system environment of an UWB antenna. The UWB antenna plays a role in the accuracy of the range measurement taking also into consideration the fact that it's characteristics, like for example input impedance, radiation pattern, gain, are frequency dependent. For example, the work documented in [34] focuses on the ranging performance of an commercially available UWB system. The study is conducted mainly in the data link layer. The author analyzes also the impact of an monopole bow tie antenna on the ranging measurements but mainly from the data link perspective. The results are acknowledged and are used as part of the reference for this work.

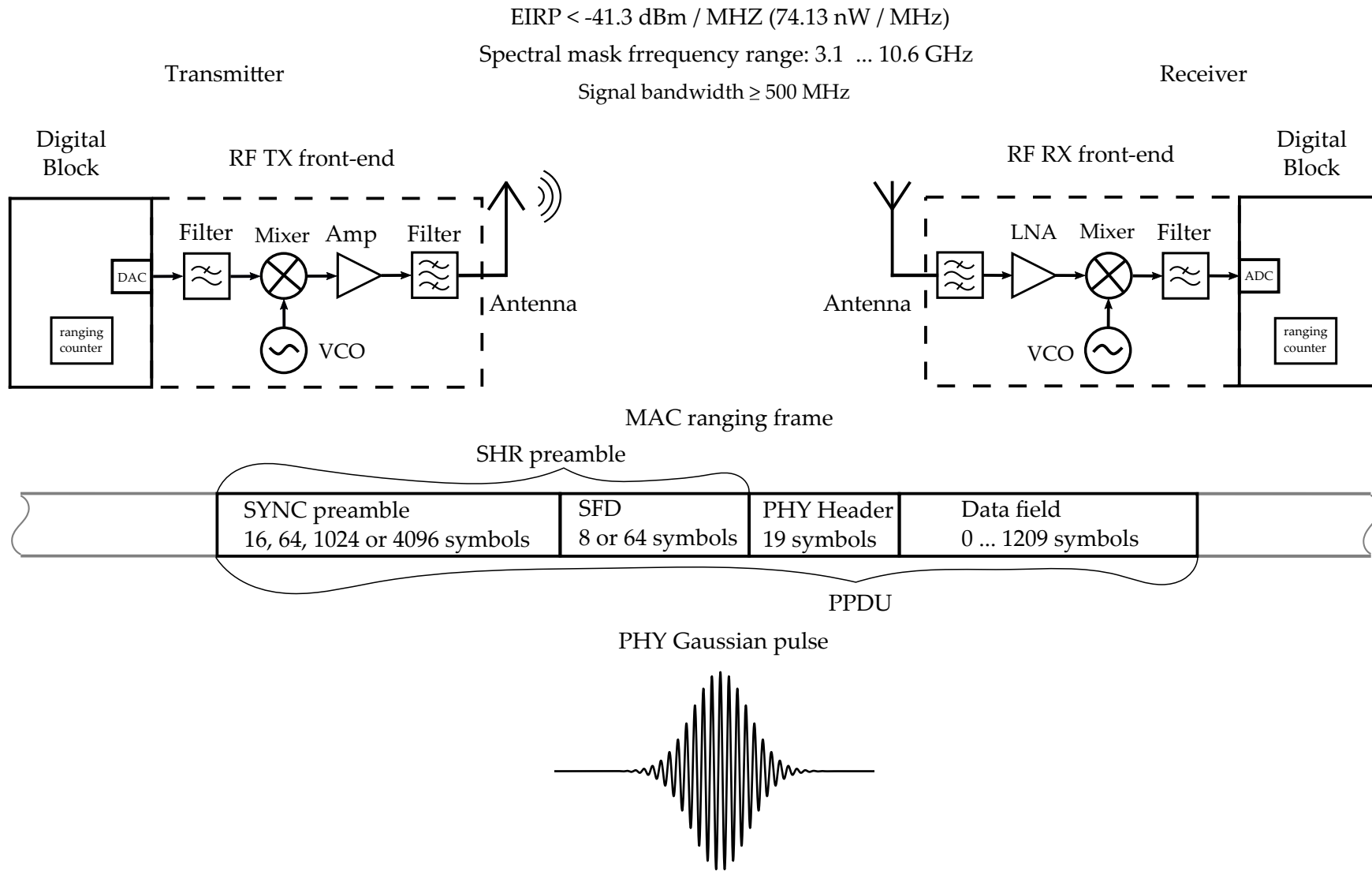


Figure 1.2: An example of an peer-to-peer UWB system.

## 1.2 Accomplishments with UWB technology

The following observations concern this present work. Selected results from scientific works and scientific papers are outlined. The focus is on antenna designs that have been used successfully for UWB systems in wireless personal area networks (WPAN) and body area networks (BAN). This literature search was conducted in order to understand the current situation of UWB antennas in practical UWB systems.

Mäkinen et al. study in their work the body effect on thin planar single-layer slot antennas, on planar self-complementary antennas and on planar wire antennas. They focus on plaster-like sensor applications at 2.4 GHz and describe the channel characteristics of an on-body to off-body channel, [3]. A comparison of several antenna types regarding their channel properties are presented. More concrete, these represent a planar magnetic dipole antenna with a geometry which is complementary to the electric dipole, a planar annular slot, a planar self-complementary dipole with a geometry based on reflection symmetry around a chosen axis, a planar self-complementary slot, a planar small inverted-F antenna, a planar large inverted-F antenna and a planar inductive meander structure. The planar self-complementary dipole had the largest form factor, namely  $7\text{ cm} \times 7\text{ cm} \times 5\text{ }\mu\text{m}$ . The measurements of the channel were conducted using a  $20\text{ cm} \times 20\text{ cm} \times 5\text{ cm}$  piece beef covered with a plastic bag with a relative permittivity of 3, which should resemble the body. The authors did not mention relative permittivity of the used beef. The antennas placed at 0.3 mm distance from the beef showed a return loss between 5 and 15 dB and a peak gain between -10 and -16 dBi. Further studies concerning distribution of energy densities and the distribution of the power loss for the planar magnetic dipole antenna, for the planar self-complementary slot antenna and for the planar small inverted-F antennas for three different spacing between the beef and the antenna, namely 0 mm, 0.3 mm and 0.6 mm, were conducted. Measurements for the radiation pattern of the mentioned three antennas in the same conditions and a comparison with the measured radiation pattern under the condition that the antenna is in the air isolated from the beef were provided. The planar magnetic dipole antenna showed satisfying results and a realization of a sensor chip using the planar magnetic dipole was presented. At the operating frequency of 2.5 GHz the sensor was characterized with a maximum gain of around -12 dBi when placed in the proximity of the body, for example 0.3 mm. Measurements of the received power of the sensor at the same proximity and the results show a sensitivity of the receiver above 10 dB. The form factor of the sensor is equal to that of the antenna, namely  $50\text{ mm} \times 31\text{ mm}$ . Details for this presented work are provided in [22].

The work of Sipal et al. regards the optimization through software of a UWB antenna which is to be used in a UWB localization system, [19]. The optimization of the antenna is based on a planar spline antenna which belongs to the family of planar monopole small-element electric antennas [1]. The point of interest here is the study of the amount of dispersion that is introduced by the antenna to the transmitted signal. The parameters that are studied are the time of arrival (TOA) and the time difference of arrival (TDOA) which are relevant for impulse-radio (IR) UWB localization systems as surveyed in [25]. The operating frequency band chosen is between 6.0 and 8.5 GHz. The test pulse with which the antenna is fed during the simulation is a root-raised-cosine pulse which complies with the IEEE 802.15.4a standard. The antenna is placed in free space. The form factor of the antenna is  $3.1\text{ cm} \times 4.0\text{ cm}$ . The

shape of the pulse is studied at different elevation angles,  $\theta$ , between 10 and 170 degrees, the gain being maximum at 0 elevation ( $\theta = 90$  degrees). The distance at which the observation was done was not mentioned by the authors. From this, the TOA and the correlation between the observed signal and the input signal was performed. The signal envelope showed no severe dispersion. Three other simulations were conducted, one with the spline antenna on a concrete block, another simulation with two spline antennas touching each other in the yz-plane, and another experiment again using two spline antennas in the yz-plane but with cylinder wall between them, all used antennas having the same form factor as the antenna in the first simulation. In the last two simulations the distance between the antennas was also varied. The motivation behind performing the last two simulations was to study the impact of the angle of arrival (AOA) on the TDOA. The AOA in these simulations is varied between 0 and 90 degrees in the azimuth plane at 0 elevation. All in all the results are satisfactory. A delay spread of roughly around 0.2 ns for the antenna in free space and around 2 ns for the antenna on the concrete block was obtained. The TDOA showed a behavior as a function of the AOA with small deviations from the linear behavior. The main message of this study is that UWB antenna designed in time domain can improve the localization accuracy of localization systems. Details for this presented work are provided in [19].

In the work of Anzai et al. in-body to on-body channels, [3], are studied experimentally, [23]. For this purpose a IR-UWB system is used which operated in the frequency band between 3.4 GHz and 4.8 GHz. The experiments are carried out on a live animal, namely a pig. During the process three UWB antennas are designed and are realized practically. One antenna is the transmit antenna. This antenna is planar with a trapezoid shape and is placed on a medical capsule endoscope, thus forming a dielectric resonator antenna, [6], [1]. The relative permittivity of the capsule is equal to 3. Its measured reflection coefficient with the antenna placed in a liquid phantom which resembles the electrical behavior of the inner living body was reported to be less than -10 dB and its gain towards the main radiation direction, likewise with the antenna placed in the liquid phantom, was reported to be -24 dBi at 4 GHz. The form factor is around 8 mm  $\times$  4 mm. The other two antennas were used as receive antennas. One is a Vivaldi antenna with linear polarization with a metallic reflector and the other one is a helical antenna with a circular polarization. These antennas are placed on the surface of the body. The form factor of the Vivaldi antenna is 11 cm  $\times$  4 cm, unfortunately with no documented distance value between substrate and the reflector. The form factor of the helical antenna is 7 cm in diameter for the ground plane and 10 cm for the length of the helical axis. The reported measured return loss is bellow -10 dB in the frequency band of operation. A goal of the experiments was to measure the path loss for different distances between the transmitter antenna, placed in the body, and the receiver antenna, placed on the body, and another goal was to study the reliability of the of the link under the same experimental conditions as the ones used in the path loss experiments provided that the tolerable bit error rate without error correction is 1 error in 200 bits. The probed distances are in the range between 40 mm and 120 mm. From the overall measurements the accepted path loss came to be 80 dB and the bit rate which the system can manage under the mentioned tolerable condition and for distances till 12 cm is 1 Mb/s. These values are given for scenarios that are likely to occur in practice and the value given for the path loss is in concordance with the results presented in [3] for the above mentioned type of channels. The effect of the antenna polarization on the path loss is also studied but only through simulation. As expected the path loss does not depend on the orientation when the helical antenna is used because the field of the helical antenna has a circular polarization. The usage of circular polarized helical antennas for on body sensors offers more flexibility in orientation than linear

polarized Vivaldi antennas. Details for this presented work are provided in [23].

Several compact on-chip UWB antennas were studied in the work of Gentner, [32]. These antennas are intended for communication between short range connectivity devices. The designed and realized antennas are variations of dipoles, of monopoles and of loop structures that present meandered geometries. Due to the fact that the on-chip antennas are integrated within the transceiver with a chip area of  $3.5 \text{ mm}^2$ , this being a system on chip realized in standard CMOS technology, the form factor of on chip antennas is small in comparison to the electrical length in the system. This classifies the on-chip antennas in the family of electrically small antennas [1]. A problem that arise with integrating antennas in chips where different layers with different relative permittivity are present, like silicon with a permittivity of 11, and silicon dioxide with a permittivity of 4, is the frequency shift to lower frequencies of the return loss, or equivalent the input impedance, of the antenna. The frequency shift is observed at for example a layer thickness of  $100 \text{ }\mu\text{m}$ . From a positive point of view this technique is also termed dielectric loading, [1], because in this case the input impedance of the antenna is controlled with concern to it's resonance value by changing the layer thickness. The same is true for the quality factor. Another problem is the dielectric loss that is a important cause for the reduction of the antenna efficiency and thus it's gain. From the presented measurements it can be concluded that the antennas present good UWB properties regarding the return loss but only at dedicated resonance frequencies that are present in the upper frequency range. The measured gain lies between  $-50 \text{ dBi}$  and  $-40 \text{ dBi}$  in a frequency range between  $4 \text{ GHz}$  and  $11 \text{ GHz}$ . The achieved communication distance with such a system on chip lies in the mm range, that being near-field communication, and the achieved data rate has a value of around  $125 \text{ Mb/s}$ . Details for this presented work are provided in [32].

For a UWB sensor system for low-power and short range applications Ruengwaree designed a new UWB antenna at the frequency band of operation in the range from  $1 \text{ GHz}$  to  $20 \text{ GHz}$ , [33]. The antenna belongs to the family of planar circular small-element electric dipole antennas [1]. The design of the antenna is mainly based on the intersection of two circles with different radius. Because of the obtained antenna shape Ruengwaree entitled it UWB rugby-ball antenna. The prototype of his antenna incorporates a reflector at  $3 \text{ cm}$  from the antenna apart, this being a quarter wavelength at  $2.5 \text{ GHz}$ . In his simulations he optimized the geometry of the antenna by focusing on the distribution of the currents in the antenna and the radiation pattern both at frequencies of  $1 \text{ GHz}$ ,  $5 \text{ GHz}$ ,  $10 \text{ GHz}$  and  $20 \text{ GHz}$ . The overall form factor of his antenna is  $17.5 \text{ cm} \times 13.7 \text{ cm} \times 5.2 \text{ cm}$ . The simulated return loss of the antenna is below  $-20 \text{ dB}$  in the frequency range between  $2 \text{ GHz}$  and  $10 \text{ GHz}$  and between  $-20 \text{ dB}$  and  $-15 \text{ dB}$  with a mildly monotonous decrease in the frequency range between  $10 \text{ GHz}$  and  $20 \text{ GHz}$  as documented. After practical realizing his prototype he performs measurements of the VSWR, of the far-field radiation and of the radiation pattern. Over the operating frequency band,  $1$  to  $20 \text{ GHz}$ , he received a VSWR lower than 2 which is equivalent with a return loss less than  $5 \text{ dB}$  and from the measurements provided it seemed to be stable over the whole operating frequency band. He compared these results with the simulation results. To reduce the weight of the antenna he introduced holes in the antenna and the reflector. This introduced resonances into the system at multiple frequencies in the frequency band of operation. Details for this presented work are provided in [33].

The five discussed works represent only a few examples of the possibilities of how to design antennas for UWB systems and how to test these systems for performance. The mentioned values for different characteristics of the antenna and UWB system serve as examples for the contemporary situation of the UWB technology.

## 2 UWB antenna

The predecessors of the UWB antennas date from the end of the nineteenth century when Heinrich Hertz (1857–1894) first demonstrated experimentally the existence of electromagnetic waves. For his experiments he used among others a spherical loaded dipole in conjunction with a parabolic cylindrical reflector. [1]. Today, at the beginning of the twenty-first century, the design of a UWB antenna is performed mainly in the frequency band of operation determined by regulatory institutions, like FCC. The frequency band that attracts the most attention lies between 3.1 GHz and 10.6 GHz. The goal of the UWB antenna designer is to design the antenna such that the characteristics of the antenna fulfill specified requirements in the frequency band of operation. For example, the return loss should exceed a certain value, the antenna gain should not be below a minimum value in the main direction of radiation and should be constant. Such design goals are determined by the UWB system and the application of such systems at hand. Another thing to mention is that the modern UWB antennas tend to have a small form factor in comparison to their predecessors and they are built on an insulating substrate. This encourages the modern UWB designer to focus on the design of planar antennas.

### 2.1 The view principle

To summarize the work presented in text books concerning the theory of antenna, regardless of the fact that the antenna may be narrow or wide band, four views of the antenna are presented in Fig. 2.1. The views presented here are an adaptation to views presented in the work of Hans Schantz, [1]. The view principle intends to guide the antenna designer into visualizing the possibilities for an antenna design. This work is to be seen as another example for the usage of the view principle in antenna design. The view principle is not used only for antennas. In the software domain the view principle helps the designer to organize the designed system components. For example the Cadence<sup>®</sup> EDA tools use the view principle to organize the content of their libraries. Each library has one or more cell views. Each cell view has among others schematic and a layout views.

The first antenna view presented may be called system view, see Fig. 2.1a). From this view the antenna is seen as a part of a wireless communication system. The antenna is characterized by parameters like bandwidth, gain, radiation pattern, directivity, polarization, aperture, dispersion. A more comprehensive description of such parameters and a description of other parameters that fit to this view can be found in [6], [1] and [5]. In the case of UWB antennas these parameters are frequency dependent. Being part of a wireless communication system the antenna is implicitly part of a communication channel. From this it may be said that the antenna contributes to the weight of the channel. For UWB antennas this observation is more conspicuous than for narrow band antennas because the wide operation bandwidth of the UWB antenna. It is to mention that in the work of Hans Schantz, [1], the antenna is seen in this view as a transducer. The antenna is a black box that converts the guided wave into free space wave and vice versa. The meaning behind this view is the same as the one mentioned above.

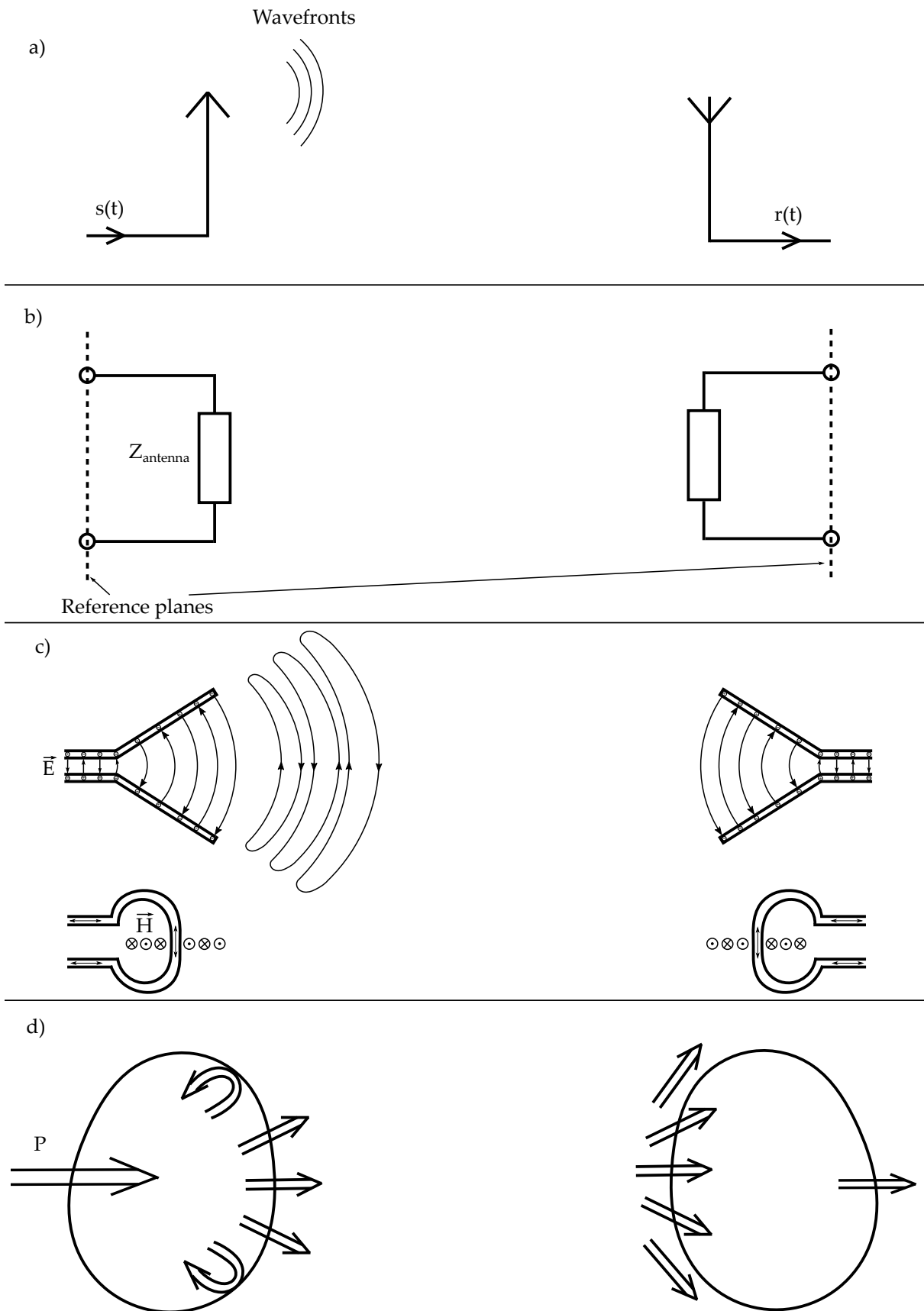


**Figure 2.1:** Four antenna views: a) system view, b) transformer view, c) radiator view and d) converter view.

The second antenna view is called transformer view [1], see see Fig. 2.1b). The designation transformer comes from the fact that the antenna is meant to transform the impedance of the wave guide, usually  $50 \Omega$ , to the impedance of the free space, approximately  $377 \Omega$ , and vice versa. Among others the main parameter that governs this view is the input impedance of the antenna, the reflection coefficient and the VSWR of the antenna [6]. For the UWB antenna these parameters depend on the frequency. The antenna structure in this view is attributed to an impedance. More concrete this impedance is composed out of a resistance that contributes to losses like ohmic and dielectric losses, a resistance that contributes to the radiation, a capacitor and an inductor that store the electromagnetic energy. These components are connected in series forming a series resonant circuit. A relevant design parameter that characterizes such a resonant circuit is the quality factor, Q-factor, which is referenced to a resonant frequency and is related in an inverse proportional manner to the bandwidth of the antenna. Details and definitions regarding Q-factor can be found in [6], [7] and [1]. The UWB antenna must present a much lower Q-factor at a resonant frequency than the narrow band antenna at the same resonant frequency, which means that the UWB antenna is lossier than the narrow band antenna. In a positive sense these losses are radiated energy.

The third antenna view is called radiator view, see Fig. 2.1c). This view was again inspired from [1]. In this view the electromagnetic field of the antenna, more exactly the field in the near field zone of the antenna and the field in the far field zone of the antenna, is of main concern. Two types of antennas are recognized in this view. One is the electrical antenna and the other is the magnetic antenna. The difference between these two antennas are obvious in their construction. The electrical antenna is an open structure and the magnetic antenna is a closed structure. Numerous examples for the electrical performance of both antenna types are found in [6] and in [1]. This work handles only electrical antennas. In this view the distribution of the sources of the radiated fields are also taken into consideration, like fore example the distribution of the currents in the metallic structure of the antenna. This is important when optimizing the antenna in terms of minimal thermal losses of the structure.

The last view presented is entitled converter view, which is likewise consistent with [1], see Fig. 2.1d). The antenna converts the amount of electromagnetic power which is feed into it, through, for example, a wave guide, to the amount of electromagnetic power that is radiated into free space. The process is reversible which means that the antenna is also capable of converting an amount of electromagnetic power from the free space into electromagnetic power that is feed for example again to a waveguide. The main parameter used in this view is the antenna efficiency. The efficiency is defined as the amount of power that is radiated by the antenna divided to the amount of power that is feed to the antenna. [1]. Another parameter that is helpful in this view is the Q-factor which was used in the transformer view. In the converter view the Q-factor is defined by the fraction of the amount of energy that is stored into the system to the amount of energy that is dissipated from the system [9]. The loss of energy is expressed in the case of antennas in ohmic losses, dielectric losses and radiated energy. No matter the antenna type, UWB or narrow band, an efficient antenna must be capable of radiating as much energy as possible while storing as less energy as possible and losing energy through heat as less as possible. This must be consistent with the conservation law. In the near field some of the radiated power couples back into the antenna structure. The border between the near field and the far field is at the distance above which radiated power cease to couple back into the antenna structure. This coupling contributes to the antenna efficiency and is to be kept through design at a minimum. In summary the converter view offers the designer the possibility to design the antenna geometry from the very beginning.



In the system view the same antenna may be used both at the transmitter and at the receiver side. In the transformer view the same antenna may be used to transform the impedances in both directions. In the radiator view the same antenna may be used for radiating the field and capturing the field. In the converter view the same antenna may be used to convert the amount of energies in both directions. Concerning the parameters of the antenna, it is expected that the antenna will behave the same in both states, due to the validity of the reciprocity property. Practically this is not always true. The designer has to take care during his measurements if the reciprocity property is valid. A theoretical aspect of the reciprocity principle is discussed in appendix C.

These views are intended to have no order in the antenna design flow. This means that the designer is free to choose the view or the views in which the design of the antenna is performed. For example the designer may choose an hierarchical approach. With respect to Fig. 2.1 it means that the designer may start with the converter view and end with the system view or the other way around. It is also possible for the designer to work with the views in parallel while taking into consideration the importance of each view for the application at hand. This means that the views are weighed differently depending on the application and the available time, like for example when Time-to-Market poses a concern. For this work a parallel approach was chosen.

## 2.2 Complementary structures and the self-complementarity principle

The self-complementarity principle helps the antenna designer to optimize the antenna in the frequency band of operation with respect to the return loss. The principle promises that the return loss is kept constant in the frequency band of operation. The theory of self-complementary antennas covers on the other hand the whole spectrum providing a general approach to the principle. In order to use the principle of self-complementarity in practice, an understanding of the theory of self-complementary antennas is required. The following observations are based on the works presented in [2], [18] and [8].

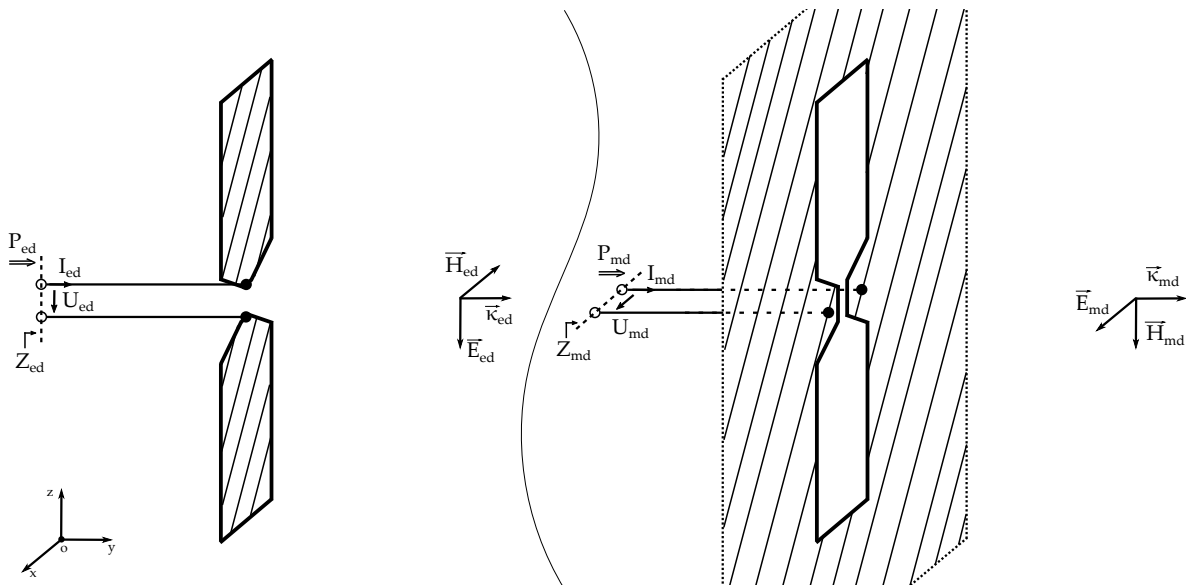


Figure 2.2: Complementary structures.

Figure 2.2 depicts the scenario of interest. One structure, entitled electrical dipole, is supplied at its port with the power  $P_{ed}$ . The other structure, entitled magnetic dipole, is supplied at its port with the power  $P_{md}$ . The supply powers  $P_{ed}$  and  $P_{md}$  are chosen unequal because this offers a more general approach for the problem. The surfaces marked with lines represent conductive sheets. These are assumed to be ideal conductors.

The duality principle of the electromagnetic field claims that every electromagnetic field problem can be transformed in a dual electromagnetic field problem. Implicitly also the solution of the original problem is transformed into the solution of the dual problem. In the presented situation the duality principle is applied in order to obtain a distribution profile of the electrical voltage<sup>1</sup> on the magnetic dipole equal with the distribution profile of the electrical current on the electric dipole. This requires that the outer boundaries of the conductive sheet of the magnetic dipole spread to infinity. What remains are the inner boundaries of the conductive sheet which are required to be equal with the outer boundaries of the conductive sheet of the electric dipole. Further argumentation on the duality principle is provided in the appendix A of this work.

The electromagnetic field of both structures in Fig. 2.2 is observed in the far field zone. It is assumed that the whole power feed to the structures is radiated and no coupling is present. Further the magnetic field strength of the electric dipole is assumed to be proportional to the numerical value of the electrical current,  $I_{ed}$ , and the electrical field strength of the magnetic dipole in the half space<sup>2</sup> is assumed to be proportional to the numerical value of the electrical voltage,  $U_{md}$ . Because the electrical voltage distributes equally both on the upper side and on the lower side of the conducting sheet of the magnetic dipole the total electric field strength of the magnetic dipole is twice the electric field strength in the half space. Using the relation  $\vec{k} \times \vec{E} = Z_0 \vec{H}$ , [7], with  $\vec{k}$  being the direction of propagation of the wave and  $Z_0$  being the wave impedance in the free space, the following relations for the electromagnetic field strengths of the two structures are given<sup>3</sup>:

$$\vec{E}_{ed} = I_{ed} Z_0 \vec{e}_{ed}, \quad \vec{E}_{md} = 2 U_{md} \vec{e}_{md}, \quad (2.1)$$

$$\vec{H}_{ed} = I_{ed} \vec{h}_{ed}, \quad \vec{H}_{md} = 2 \frac{U_{md}}{Z_0} \vec{h}_{md}. \quad (2.2)$$

$\vec{e}$  and  $\vec{h}$  are the profiles of the field strengths of the two structures. These profiles depend on the space coordinates, for example on the spherical coordinates, namely the radius, the azimuth angle and the elevation angle. Using the orientations from Fig. 2.2 and the previously introduced duality principle for the current problem, the solutions for the magnetic dipole change as follows:

$$\vec{E}_{ed} = I_{ed} Z_0 \vec{e}_{ed}, \quad \vec{E}_{md} = -2 U_{md} \vec{h}_{ed}, \quad (2.3)$$

$$\vec{H}_{ed} = I_{ed} \vec{h}_{ed}, \quad \vec{H}_{md} = 2 \frac{U_{md}}{Z_0} \vec{e}_{ed}. \quad (2.4)$$

The structures are to be feed with oscillating power at a given frequency. This means that the profiles of the field strengths can be described using complex vectors<sup>4</sup> that hold the information

<sup>1</sup>The electrical voltage applied to a magnetic dipole is also termed magnetic current.

<sup>2</sup>The half space of the magnetic dipole is bounded by the xy-plane containing the feeding point.

<sup>3</sup>Adaptation from [2].

<sup>4</sup>The complex vectors are marked using underlines.

## 2.2 Complementary structures and the self-complementarity principle

of the phase of the oscillating fields. Starting from this assumption the mean power transported by the radiated field is calculated. This is given by the real part from the integrated mean of the complex Poynting vector<sup>5</sup>. The integration is performed on a closed surface around the structures in Fig. 2.2 which is represented as the boundary of an oriented volume space. The integration surface around the magnetic dipole structure is chosen equivalent with the integration surface around the electric dipole structure:

$$P_{ed,r} = \frac{1}{2} \int_{\partial V} \vec{n} \cdot \text{Re} \left\{ \vec{E}_{ed} \times \vec{H}_{ed}^* \right\} dA, \quad P_{md,r} = \frac{1}{2} \int_{\partial V} \vec{n} \cdot \text{Re} \left\{ \vec{E}_{md} \times \vec{H}_{md}^* \right\} dA. \quad (2.5)$$

Introducing the solutions for the electric field strengths and using the relations  $-\vec{a} \times \vec{b} = \vec{b} \times \vec{a}$  and  $\text{Re}\{z^*\} = \text{Re}\{z\}$ <sup>6</sup> the radiated power results in

$$P_{ed,r} = \frac{1}{2} I_{ed}^2 Z_0 \int_{\partial V} \vec{n} \cdot \text{Re} \left\{ \vec{e}_{ed} \times \vec{h}_{ed}^* \right\} dA, \quad P_{md,r} = \frac{1}{2} \frac{4U_{md}^2}{Z_0} \int_{\partial V} \vec{n} \cdot \text{Re} \left\{ \vec{e}_{ed} \times \vec{h}_{ed}^* \right\} dA. \quad (2.6)$$

By using the input impedances of the structures the real part of the mean power that is feed into the structures is given as follows:

$$P_{ed} = I_{ed}^2 Z_{ed}, \quad P_{md} = \frac{U_{md}^2}{Z_{md}}. \quad (2.7)$$

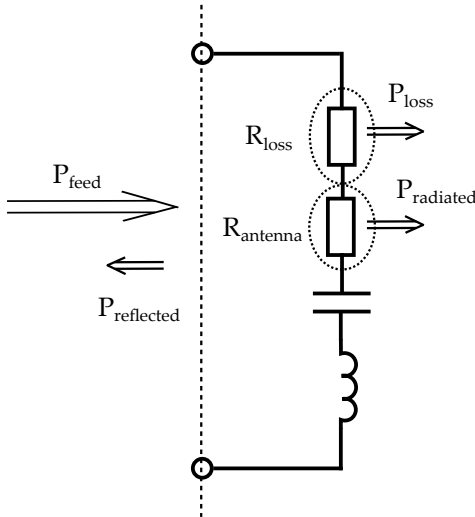


Figure 2.3: Antenna equivalent circuit.

Figure 2.3 shows an equivalent circuit of the antenna. Due to the fact that the point of interest here is not the resonance of the antenna, this equivalent circuit may be used to describe the power budget of antennas as seen in the converter view. From the power that is feed to

<sup>5</sup>The derivation of the used definition for the mean power is provided in the appendix B of this work.

<sup>6</sup> $\text{Re}\{z\}$  is the real part of a complex number.

the antenna, part of it is lost due to the ohmic and the dielectric losses, another part of it is radiated and another part is reflected. The same is observed also in [1]. An assumption made at this point is the neglecting of both the power that is transformed into heat and the reflected power. This neglecting means that their quantities are set to zero. Under this assumption in conjunction with the energy conservation law it results that the whole power that is feed to the antenna is radiated by it.

Returning to the previous calculations this results in the following statements:

$$P_{ed} = P_{ed,r}, \quad P_{md} = P_{md,r}. \quad (2.8)$$

Introducing the corresponding expressions:

$$I_{ed}^2 Z_{ed} = \frac{1}{2} I_{ed}^2 Z_0 \int_{\partial V} \vec{n} \cdot \text{Re} \left\{ \vec{e}_{ed} \times \vec{h}_{ed}^* \right\} dA, \quad \frac{U_{md}^2}{Z_{md}} = \frac{1}{2} \frac{4 U_{md}^2}{Z_0} \int_{\partial V} \vec{n} \cdot \text{Re} \left\{ \vec{e}_{ed} \times \vec{h}_{ed}^* \right\} dA. \quad (2.9)$$

From this expressions the input impedances of the structures are obtained:

$$Z_{ed} = \frac{1}{2} Z_0 \int_{\partial V} \vec{n} \cdot \text{Re} \left\{ \vec{e}_{ed} \times \vec{h}_{ed}^* \right\} dA, \quad Z_{md} = 2 \frac{Z_0}{4} \frac{1}{\int_{\partial V} \vec{n} \cdot \text{Re} \left\{ \vec{e}_{ed} \times \vec{h}_{ed}^* \right\} dA}. \quad (2.10)$$

Multiplying the two impedances results in the following equality:

$$Z_{ed} Z_{md} = \frac{Z_0^2}{4}. \quad (2.11)$$

The product of the input impedances is constant. Due to the fact that the frequency dependency was eliminated from the expressions during the derivation at the moment when the complex vector were introduced this equality is valid for each operating frequency.

The structures that fulfill this equality and are similar to those depicted in Fig. 2.2 are called complementary structures. It is also said that their geometries complete each other.

If the input impedance of the electrical dipole is known then the input impedance of the magnetic dipole can determined from the above equality. This is a consequence of the duality principle. If the solution of the original problem is known then the solution of the dual problem can be determined from that solution.

When the shape of a structure is exactly equal to the complementary shape of another structure and their input impedances are likewise equal then the structure is called a self-complementary structure. In this situation the input impedance for both of the structures is equal to approximately  $188.5 \Omega$ . From this affirmation it can be concluded that in practice only the realization of one structure is necessary. In this work this observation is used as a design principle and it shall be termed the self-complementarity principle.

The structures presented in Fig. 2.2 are more likely to represent UWB antennas than narrow band antennas, despite the fact that they were named after two theoretical narrow band antennas. The reason for this statement is that the form factor of the treated structures is closer to the form factor of a UWB antennas than that of a narrow band antenna.

Using the self-complementary principle the antenna designer can pursue a return loss which is constant over the frequencies of interest. Taking into consideration the assumptions that were made during the process in gaining this result it remains interesting if such result can be achieved in practice only for a certain bandwidth like that of the UWB system, namely equal or higher than 500 MHz. A trial of such kind is presented in this work.

## 2.3 The antenna system

The antenna system may be thought of being composed of the radiating system and the feeding system. The radiating system comprises of elements that are optimized for radiation, like for example wide metal surfaces. Such elements usually have high impedances, above 100  $\Omega$  [6]. The feeding system ensures both the impedance transformation and the canceling of the equally phased currents if such are present. Naturally this is to be achieved by the designer. Figure 2.4 shows an example of how to organize the antenna system.

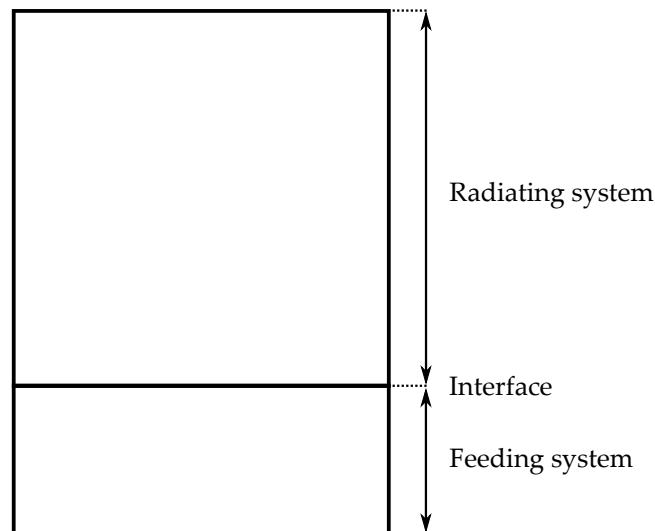


**Figure 2.4:** An example of an antenna system.

Such proposals were also made by Schantz in [1]. The above example is an adaptation of the encountered strategy proposal and reflects the strategy adopted in this work. Schantz mentioned such strategy during the discussion on controlling the antenna impedance. Changing only the shape of the structures in the antenna system, like the metal structures, causes a change for the impedance of the structure.

Organizing the antenna system in the proposed way is an old technique and has been used for numerous antenna designs. Examples of such are the Vivaldi antenna [26] from 1979, Nester's antenna [39] from 1985, both planar, and Carter's antenna [40] from 1938, which is a tapered 3D horn antenna.

## 2.4 Design of three self-complementary antennas

For this section the term antenna is used to describe the radiating system. It was chosen in this way in order to maintain consistency with the literature and scientific community.

The antenna and feeds design is restricted in this work to planar linear polarized antennas only since this is the most common design approach in the practice of UWB systems. With the emerging trend of the Internet of Things (IoT) [48] and of the wearables [3] the antenna must be small while preserving their electrical properties. The planar antennas are most suited for this task.

Based on Mushiake's studies [18] and on an article published in 2009 [24] three antenna types are observed. These observations are studied in detail in this work by preserving the rights of their owners regarding the idea but at the same time introducing new shapes and a new systematic on how to realize them while maintaining the self-complementary principle intact. In the end it is true that the antenna will present deviations from the principle in order to meet the design goal regarding the electrical performance. This may not always be the case. Nevertheless the self-complementary principle is used as a starting point.

The observed structures are classified in three categories:

- Plane-symmetrical self-complementary antennas
- Axis-symmetrical self-complementary antennas
- Rotation-symmetrical self-complementary antennas

The first examples of axis-symmetrical self-complementary antennas and rotation-symmetrical self-complementary antennas were provided by Mushiake. For plane-symmetrical self-complementary antennas a unique example was encountered in [24].

The construction of these antennas may be realized by using basic transformation operations such as translation, rotation, reflection and inversion in conjunction with well defined symmetry planes or symmetry axes. The operations are performed on a defined space which is termed in this work the primitive space. The use of this technique makes sure that the self-complementary principle is preserved for every defined shape in the primitive space. Now, not every structure constructed in this way is a feasible antenna or even at all an antenna. This still remains the responsibility of the antenna designer.

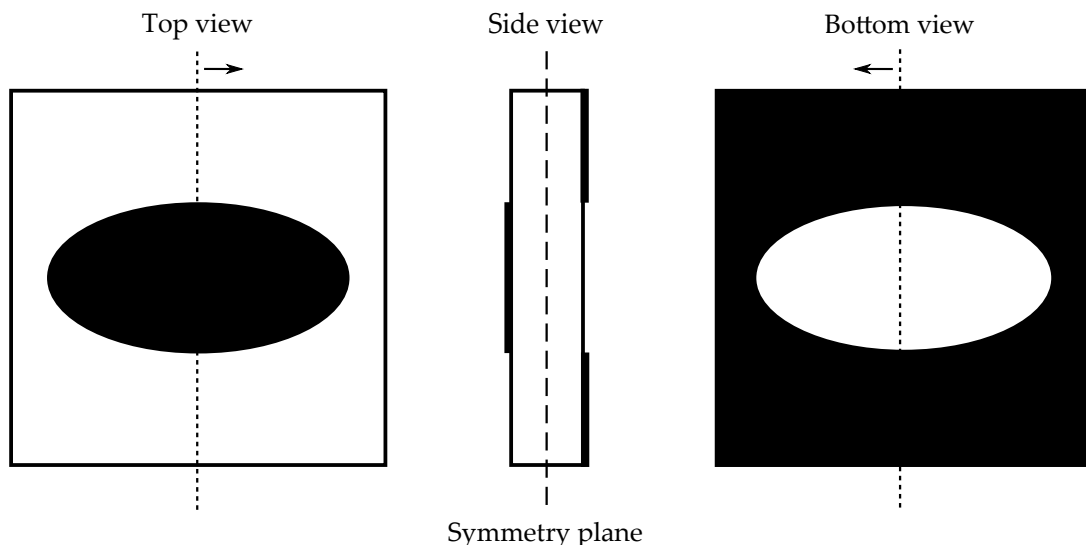


**Figure 2.5:** Plane-symmetrical self-complementary antenna.

In Fig. 2.5 an example of a plane-symmetrical self-complementary antenna is presented. The primitive space is defined by the square, which represents the edges of the substrate and it is defined, in this case, on the upper side of the substrate. A shape, in this case an ellipse, is defined in the primitive space. The primitive space together with the defined shape or shapes is translated to the bottom side of the substrate where it is inverted<sup>7</sup>. At this moment no feeding for the antenna is defined. This is taken into consideration during the design improvement later in this work.

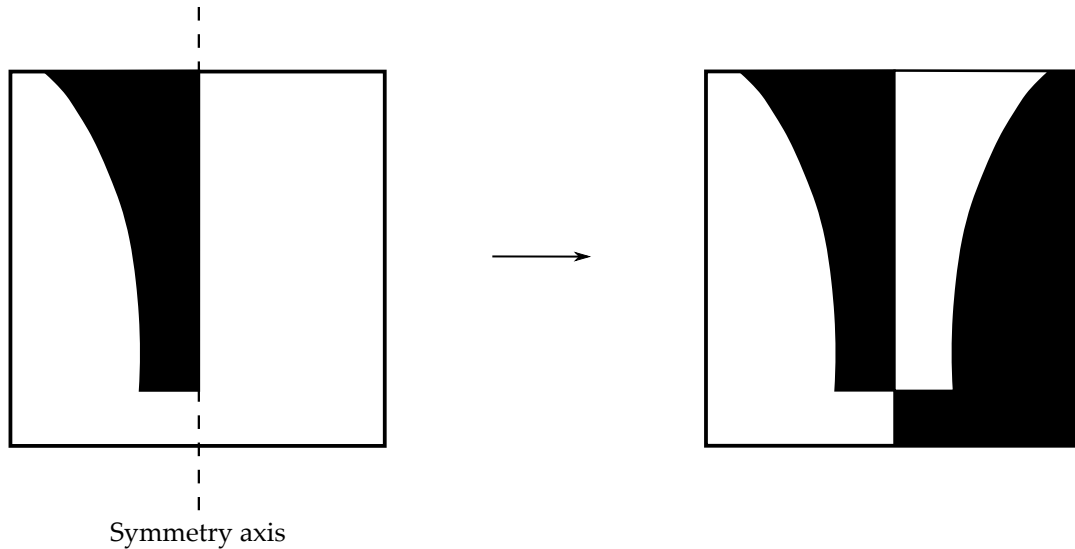


**Figure 2.6:** Axis-symmetrical self-complementary antenna.

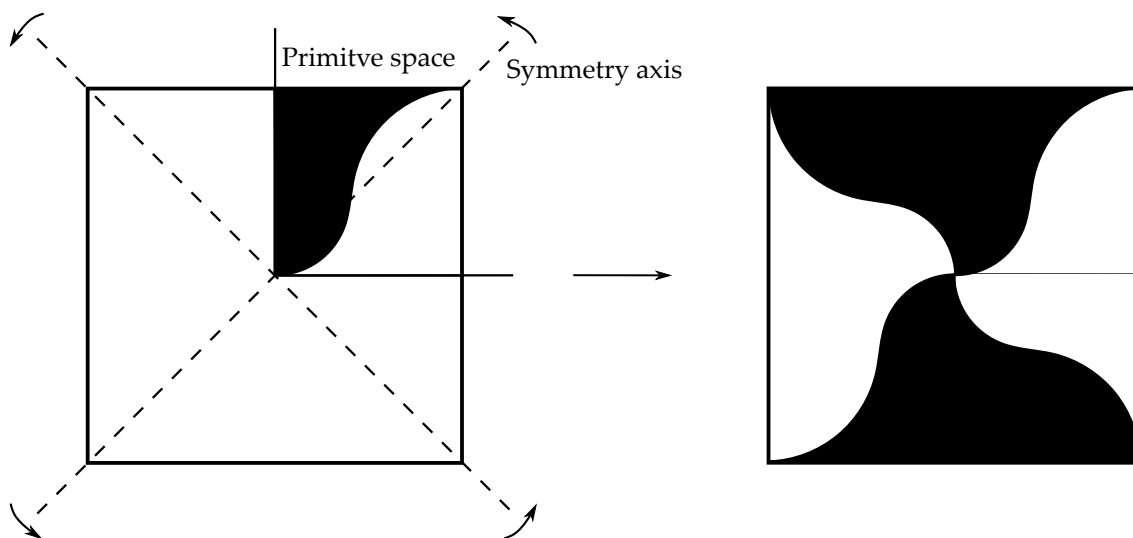


**Figure 2.7:** Rotation-symmetrical self-complementary antenna.

In Fig. 2.6 an example of a axis-symmetrical self-complementary antenna is presented. The primitive space is defined on one side with respect to a chosen symmetry axis. The primitive

<sup>7</sup>The reader should imagine the inversion operation as a toggle between black and white.

space together with the defined shapes is reflected with respect to the symmetry axis. The primitive space with the shapes included is then inverted. In this example the defined curve resembles a parabolic curve. The position of the feeding point is chosen conveniently by the designer, for example in the point where the two defined shapes intersect but it is not restricted to this particular position.

In Fig. 2.7 an example of a rotation-symmetrical self-complementary antenna is presented. The primitive space is chosen to be defined by the right upper quadrant. A symmetry axis together with a shape is defined in this quadrant. The shape need not necessarily be defined with respect with the symmetry axis. The symmetry axis serves here as a construction reference for the curved edge. The primitive space together with the defined shapes is rotated three times around it's lower left corner. The rotation angles are 90, 180 and 270 degrees. When the primitive space is in the upper left and the lower right quadrant an inversion is applied to the space. The feeding point is placed conveniently in the lower left corner of the primitive space, that being, in the end, the center of the antenna.

The plane-symmetrical self complementary antenna features a ground plane. This feature is in some situations is positive and in others is negative. The ground plane of such antenna presents a defect. This leads to a resonant antenna structure for which a pass band is defined at it's feeding point. Introducing defects into the ground plane is a known technique which is termed defected ground structures (DGS). Examples and study material for this technique is found in [1].

It is a convenient practice that antennas, or more exactly the radiating system of the antenna, has a tapered transition from a narrow to a wide structure, and thus presents wide surfaces. This tapered transition is not always helpful when the respective planar structure presents a ground plane. When this is the case the mentioned tapered structure will transition from an high impedance to a low impedance and is explained nicely by using the microstrip line model. The achieved result will be exactly the opposite of the design goal.

The method for constructing the rotation-symmetrical antenna was inspired from the construction of the log-periodic antenna [6]. The log-periodic antenna is constructed by using a transformation. The transformation consist in applying the natural logarithm on the complex plane. The points in the complex plane represent the coordinates of the antenna structure. A new antenna structure is easily defined by working in the new plane defined by the natural logarithm of the radius and the azimuth angle, which may be seen as a primitive space or a unit cell. An example of applying a similar transformation to create new structures was found in [17]. In this work the starting point for the construction is given by the choice of a unit cell geometry. An arm of the antenna is then constructed by applying the transformation on the unit cell geometry and, depending on the number of arms needed for the design, in the mentioned work 4, they are arranged centered in a point. The reason why this is feasible is because the transformation offers this possibility without the fear that the structures will overlap. Naturally the unit cell geometry must also be suitable. This falls into the responsibility of the antenna designer.

The mentioned operations used in the presented strategy to design these self-complementary antennas are not only known in this work. Such operations and even more complex ones are used also in the industry. For example the geometry modeler of the 3D structure simulators use these operations. A description of the operations of a common geometry modeler was presented in [27]. Another example, where such operations are used, is in the extended "gerber"



file format. This is a well renowned standard for printed circuit boards image data transfer in the electronics industry, more generally, a standard for a stage in the electronics manufacturing process [38].

## 2.5 Design of the feeding system

Due to the fact that for self-complementary antennas an impedance higher than  $50 \Omega$  is expected, a feeding system that transforms the impedance of the antenna to  $50 \Omega$  is often required.  $50 \Omega$  is the value of the impedance for most of the cable connectors, one of the most popular examples being the SMA connector or its variants. A very interesting argument regarding the value of  $50 \Omega$  is found in [10], which summarized, states that the choice of the value  $50 \Omega$  for the wave impedance of the transmission lines is a compromise between minimum attenuation and maximum power capability.

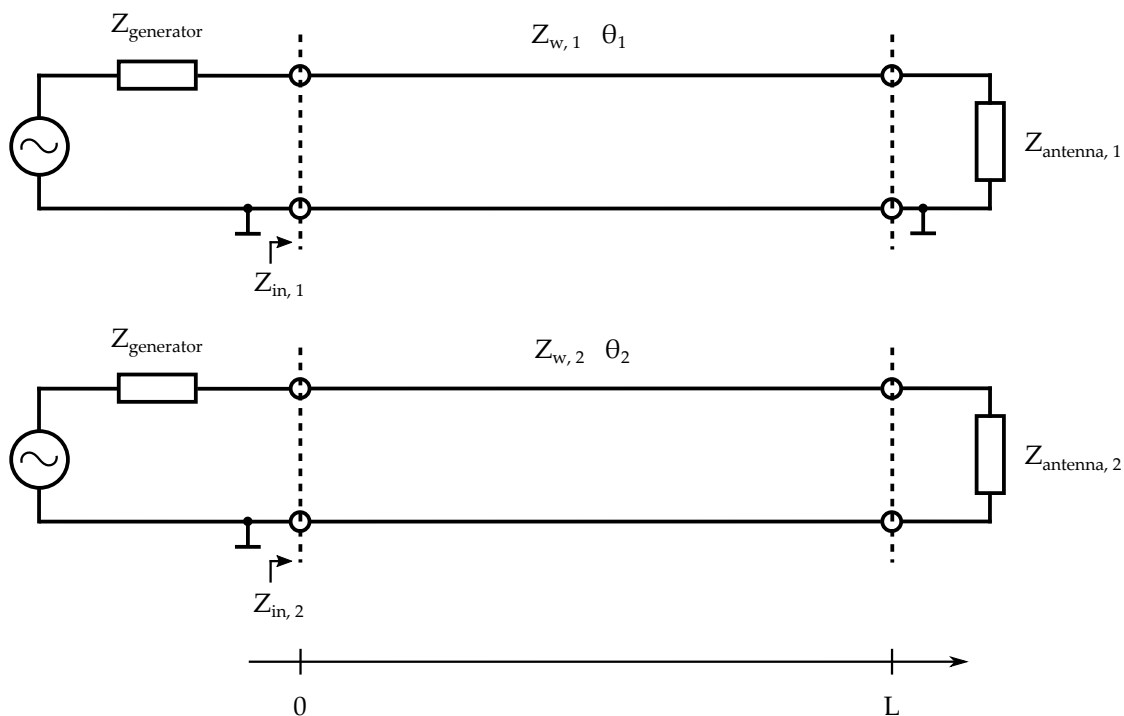


**Figure 2.8:** Models for the feeding system. The first model represents a transition from a unbalanced system to a unbalanced system. The second model represents a transition from a unbalanced system to a balanced system.

Fig. 2.8 presents the model that was used for the design of the feeding system in this work. With one model the transition from a asymmetrical system to a asymmetrical system is modeled, like for example to a monopole antenna. With the other one a transition from a asymmetrical system to a symmetrical system is modeled, like for example a dipole antenna. For the second transition a balun is in practice needed. The first model is a common transmission line and it is depicted to represent a reference for the design. The second model was inspired by the numerous examples presented in [11], [12] and [1].  $Z_w$  is the wave impedance of the line and  $\theta$  is the electrical length of the line. Notice that the parameters of the transmission line are not the same. This is due to different layouts of the two systems.

It is true that, if understood properly, the transmission line may serve as a unun or as a balun. Duncan and Minerva showed in their work how elegantly a balun can be realized by tapering the outer conductor of a coaxial cable [20] and Climer studied among others the possibility to use the suspended microstrip taper as balun. The design of a unun from a transmission line is illustrated in the following and it is true also for the design of a balun but incomplete. For the complete design of a balun also the suppression of the common mode currents must be taken into consideration.

The following equation is used during this work to aid in the design of the needed transmission line transformers. It states that the input impedance is dependent on the wave impedance of the transmission line, the electrical length of the transmission line and on the load impedance, which in this particular case is the impedance of the antenna structure. The impedance of the antenna can be measured and is known. The input impedance is the design goal, namely 50  $\Omega$ . The design parameters remain the wave impedance and the electrical length, which in turn depend on geometry parameters, like width and length of the line, the used material, the velocity of the wave and the frequency,

$$Z_{in} = Z_{in}(Z_w, \theta, Z_{antenna}). \quad (2.12)$$

A common example for such an expression, token from the textbook [10], is given in Eq. 2.13 and is the expression for the input impedance of the theoretical transmission line which is terminated in this case with an antenna.

$$Z_{in} = \frac{Z_{antenna} + j Z_w \tan(\theta)}{Z_w + j Z_{antenna} \tan(\theta)} Z_w. \quad (2.13)$$

By designing the electrical length to be 90 degrees at a specified frequency, the above expression becomes

$$Z_{in} = \frac{Z_w^2}{Z_{antenna}}. \quad (2.14)$$

A expression for the wave impedance, the design parameter, can be obtained, which is the geometrical mean between the input impedance and the antenna impedance. This is the expression for the well known quarter wavelength transformer [10]:

$$Z_w = \sqrt{Z_{in} Z_{antenna}}. \quad (2.15)$$

In this special case the wave impedance of the quarter wavelength transformer is assumed constant over the length of the structure. A more flexible approach is to use tapered lines. In this case the transmission line structure is designed in a way that the wave impedance increases or decreases with the length of the line. This is a systematic approach to achieve a variety of impedance transformation ratios at a certain frequency. Commonly taper line transformers are the linear taper, the exponential taper and the Klopfenstein taper. An example of a Klopfenstein taper for a 100  $\Omega$  to 376  $\Omega$  transition is found in [1]. The reflection loss at the input of the structure is used as a figure of merit, which is derived from the wave impedance. Details on tapering of transmission lines are provided for example in [10].

Besides the impedance transformation the balun must also ensure that the common or even mode currents are suppressed. It is very difficult to characterize the amount of suppression

directly, that is by measuring the even currents. An indirect method would be to look at the radiation of the balun structure. This is done by means of simulation, by means of measurements or jointly. In this work only the simulation is taken into consideration.

## 2.6 Design improvement through simulation

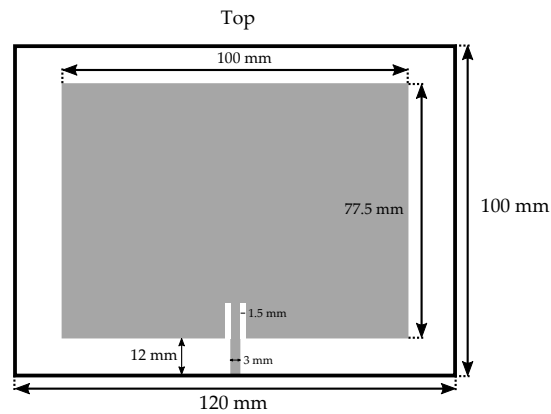
The chosen designs need to be verified. A convenient low cost option is given through the simulation. For this purpose, a commercial electromagnetic 3D structure simulator is used. The commercial simulator HFSS from ANSYS® was selected for its high frequency simulation capabilities.

In order to work efficiently with the simulator it is necessary to understand its functionality. A short, for this work relevant, brief of HFSS is given with examples.

The HFSS engine is based on the finite element method [47]. Inside the simulator a discrete mesh is constructed using a tetrahedron as a primitive cell. The information of the fields is stored in the vertexes and additionally in the midpoints of the tetrahedrons and finally the field inside each tetrahedron is interpolated from the corresponding values. This is important to be aware of when configuring the mesh size, for example when trading simulation accuracy in favor of simulation speed. HFSS has also a versatile solid geometry kernel. With it, it is easy to construct complex geometries out of primitive shapes like squares, circles, boxes and cylinders, to name a few, in conjunction with boolean and geometric operations. The geometry kernel of HFSS allows to parametrize the geometry. This enables to maintain the whole structure consistent with deformation, like for example when the length of an edge is changed. HFSS offers also an optimizer which is not discussed in this work. The tuner was used to change the parameters interactively. An example of an efficient framework of a simulator based on a similar concept is presented in [27].

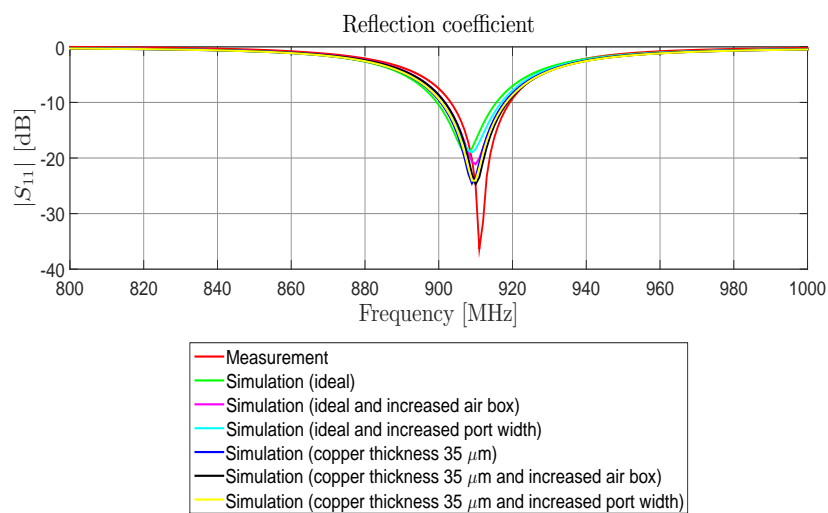
Fig. 2.9 shows a resonant patch antenna intended for 900 MHz. This antenna was realized by colleagues at the institute and is used in this work as a test structure within the simulator. The substrate of the antenna is FR-4, its height is 1.60 mm and the ground plane covers the whole surface of the substrate. To simulate a resonant structure, and compare it afterwards with measurements, is a convenient way to test the simulator because resonances are sensitive to changes and this can be observed clearly for different scenarios.

Fig. 2.10a shows a diagram of the patch antenna's reflection coefficient in which scenarios with different simulation configurations are tested. "Ideal" means that the copper foil is modeled as a perfect electric conductor (PEC). The air box represents the space in which the electromagnetic field equations are solved and, at its boundaries, a second order boundary condition is used, which emulates free space. It is recommended by the HFSS developers that the boundary should be spaced half a wavelength apart from the structure. This distance was increased in the simulation to half a wavelength and documented in the figure. The port is the part of the structure through which energy is fed and is defined by using a rectangular window. This window is to be imagined as the interface between an infinite rectangular waveguide and the structure. The dimensions of this window have an influence on the number of modes that are allowed to propagate in the rectangular waveguide and thus reach the structure [5]. The port length was increased from the length of the feed line to the length of the substrate.



**Figure 2.9:** The body model patch intended for 900 MHz used as test structure for the simulation.

(a)



(b)

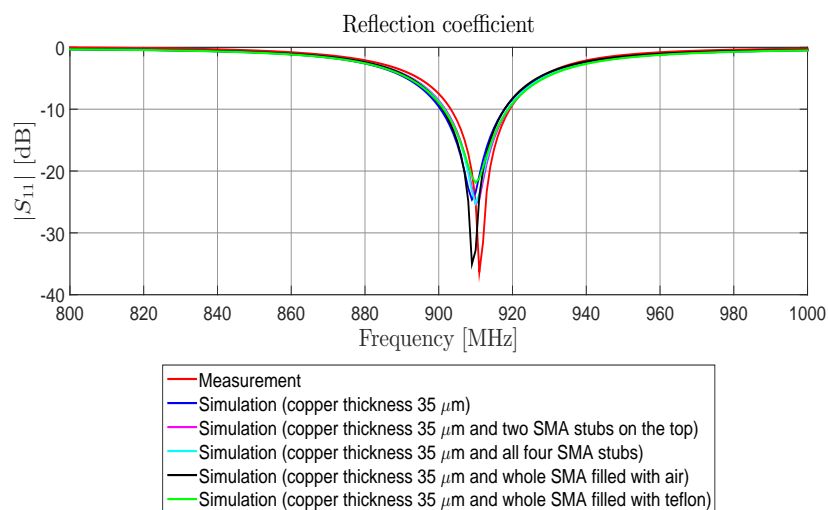


**Figure 2.10:** Reflection coefficient of the body model patch for different simulator configurations, see Fig. a, and for different scenarios, see Fig. b.

The results in of Fig. 2.10b show how the measurements are approached when realistic scenarios are taken into consideration. It is also observed that the simulation accuracy deteriorates as Teflon is added to the SMA. This is because this scenario requires a more detailed modeling approach due the complexity of the SMA connector. The presence of the stubs are not expected to influence the performance of the structures, because they resonate at around 11 GHz as will be seen later in this work.

For the wide band structures another simulation approach is needed than for narrow band structures. While in HFSS it is recommended by the developers to simulate narrow band structures using a fast frequency sweep, for wide band structures it is recommended to use an interpolating frequency sweep. In the fast frequency sweep the simulator solves the problem accurately at a frequency determined by the user, for example the resonant frequency, and then extrapolates the solution for other frequencies. The interpolating frequency sweep is an iterative method. In this mode, the problem is solved at frequencies chosen by the simulator in the frequency domain specified by the user. In this simulation mode the user specifies the maximum error tolerance, in this work 0.09, or the maximum number of iteration steps, in this work 20. The simulator performs in both modes an automatic mesh refinement. The user is allowed to toggle this mesh refinement. This was left on during the simulation in this work.

In Fig. 2.11 the result of the two sweep modes for the Vivaldi antenna from Fig. 2.12 are presented. The Vivaldi antenna was provided by the institute and it is used in this work as a test structure for the simulator. It is seen that the difference between the modes is not so obvious. Regardless of this behavior the interpolating frequency sweep is chosen for simulation of wide band structures as the developers of the simulator recommend.

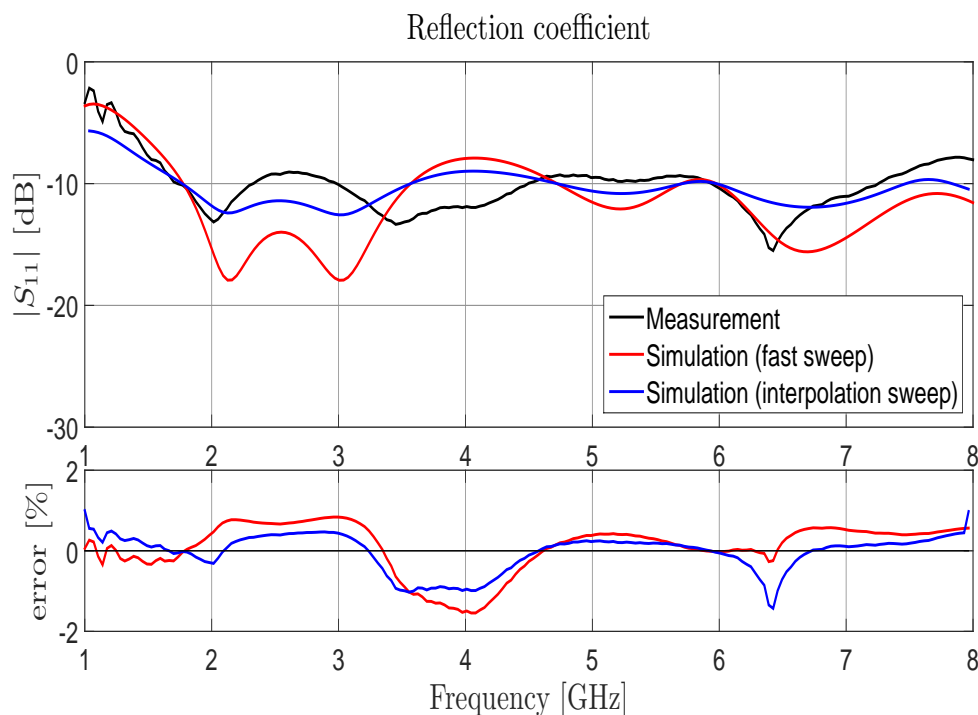


**Figure 2.11:** Reflection coefficient of the Vivaldi antenna for different simulator configurations. The fast sweep is at 4 GHz. The error is defined as  $\| |S_{11, \text{measurement}}| - |S_{11, \text{simulation}}| \|$ .

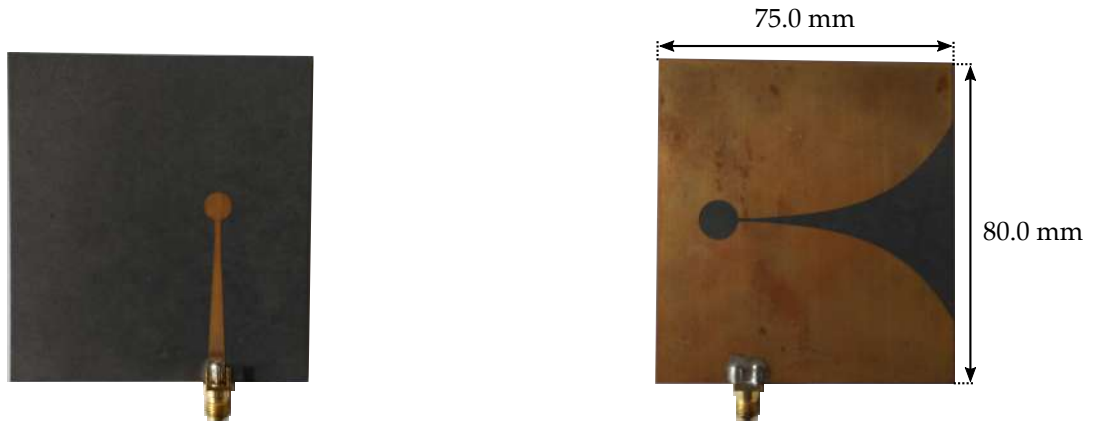


**Figure 2.12:** The Vivaldi antenna used as a test structure during the simulation.

In the following, the improved design of the three presented self-complementary antennas is presented without presenting any simulation results. These are left for chapter 4 because it is more interesting to see the simulation results in comparison with the measurement results. Only the highlights and caveats are presented in this section.

The antennas were simulated in the interpolating frequency sweep mode with adaptive mesh refinement. The solution type chosen was the modal solution for which the fields in the problem space are calculated by the simulator. From them the quantities of interest are derived, for example the S-parameters. For the conductors, PEC sheets are used and for the substrate, RO4003C is used from ROGERS corporation with a relative permittivity of 3.55.

In Fig. 2.13 the improved design for the plane-symmetrical self-complementary antenna is presented and in Tab. 2.1 its summarized geometric parameters are given. The self-complementarity of the antenna had to be damaged in order to achieve a matched structure. The ellipse cut in the ground plane is larger than the ellipse patch. The ellipse patch had to be cut from the co-vertex. The width of the line feed corresponds to that of a  $59 \Omega$  ideal microstrip line with infinite ground plane. During the simulation it was observed that the most sensitive spot is the bottom line feed that rises into the ellipse cut in the bottom plane. The main radiation direction is expected to be perpendicular to the patch and the antenna is expected to radiate in the antenna plane on both sides. The maximum gain is expected to be at 7 GHz and it is estimated to 3 dBi.

In Fig. 2.14 the improved design for the axis-symmetrical self-complementary antenna is presented and in Tab. 2.2 its summarized geometric parameters are given. The self-complementarity of the radiating system for this antenna is kept intact. The radiating system resembles that of the Vivaldi antenna. This is because the radiating system of both antenna types is composed of a tapered slot line. In this case the taper is a parabolic taper in contrast to the Vivaldi antenna for which the taper is exponential. From Fig. 2.14 the taper is rather unusual because it occurs only on one side. It is interesting to note that such a structure was derived by using the self-complementarity principle. The width of the feeding line corresponds to that of a  $70 \Omega$  ideal microstrip line with infinite ground plane. The feeding system represents a balun with a transition from a microstrip line to a slot line. Similar feeding systems are found for Nester's microstrip notch antenna [39] or for a more recent antenna design in [29]. The main radiation direction follows the parabolic curve. It is expected that the antenna radiates side-

ways. An offset from the left boundary, parameter  $o^t$ , is introduced in order to accommodate a near straight main radiation direction while maintaining the matching of the structure. The maximum gain is expected to be at 7 GHz and it is estimated to 1.65 dBi.

In Fig. 2.15 the improved design for the rotation-symmetrical self-complementary antenna is presented and in Tab. 2.3 its summarized geometric parameters are given. The self-complementarity of the radiating system is mainly kept intact except at the feeding system where accommodations were necessary. It should not be a surprise for the reader that the design differs from Fig. 2.7. This was chosen deliberately to demonstrate the presented method for designing the rotation-symmetrical self-complementary antenna with a different example. The main radiation direction is expected to be perpendicular to the radiating system and the antenna is expected to radiate in the aperture of the radiating system on both sides. The maximum gain is expected to be at 4 GHz and it is estimated to 1.6 dBi. The polarization is expected to be circular and not linear. Fig. 2.16 shows the simulation results for the input impedance of the structure together with the 188.5  $\Omega$  line.

In Fig. 2.17 a design of the feeding system is presented and in Tab. 2.4 its summarized geometric parameters are given. The design was inspired by the results presented in [21]. This is a microstrip balun and it was designed for the rotation-symmetrical self-complementary antenna. A similar structure, used in this work as a reference, is encountered in [30] but designed for a bow tie antenna in the UHF. The top tapered line was designed using a linear taper. The bottom tapered line was designed by using an arc. The edge points of the arc were fixed at the interfaces between the middle region and the input region and between the middle region and the output region respectively. The middle point of the arc was used as a design parameter. This taper was chosen to approximate the exponential taper, see Fig. 2.18. At the output side a cut is introduced in order to mechanically accommodate the connection with the designed antenna from Fig. 2.15. The input was designed for a 50  $\Omega$  wave impedance and the output was designed for the simulated impedance from Fig. 2.16.

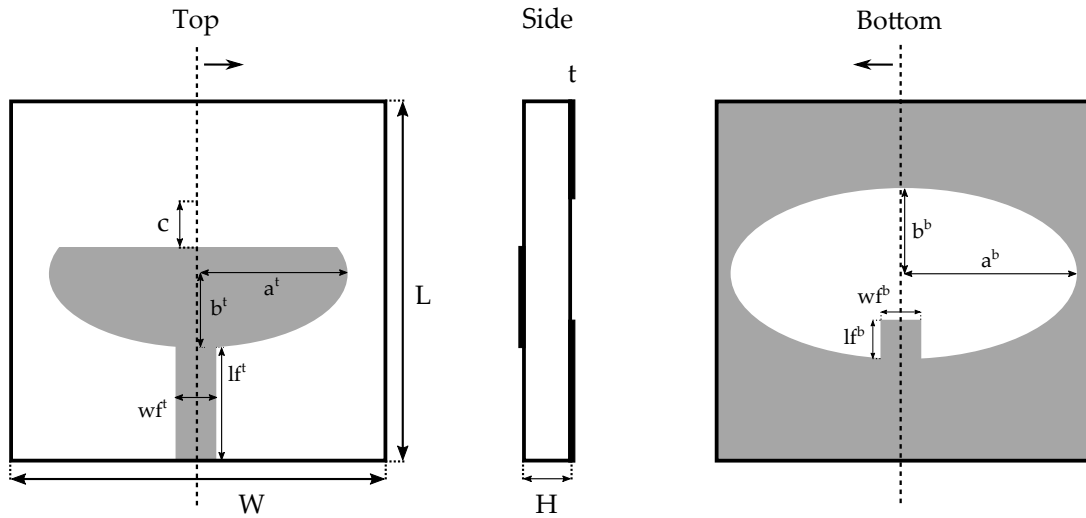


Figure 2.13: Improved design of the plane-symmetrical self-complementary antenna.

Table 2.1: Geometry parameter table for the designed plane-symmetrical self-complementary antenna:

Parameter	Value [mm]	Description
H	0.813	substrate height
W	22.0	substrate width
L	21.0	substrate length
t	0.035	copper thickness
$wf^t$	1.4	top feed line width
$lf^t$	7.0	top feed line length
$a^t$	6.6	top ellipse semi-major axis
$b^t$	3.3	top ellipse semi-minor axis
c	1.0	the amount of the truncation referenced to the ellipse co-vertex.
$wf^b$	1.7	bottom feed line width
$lf^b$	1.89	bottom feed line length
$a^b$	1.2	semi-major axis of the bottom ellipse
$b^b$	0.6	semi-minor axis of the bottom ellipse



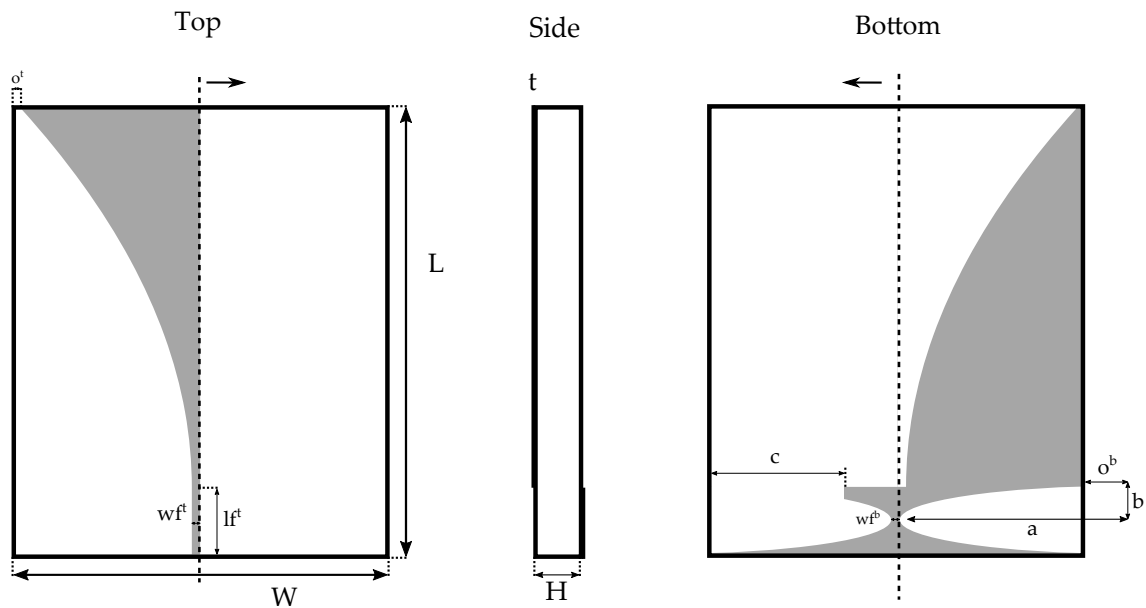


Figure 2.14: Improved design of the axis-symmetrical self-complementary antenna.

Table 2.2: Geometry parameter table for the designed axis-symmetrical self-complementary antenna:

Parameter	Value [mm]	Description
H	0.813	substrate height
W	50.0	substrate width
L	60.0	substrate length
t	0.035	copper thickness
$wf^t$	1.0	top feed line width
$lf^t$	10.0	top feed line length
$o^t$	1.51	offset from the vertical edge
$wf^b$	1.0	minimum bottom feed line width
a	30.0	semi-major axis of the the bottom ellipses
b	4.5	semi-minor axis of the bottom ellipses
$o^b$	5.0	distance between vertical edge and ellipse center point
c	17.0	the amount of truncation referenced to the vertical length

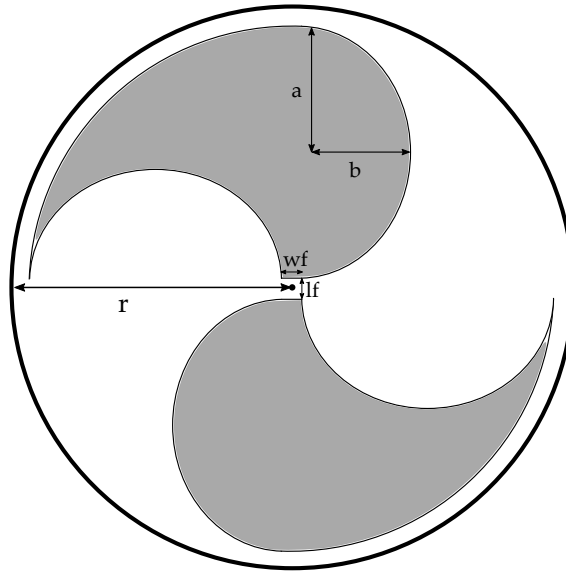


Figure 2.15: Improved design of the rotation-symmetrical self-complementary antenna.

Table 2.3: Geometry parameter table for the rotation-symmetrical self-complementary antenna:

Parameter	Value [mm]	Description
H	0.2	substrate height (not depicted)
r	40.0	substrate radius
t	0.035	copper thickness (not depicted)
wf	0.813	feed region width
lf	0.813	feed region length
a	20.0	semi-major axis of the ellipse
b	18.0	semi-minor axis of the ellipse

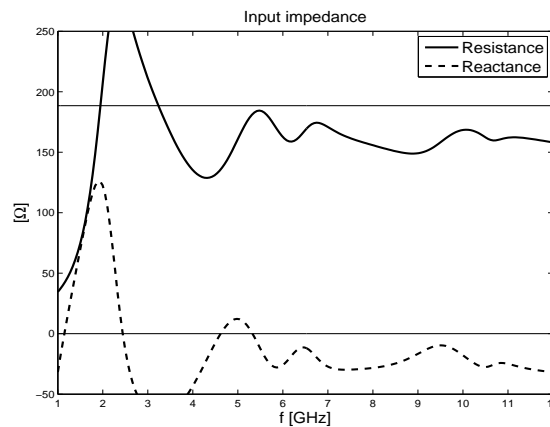


Figure 2.16: The simulation results for the input impedance of the designed rotation-symmetrical self complementary antenna. The 0 and 188.5  $\Omega$  line is drawn.

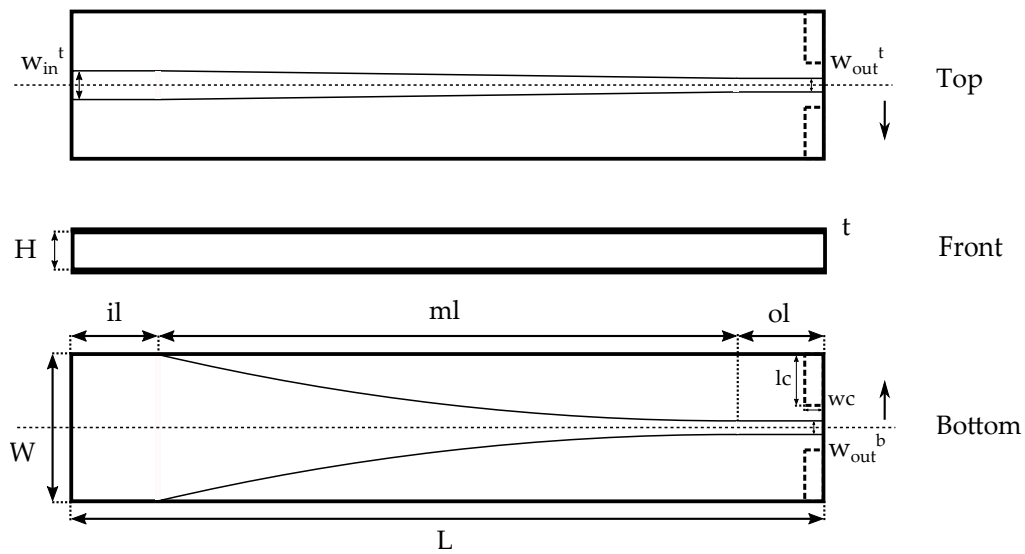


Figure 2.17: Designed microstrip balun.

Table 2.4: Geometry parameter table for the microstrip balun:

Parameter	Value [mm]	Description
H	0.813	substrate height
W	10.0	substrate width
L	55.0	substrate length
t	0.035	copper thickness
$W_{in}^t$	1.77	top input line width
$W_{out}^t$	0.45	top output line width
$W_{out}^b$	0.45	bottom output line width
il	4.0	input region length
ml	46.0	middle region length
ol	5.0	output region length
wc	1.0	the width of the truncated area
lc	8.5	the length of the truncated area

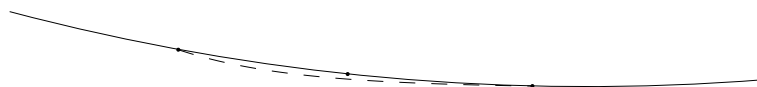
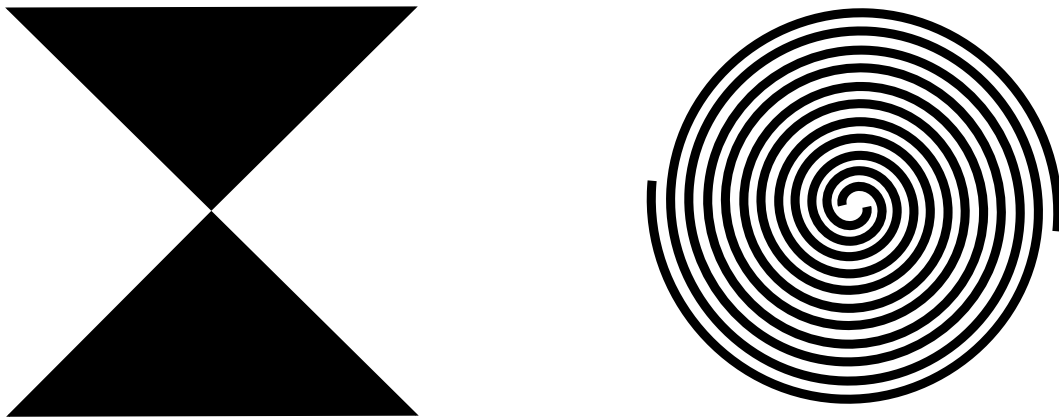


Figure 2.18: Approximation of the exponential taper, dashed line, with an arc taper, continuous line, drawn on a scale of 1.385 to 1

## 2.7 Self-complementary antennas and other types of UWB antennas

Some of the known UWB antennas can be parametrized to conform with the self-complementary principle. The bow-tie antenna has a self-complementary structure when the apex angle is chosen to have 90 degrees. The spiral antenna may also be made self-complementary if the width of the spirals is made equal with the width of the gap between the spirals. The bow-tie antenna is a linearly polarized antenna and the spiral antenna is a circularly polarized antenna. An example of such a design is presented in Fig. 2.19. Measurements for a bow-tie antenna with an apex angle of 90 degrees are found in [1].



**Figure 2.19:** Examples of self-complementary UWB antennas that can be made. On the left side is the bow tie antenna with the apex angle of 90 degrees and on the right side is the spiral antenna with the spiral width equal with the gap width.

Rumsey introduced a class of antennas entitled frequency independent antennas in 1966, see [28]. For frequency independent planar antenna structures the radius of the radiating structure is made exponentially dependent on the azimuth angle and can be configured using a parameter in the exponential argument. In the general case this parameter is used to weight the argument of the exponential function. More exactly, the expression  $r_0 e^{a\phi}$  dictates the frequency independent behavior. Fig. 2.20 shows an example of a rotation-symmetrical self-complementary antennas designed using the frequency independent principle. On the left side of the figure the frequency independent principle is used with different parameter values to define the primitive space of the rotation-symmetrical self-complementary antenna. On the right side of the figure the method for constructing the rotation-symmetrical self-complementary antenna is applied for one parameter value. The choice of the design parameter value depends on the desired physical dimensions of the antenna. For example it is seen in Fig. 2.20 that the width of the feeding region is varied for different values of the parameter in question, for example it increases with increasing parameter values.

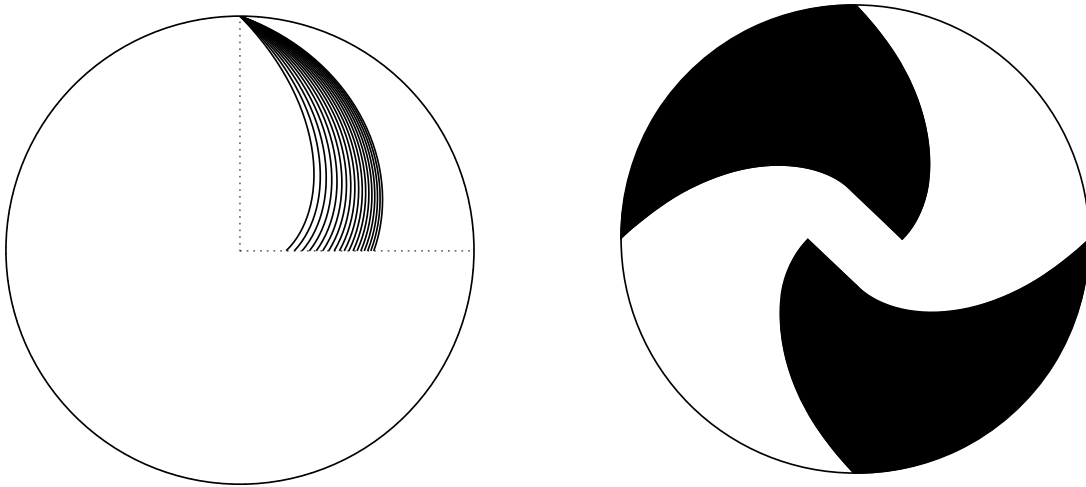


**Figure 2.20:** Example of a rotation-symmetrical self-complementary antenna designed using the frequency independent principle.

## 3 Realization and characterization of the designed UWB antennas

In order to test the designed antenna structures, several prototypes were manufactured. Fig. 3.1 shows the end state of the manufactured and tested antenna prototypes. The microstrip balun was soldered with the rotation-symmetrical self-complementary antenna. As a reminder this balun provides a  $50 \Omega$  impedance at its input and transforms the unbalanced feed of the measurement cable to balanced feed of the antenna and vice versa. The balun of the axis-symmetrical self-complementary antenna is likewise to be seen in Fig. 3.1. The substrate used is the RO4003C [45] from ROGERS corporation. The masks for the antennas were manufactured using ultraviolet photolithography and the unwanted copper was removed by means of etching. The quantities that are measured for the antenna prototypes are the reflection coefficient and the gain in the main radiation direction.

### 3.1 Measurement caveats

For the microstrip balun a Time Domain Reflectometry (TDR) measurement was performed, see Fig. 3.2 and 3.3. For the TDR measurement a signal generator and an oscilloscope are needed. The used instrument is the SDA100G, which is an oscilloscope with an integrated signal generator. The source generates a test pulse, in this case a step signal. The test signal is fed to the structure under test through a port and the reflected signal from the structure is measured at the same port. The rise time of test signal is the main parameter. In this case it was set to 20 ps, which means that structures with a maximum bandwidth of 17.5 GHz can be characterized with this test pulse. The microstrip balun fulfills the bandwidth prerequisite and the calculated space resolution for this structure is 1.6 mm. In Fig. 3.3a the influence of the top SMA connector stubs on the performance was observed. The dotted line in the measurement results represents the effect of touching the tip of one of the SMA conductor with a metal probe. From this effect the resonance frequency of the stubs can be determined. The time difference in which this effect occurs is 0.09 ns. The inversion of this difference is the resonance frequency of the stubs, which has a value of 11 GHz. The impedance value of the balun increases relative smoothly from the unbalanced input towards the balanced output with the curve being steeper near the output than the input as can be seen in Fig. 3.3b. The achieved value at the output is  $142 \Omega$ , which is  $8 \Omega$  lower than the designed value of  $150 \Omega$ . The achieved value is impressive because this shows how accurate the design is.

Fig. 3.4 presents a measurement of the microstrip balun with and without SMA connector stubs using the network analyzer ZVA24 from Rohde & Schwarz. As expected, the resonance frequency of the stub is at 11 GHz. The measurement reveals that the structure radiates between 10.5 and 11.5 GHz. It is observed that the structure radiates also at 9.3 GHz.

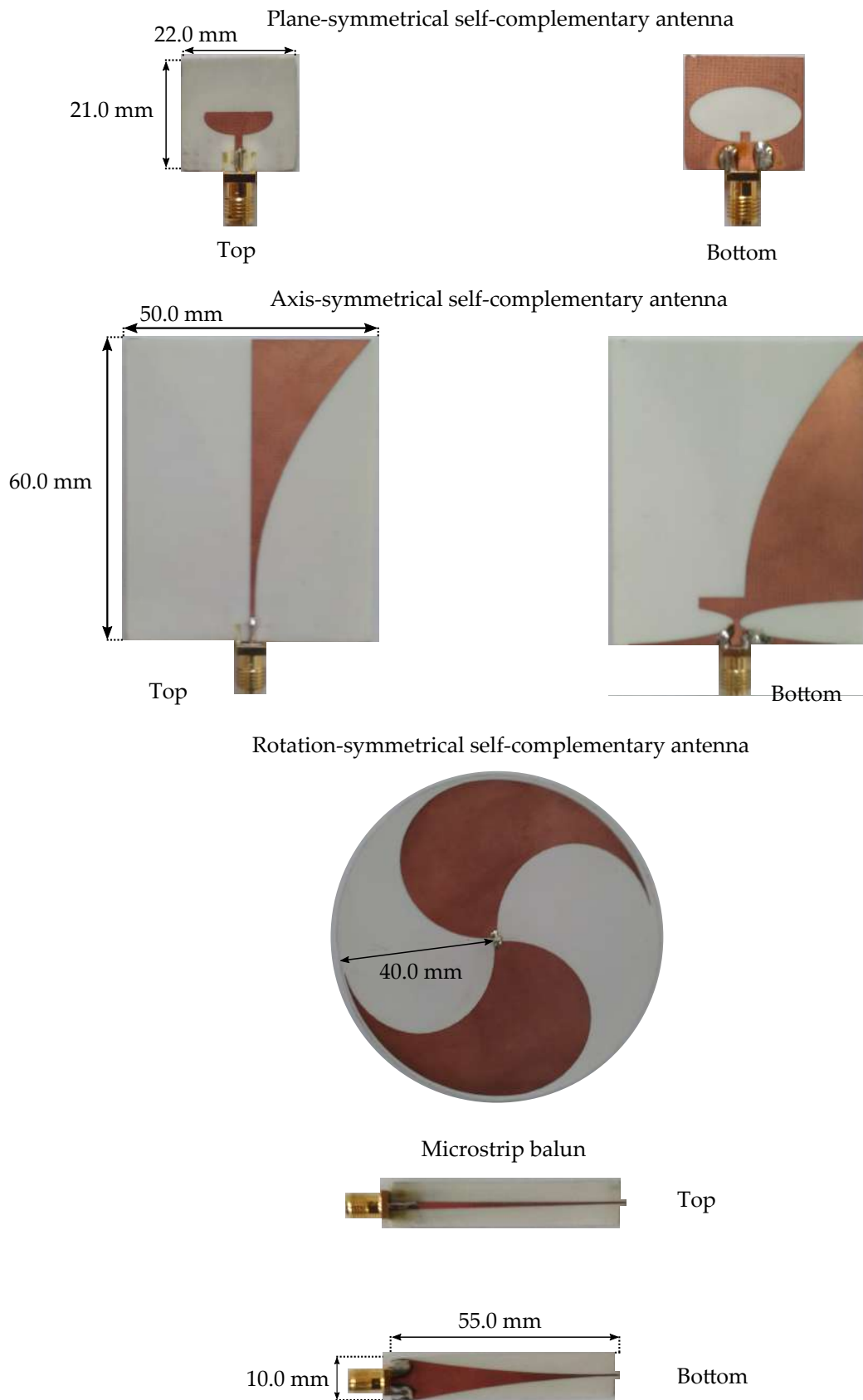
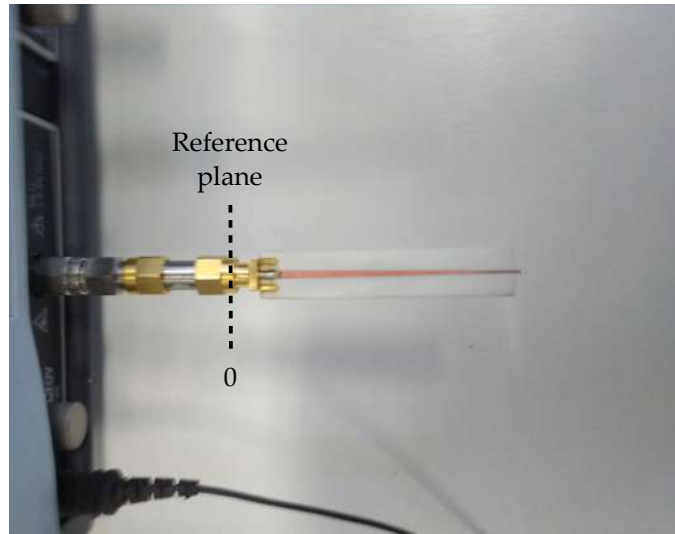
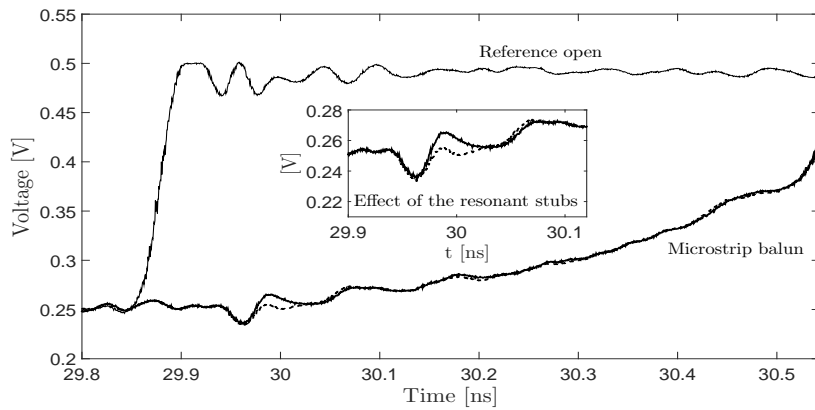


Figure 3.1: The manufactured and tested antenna prototypes.



**Figure 3.2:** TDR measurement setup for the microstrip balun with marked reference plane. The instrument used is the SDA100G sampling oscilloscope from LeCroy. The rise time was set to 20 ps.

(a)



(b)

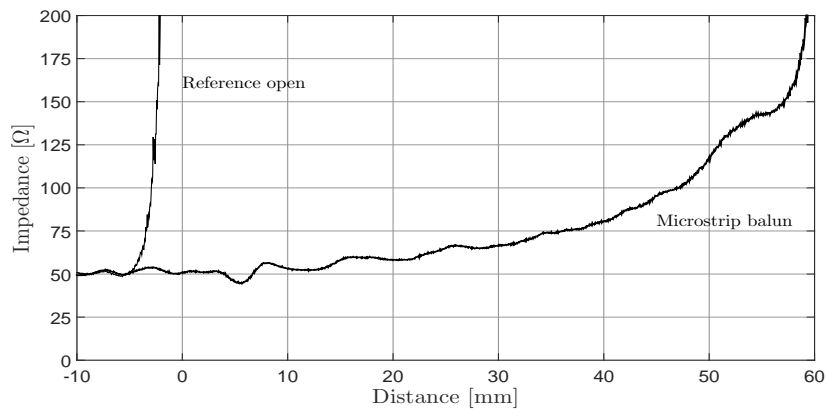


**Figure 3.3:** The TDR measurement results. Fig. (a) presents the measured voltage as a function of time. Fig. (b) presents the impedance of the microstrip balun as a function the distance.



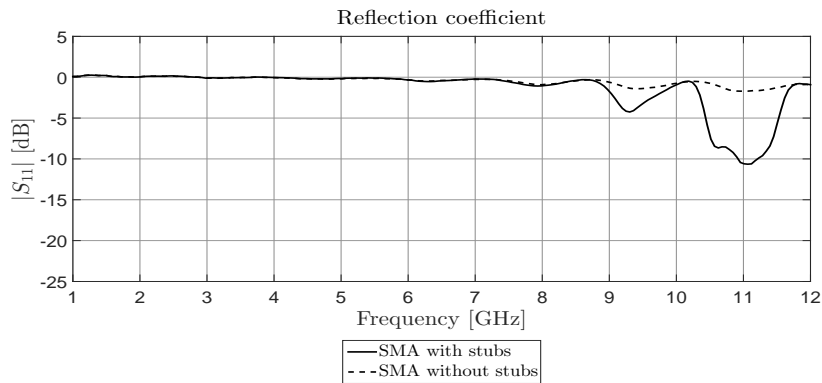


**Figure 3.4:** Network analyzer measurement results for the microstrip balun with and without the resonant stubs.

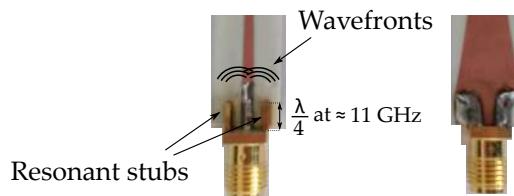


**Figure 3.5:** The top resonant stubs of the SMA from the microstrip balun. The radiation of the stubs is highlighted.

Removing the top stubs of the SMA connector, as done in this work, will cause the resonance to diminish. The microstrip balun will behave as an open, a behavior that is expected. Another solution would have been to connect the stubs with the ground plane by using vias.

It is important to understand that the resonance stubs causes the structure to radiate at frequencies unexpected from the design of the structure without an SMA connector. The SMA connector is needed to perform the measurements of the structure. The problem is that the connector introduces errors to the measurements. The comparison was conducted and documented in this work for the frequency domain between 1.0 and 12.0 GHz in order to signalize the awareness of such errors. This is naturally not restricted to the microstrip balun structure. Fig. 3.7 shows an example where the presence of the SMA stubs falsify the measurement at high frequencies as can be observed from the magenta colored line. To solve this problem the SMA connector stubs at the top were removed.

Symmetric antennas have the problem that they cause common currents in the feeding structure. When the feeding structure is the measurement cable, then the currents are termed cable currents. These currents will cause the feeding structure to radiate, which will falsify the measurement. A common example of a symmetric antenna is the dipole antenna. A planar patch antenna behaves like a dipole if its ground plane is small in comparison with the patch. The designed plane-symmetrical self-complementary antenna poses the problem of small ground plane. Although the measurement of the reflection coefficient presents acceptable values and

### 3 Realization and characterization of the designed UWB antennas

the simulation results are in good agreement with the measurement as presented in Fig. 3.7, a closer inspection will confirm that the presence of the measurement cable falsifies the measurement, which is not at all desired.

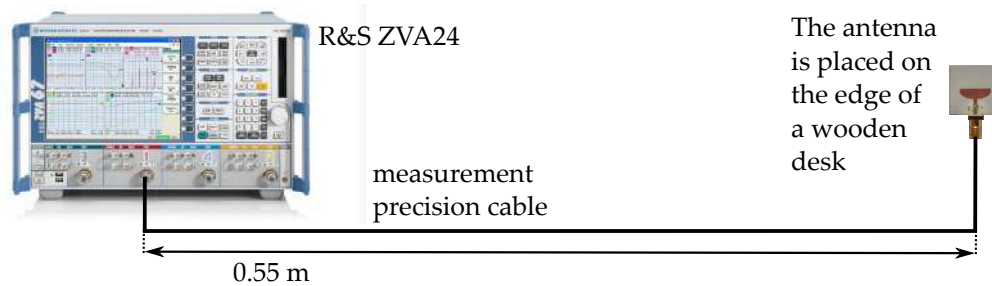


**Figure 3.6:** The measurement setup for the plane-symmetrical self-complementary antenna.

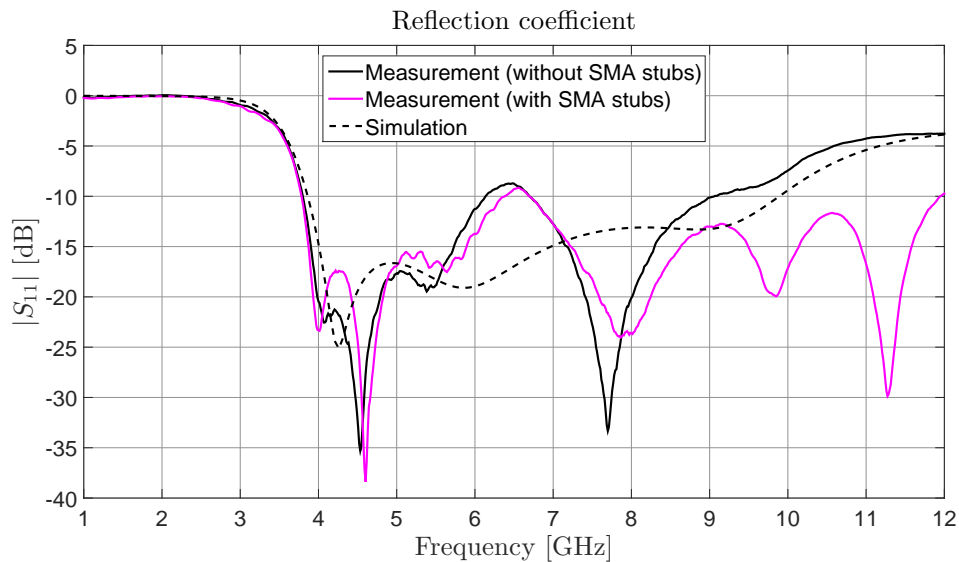


**Figure 3.7:** The reflection coefficient of the plane-symmetrical self-complementary antenna.



**Figure 3.8:** Adding a ground plane to the plane-symmetrical self-complementary antenna will diminish the cable currents. This technique is a tradeoff between accurate measurements and small form factor. The ground plane is realized out of a 0.2 mm RO4003C substrate. The stubs on the top were not removed.

To overcome this problem a solution would be to realize a monopole by adding a large ground plane as presented in Fig. 3.8. The size of the ground plane should be chosen as high as possible because these ensures high non-symmetry of the structure. Constraints for the size are

imposed by the performance of the structure regarding reflection. The diameter of the ground plane is chosen with the help of the simulator two times the diagonal of its radiating structure. Another solution would have been to add a wide band balun in the feeding system of the antenna or to shield the cables. A wide band shield is very difficult or not even at all possible to realize.

### 3.2 Reflection coefficient and gain of the realized antennas

Before conducting the measurements on the antenna prototypes, a calibration of the measurement instruments and of the measurement setup is needed. The setup used for the calibration is presented in Fig. 3.9. The antennas under test are placed on a rotating tower with the top made out of rohacell material [46], a material which behaves like air from an electrical point of view. The calibration procedure is taken from the ETSI standard [37] with the slight modification that the measurements are conducted in an indoor environment, which is rich in scatterers, and not in an anechoic chamber, where reflections are suppressed, and that the antennas are in the far field only at frequencies below 5 GHz. The intention with this measurement is to characterize the antennas in an environment in which they are likely to be used. In this case a measurement example with the antennas placed in the near field is provided. The disadvantage with this procedure is that the measurement accuracy is poor because in the near field also the non radiating field are captured by the antenna through coupling. In this calibration procedure the unknown path loss is determined and its influence is removed from the measurement. The influence of the cable losses are removed by calibrating the network analyzer. The path loss is determined by using the gain of the horn antennas, which, taken from the data sheet, has a nominal value of 11.5 dBi with a deviation of  $\pm 1.5$  dB. The reflection coefficient of the horn antennas together with the calculated free space path loss is presented in Fig. 3.10.

From Fig. 3.10a the reflection coefficients of the horn antennas is roughly below -10 dB above 6 GHz, which means less than ten percent return loss. For a UWB system with 500 MHz bandwidth it means that less than  $3.715 \mu\text{W}$  out of  $37.15 \mu\text{W}$  is reflected at the antenna terminals. The manufacturers of the horn antenna specify an operating frequency range between 6 and 12 GHz.

The path loss is estimated from Fig. 3.10b to be 50 dB. Naturally, the fact that the gain of the horn antennas was assumed constant over frequency has introduced errors to the determination of the path loss. Also the channel itself introduces errors in the determined path loss, for example through reflections from scattering objects. A comparison with the free space path shows a 4 dB difference, which is more than half in power terms. Never the less this measurement result is used as reference for the path loss. Below 6 GHz the path loss increases because the reflection coefficient of the horn antenna increases to 0 dB.

The network analyzer used for the measurements is the ZVA24 from Rohde & Schwarz capable of performing measurements up to 24 GHz. The power level of the network analyzer was set to 0 dBm and 804 measurement points were acquired to achieve a good measurement resolution. Before conducting the measurement, the network analyzer was calibrated. The calibration removed the influence of the cables. The measurement is performed remotely using the virtual instrumentation application designed during this work. Its architecture is presented in the appendix D.

The reflection coefficient of the antennas under test were measured on the tower using coaxial cables of standard RG400 with SMA connectors and on a wooden desk with the antenna placed on the edge of the desk using a measurement precision cable designed to be used with the network analyzer. The second measurement was chosen in order to compare the measurement for the antenna placed on a tower with a more accurate one. Adding the round ground plane to the plane-symmetrical self-complementary antenna resulted in the reflection coefficient presented in Fig. 3.12a. The antenna radiates mainly at 8.0 GHz in a bandwidth of 2 GHz. It is hard to predict the resonance frequency of this monopole because the pole is a quadrangle. In Fig. 3.14a the reflection coefficient of the axis-symmetrical self-complementary antenna is presented. The antenna can be used between 5.0 and 9.0 GHz, that is this antenna has a 4 GHz bandwidth. This antenna is capable of covering the channels 5 to 12 from the IEEE 802.15.4a standard. The reflection coefficient for the rotation-symmetrical self-complementary antenna is presented in Fig. 3.16. This antenna can be used between 2.5 and 10.5 GHz and it covers all the channels from the IEEE 802.15.4a standard. It is to observe that at high frequencies a noise like behavior is present in the measurement results. This is because of the length of the used cables, in this case 2.0 m, and the power level used by the source, in this case 0 dBm. The cables show high cable losses at high frequencies. The power level is too low for these frequencies, which causes a mitigation of the measurement accuracy. A solution would be to increase the power level, for example to 3.0 dBm, which is twice of the initial power level.

The simulation results are likewise presented in Fig. 3.12a, 3.14a and 3.16, besides the measurement results. The simulations were performed without the SMA connector. There is a good agreement between the measurement results and the simulation results. It is to notice that the simulation results for the rotation-symmetrical self-complementary antenna are from the structure without the balun attached, whose simulated input impedance was presented in section 2.6 in Fig. 2.16. In all three cases the measurement results are better than the simulation results in term of magnitude value. The main difference is made by the presence of the SMA connector, which provides a better matching to 50  $\Omega$  than the simulator. The simulator emulates a rectangular waveguide with an infinite length as a connector.

In Fig. 3.12b the gain of the monopole antenna is presented. From the measurement the gain of the monopole antenna is estimated at 3 dBi up to 9 GHz. Above 9 GHz the gain goes down to -3 dBi when the DGS of the monopole is oriented toward the horn and for the case when the patch is oriented toward the horn the gain becomes very low above 10.5 GHz and rises again from 11.5 GHz. This behavior is due to the presence of the SMA connector stubs that were not removed. These stubs are part of the circular ground plane. This is proof that the presence of the stubs degrades the quality of the monopole antenna concerning the gain. In Fig. 3.14b the gain of the axis-symmetrical self-complementary antenna is presented. From this measurement a gain of 1 dBi is estimated when the antenna is oriented vertical. If the antenna is oriented horizontal the gain decreases to -10 dBi. This axis-symmetrical self-complementary antenna is vertical polarized. The orientation of the electric field is in the plane with the slot. When the antenna is oriented horizontally, and because the horn antenna has a vertical polarization, little power is received. In Fig. 3.14b the gain of the rotation-symmetrical self-complementary antenna is presented. From the simulation it is expected that this antenna behaves like a circular polarized antenna. The measurement in Fig. 3.14b lacks in accuracy from the same reason as for the measurements of the reflection coefficient, namely the high loss of the measurement cables. It is not possible to tell if the obtained values are plausible. The accuracy of the measurement can be improved if the power of the network analyzer is increased, for example to 3 dBm, which is twice of the initial power level.

### 3.2 Reflection coefficient and gain of the realized antennas

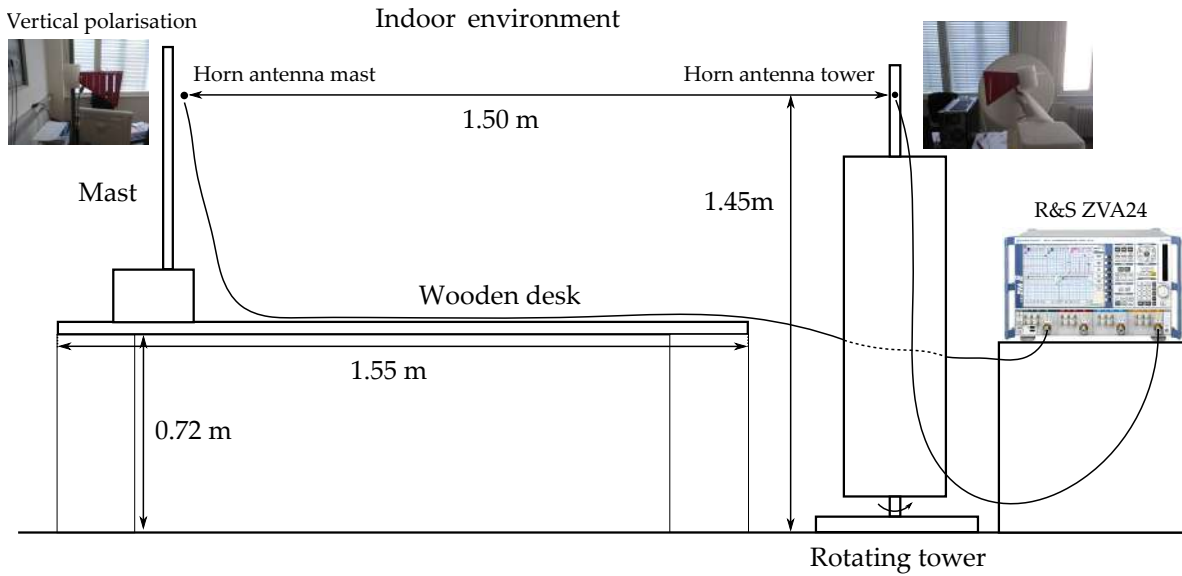


Figure 3.9: The setup used for calibration.

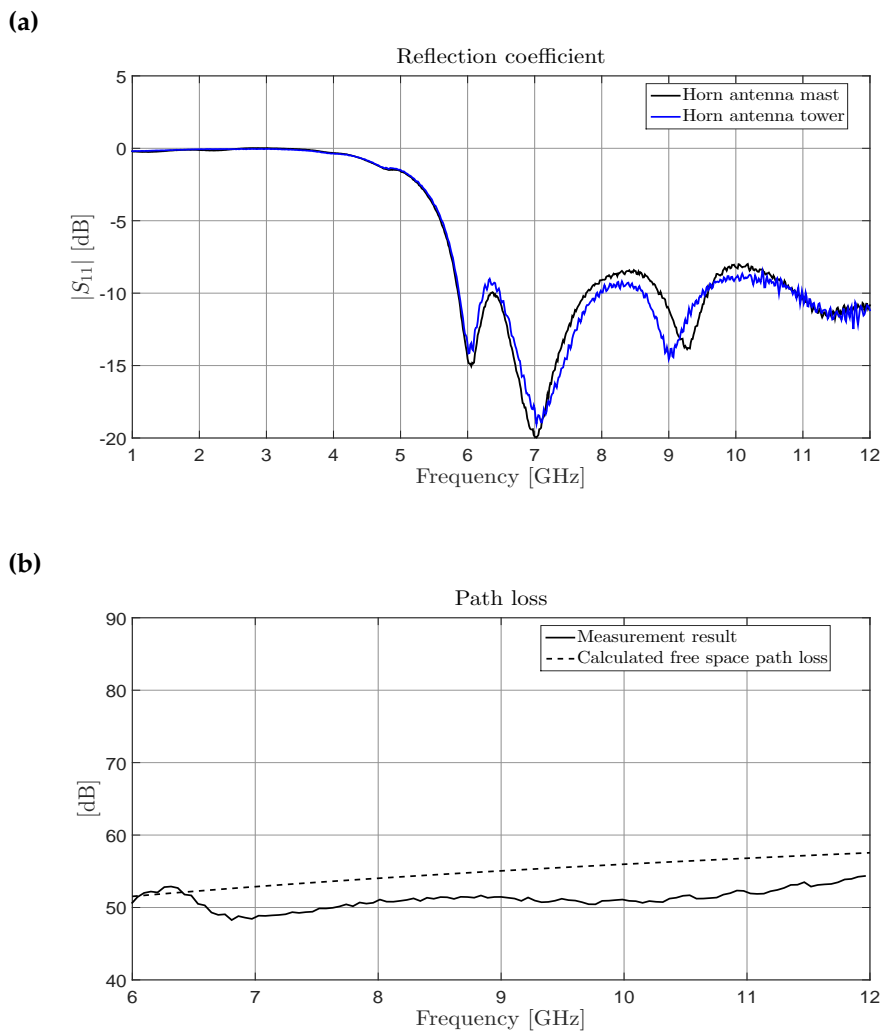
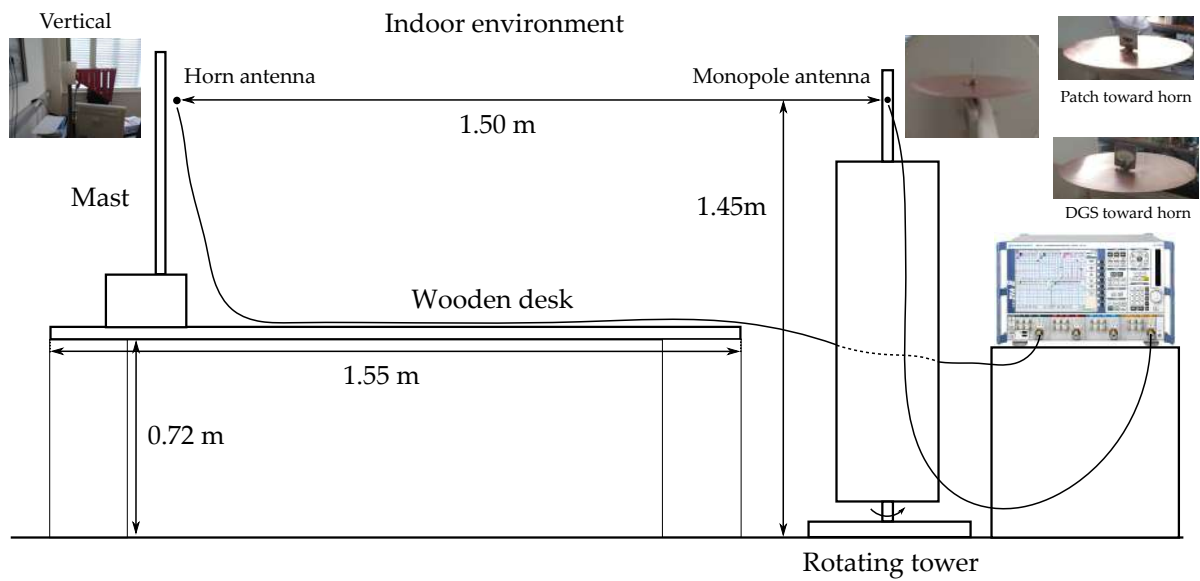


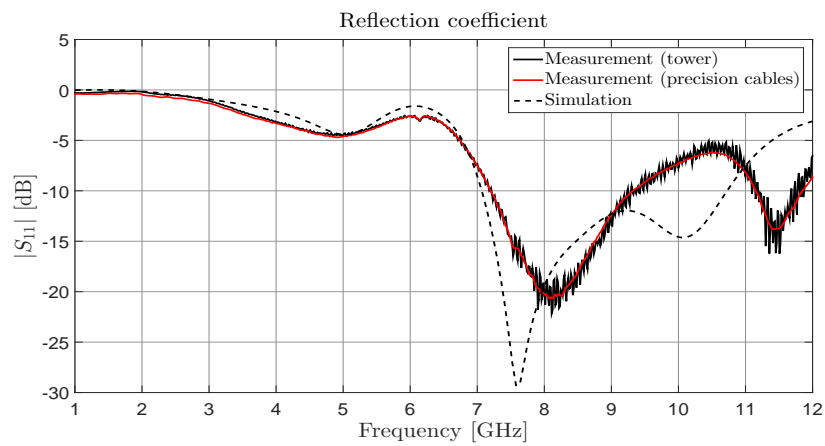
Figure 3.10: The measurement results. In Fig. (a) the reflection coefficient of the horn antennas is presented. In Fig. (b) the determined path loss with the calculated free space path loss is presented.

### 3 Realization and characterization of the designed UWB antennas



**Figure 3.11:** The measurement setup with the monopole antenna. The monopole is oriented with the patch toward the horn and with the ground plane toward the horn.

(a)



(b)

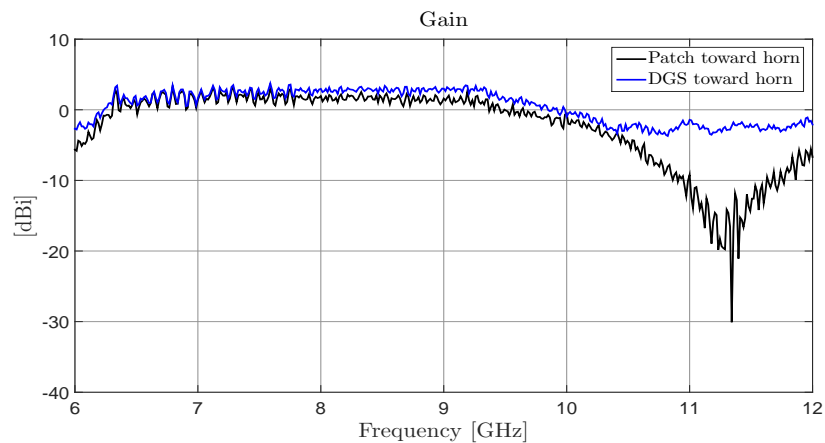


**Figure 3.12:** The measurement results. In Fig. (a) the reflection coefficient of the monopole antenna is presented. In Fig. (b) the determined gain of the monopole antenna is presented.

### 3.2 Reflection coefficient and gain of the realized antennas

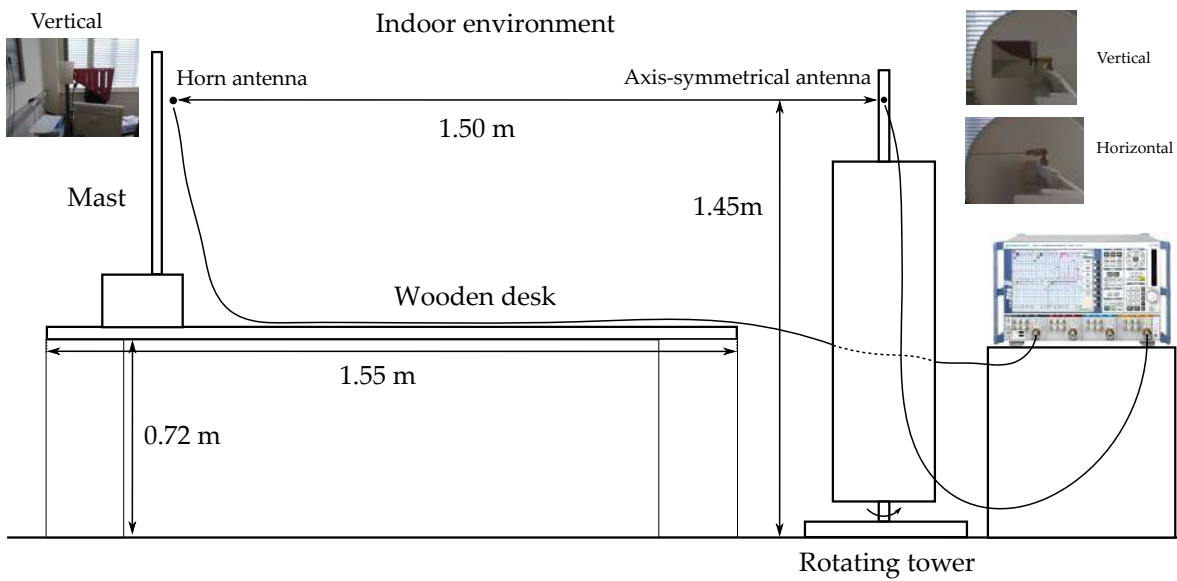
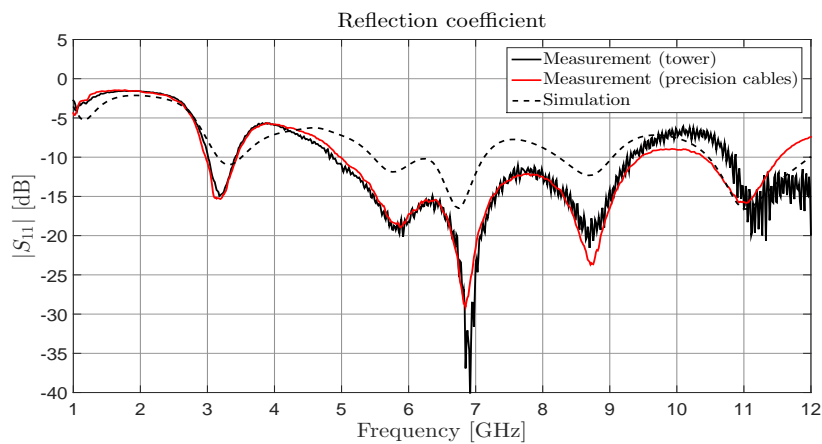


**Figure 3.13:** The measurement setup with the axis-symmetrical self-complementary antenna. The antenna is oriented vertical and horizontal.

(a)



(b)

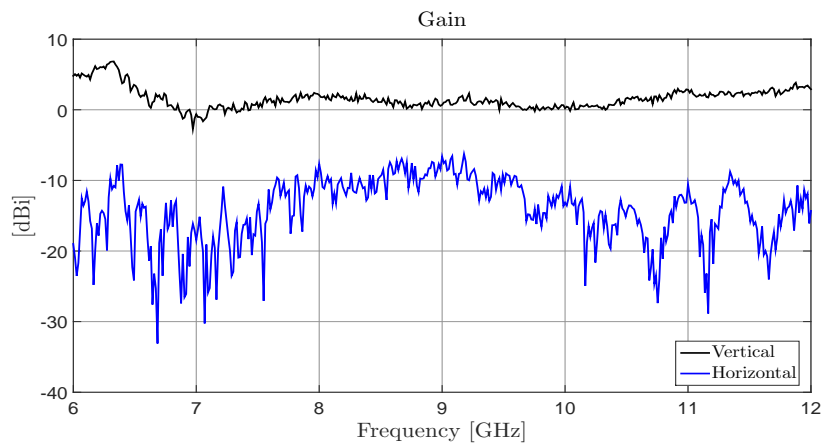


**Figure 3.14:** The measurement results. In Fig. (a) the reflection coefficient of the axis-symmetrical self-complementary antenna is presented. In Fig. (b) its determined gain is presented.

### 3 Realization and characterization of the designed UWB antennas

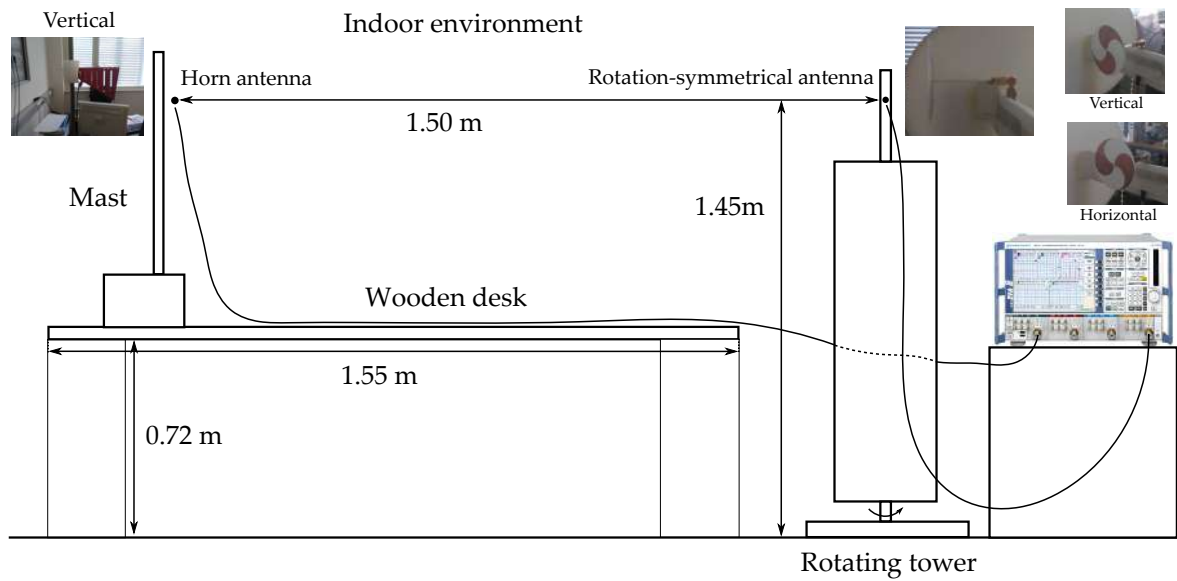
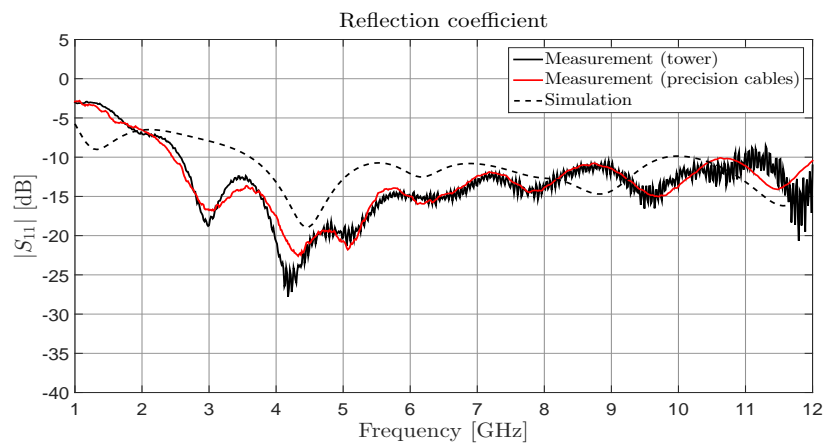


**Figure 3.15:** The measurement setup with the rotation-symmetrical self-complementary antenna. The antenna is oriented vertical and horizontal.

(a)



(b)

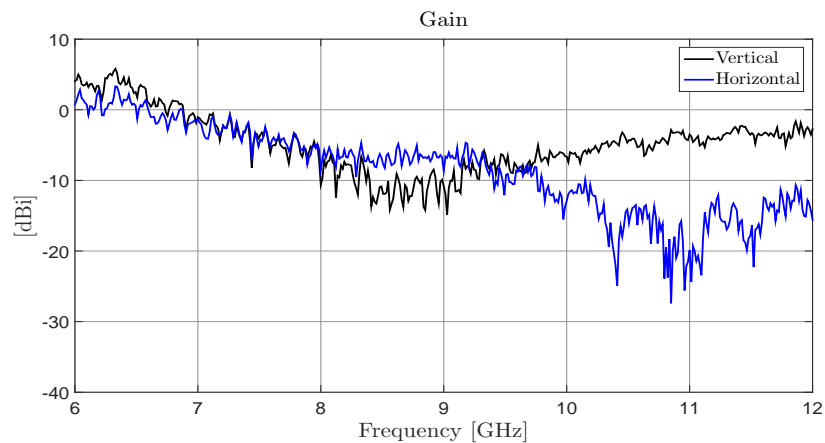


**Figure 3.16:** The measurement results. In Fig. (a) the reflection coefficient of the axis-symmetrical self-complementary antenna is presented. In Fig. (b) its determined gain is presented.



From the results regarding the gain the monopole antenna presents the most favorable gain while the rotation-symmetrical antenna the most disadvantageous. The ground plane makes a difference although both antennas radiate toward the horn and opposite from the horn. The gain of the rotation-symmetrical antenna may be improved by adding a wide band reflector which it is not seen as a trivial task due to the presence of the balun structure. The balun structure is likely to absorb some of the radiation that is reflected from the reflector at different frequencies. This will cause local minimum points for the gain in the main direction over frequency.

The rotation-symmetrical self-complementary antenna is mechanically instable. The radiation structure does not hold on to the microstrip balun for a long time. This is because the copper foil at the output of the microstrip balun, which has a very small width, has a very weak adherence with the substrate. The small width is necessary to satisfy the high impedance requirement at the output. The solder is too strong and causes a high strain on the copper foil that eventually will result in a weakening of its adherence to the substrate. This problem can be combated in the future if the antenna is designed for low impedance values, for example  $100 \Omega$  instead of  $150 \Omega$ . This will result finally in wider strip widths at the output of the balun. Another possible way to decrease the impedance of the antenna is by increasing the substrate height.

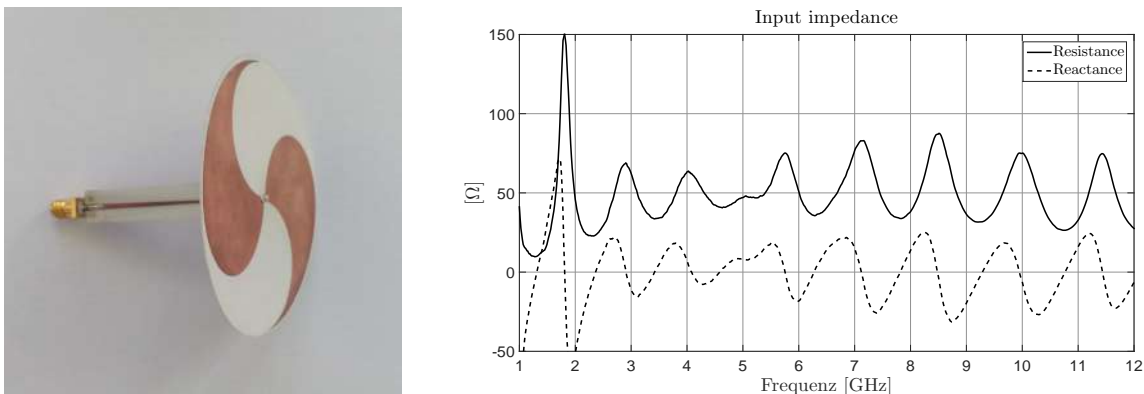


**Figure 3.17:** The measured input impedance of the rotation-symmetrical self-complementary antenna attached to the microstrip balun.

Fig. 3.17 presents the rotation-symmetrical self-complementary antenna attached to the balun and its measured input impedance. The measurements were performed on a wooden desk. For this measurement the network analyzer ZVA24 and precision cables were used. As can be seen, the impedance is not constant in the frequency band of operation and has a complex value. The values of the resistance are between  $31.7$  and  $87.0 \Omega$ , and the values of the reactance are between  $24.9$  and  $-30.0 \Omega$  in the frequency band from  $3.1$  and  $10.6$  GHz. The resistance is low as  $50 \Omega$  due to the transformation of the balun. When the relation for the input impedance of the self-complementary structure was derived in section 2.2 the presence of medium was not taken into consideration. The relation was obtained strictly using the knowledge about the distribution of the electromagnetic fields in the far field and the conservation law. In a realistic scenario the medium determines the wave impedance of a structure. Its distribution over the geometry of the structure is one of the factors that determines the input impedance of the structure as can be seen from relation 2.12 from section 2.5.

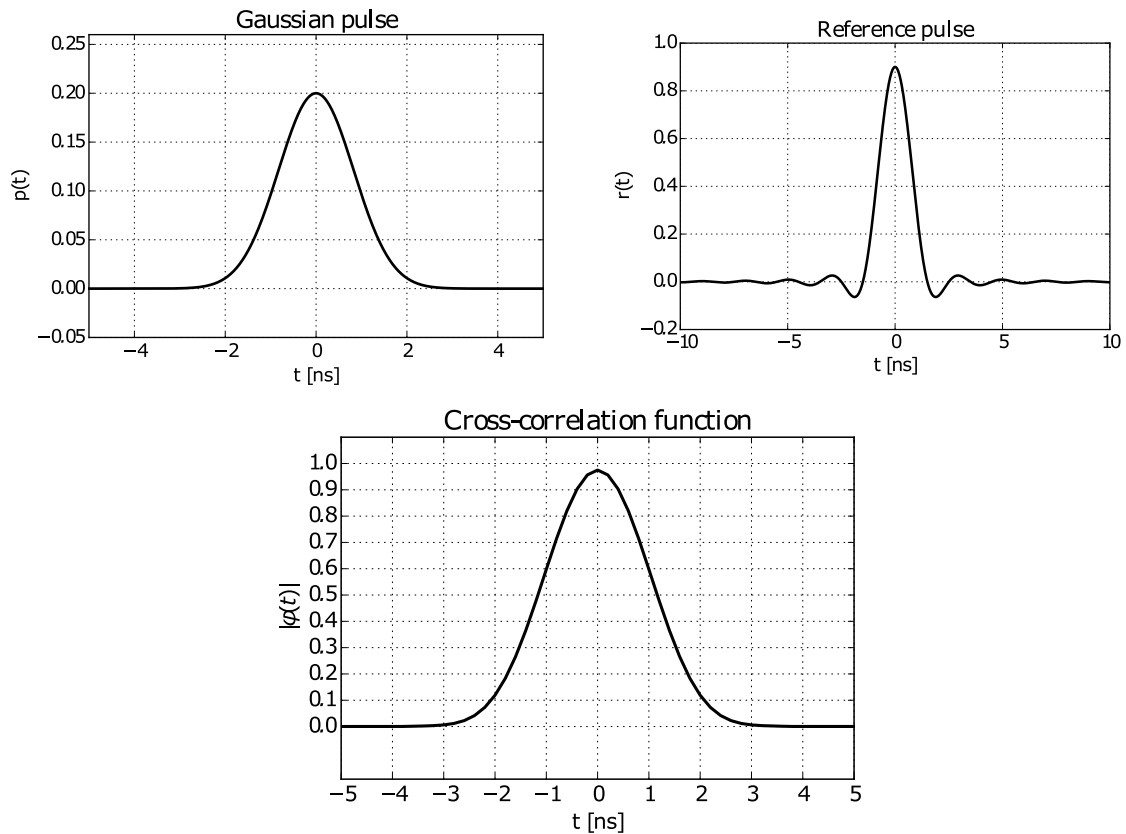


**Figure 3.18:** The compliance verification of a UWB baseband pulse recommended by ETSI with the IEEE 802.15.4a standard. The Gaussian pulse has a peak value of 0.2 and a -10 dB bandwidth in terms of power spectral density of 500 MHz. The reference pulse is a root raised cosine with a pulse duration of 2.0 ns and a roll off factor of 1.0. The ordinate is normalized and can be given, for example, in millivolts.

### 3.3 UWB test signal design and realization

In order to test the behavior of the antenna in the time domain a test pulse is required. Specifically of interest is the behavior regarding the temporal dispersion. The transmitted UWB pulse is formed of sine waves in a bandwidth of 500 MHz around a center frequency. Temporal dispersion means that the pulse is widened due to the different propagation velocities of the sine waves. It is interesting to study if the difference in propagation velocities comes from the antenna structure. This chapter deals with the design and realization of the test pulse followed in the next chapter by time domain measurements.

The design of the test pulse must be in agreement with the pulses used in commercial available UWB systems because otherwise the results of test will be meaningless. For this purpose the IEEE 802.15.4a standard [35] and a technical report from ETSI [44] regarding the UWB signal characteristics are used as references. The standard has precedence over the technical report. The requirements from the technical report are not mandatory while the requirements from the standard are mandatory. Both references have in common the fact that requirements refer to the UWB baseband impulse response, that being the envelope of the UWB pulse.

The IEEE 802.15.4a standard states that the pulse shape of the UWB signal must be constrained by the shape of the cross-correlation function. The cross-correlation function is built

between the UWB pulse and a reference pulse. The reference pulse is a root raised cosine pulse with a roll off factor of 0.6. The standard specifies constraints also on the reference pulse. These constraints regard the reference pulse duration and its main lobe width, and depend on the communication channel. For example, for channel 9, which is a mandatory channel, the reference pulse duration is 2.0 ns and the reference main lobe width is 0.5 ns. The designed UWB pulse is compliant with the standard if the main lobe values of the cross-correlation function are higher than 0.8 within the main lobe width and if the side lobes of the cross-correlation function are less than 0.3. The cross-correlation function is used to measure the similarity between the designed UWB pulse and the reference pulse.

The ETSI technical report recommends that the pulse envelope is to be defined by the following function:  $V_0 e^{-(q B_W t)^2}$ .  $V_0$  is the peak amplitude,  $B_W$  is the -10 dB signal bandwidth in terms of power spectral density and  $q$  is a constant factor and has a value of 1.4639. This recommendation states that the pulse width of the voltage pulse envelope is defined as the time in which the voltage pulse values are higher than 10 % of the voltage pulse peak value. As an example, for a UWB pulse having a bandwidth of 500 MHz the pulse width results in a value around 4.0 ns.

Fig. 3.18<sup>1</sup> shows that the recommendation of ETSI is compliant with the IEEE standard. The cross-correlation of a Gaussian pulse with the reference pulse, in this case a root raised cosine pulse, results also in a Gaussian pulse. This offers flexibility for the design of the Gaussian pulse. It is to note that the recommendation from ETSI does not constrain the pulse width of the system. It is not mandatory to design a pulse with the pulse width equal the reference pulse width, for example 2.0 ns for channel 9. The IEEE standard places constraints only on the cross-correlation function and the reference pulse, that is on the main lobe and side lobes of the UWB pulse. This observation is important because it offers a degree of flexibility in designing the UWB transceiver.

The UWB pulse can be realized by means of analog techniques using a rectangular signal as an impulse and a low pass filter, like for example a Butterworth filter. In this case the cross-correlation function will contain side lobes. In order that the signal can be transmitted, it needs to be shifted in frequency with a carrier signal. The IEEE standard contains a more comprehensive description on how to design a transceiver. The implementation can be done analog, digital or mixed. An example was already presented in section 1.1 in Fig. 1.2.

### 3.4 Time domain measurements

In Fig. 3.19 the measurement setup for the time domain measurement conducted in this work is presented. The instruments used in the setup are the digital storage oscilloscope Infiniium DSO91204A, used to capture the received signal, the arbitrary waveform generator (AWG) M8195A, used to generate the UWB test signal and the trigger signal for the oscilloscope, and the 33500B series wave generator (WG) used to generate the trigger signal for the AWG. The trigger signal for the oscilloscope is generated by using the marker technology supported by the AWG. The clock 10 MHz oscillator of the oscilloscope is used to provide the AWG with the clock signal.

<sup>1</sup>It has come to the attention that the reference pulse shape defined by IEEE resembles a root raised cosine pulse if the roll off factor in the definition is substituted with 1.0 and if the pulse is inverted. An example a root raised cosine pulse can be found in [16].

### 3 Realization and characterization of the designed UWB antennas

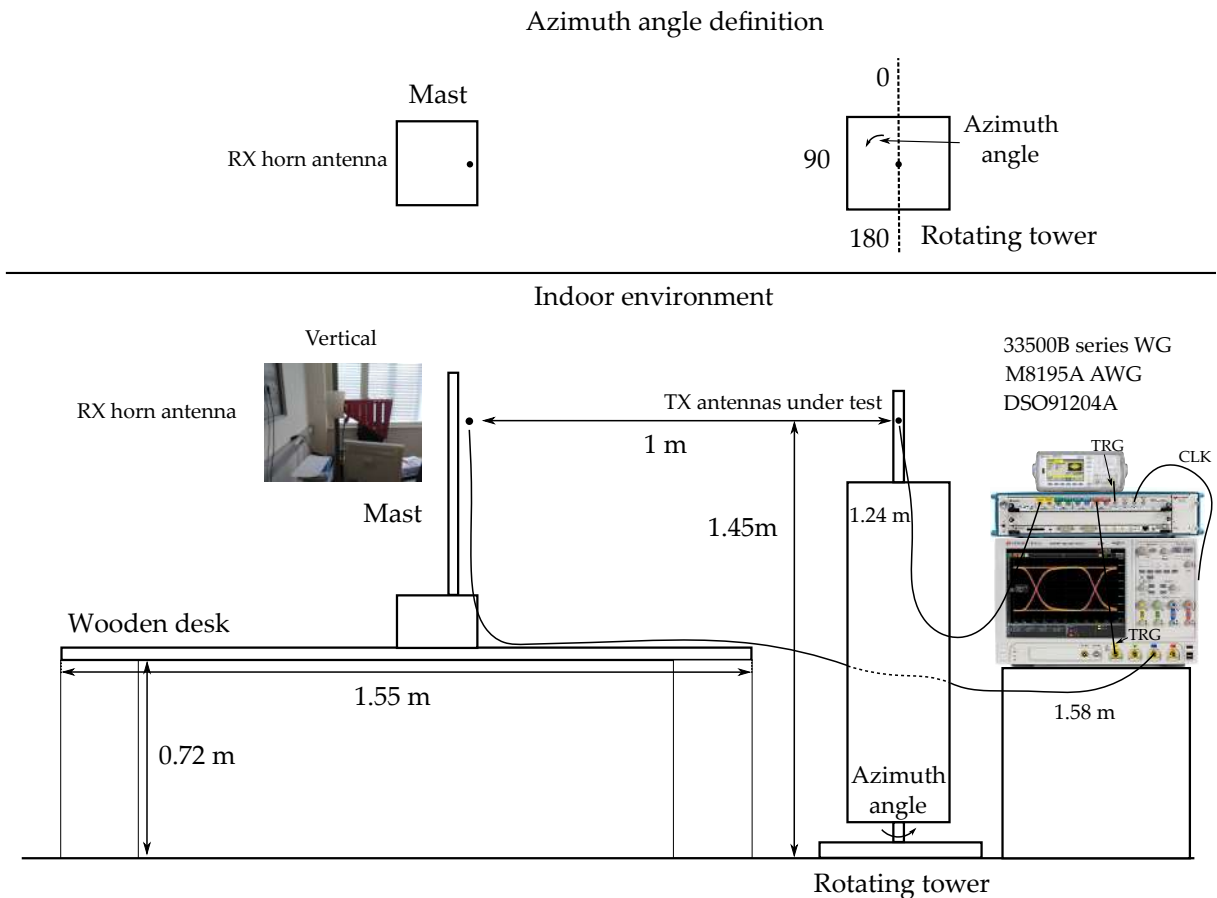


**Figure 3.19:** The measurement setup for the time domain measurement.

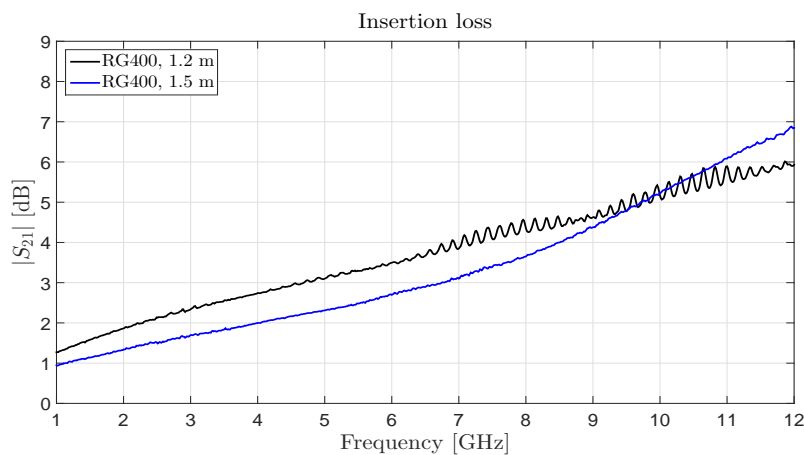


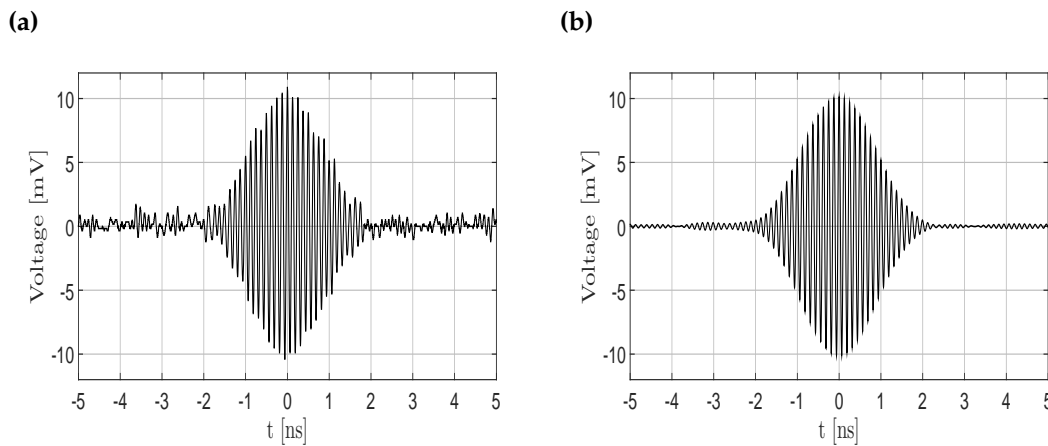
**Figure 3.20:** The insertion loss of the cables used for the time domain measurements. The power level of the network analyzer is 0 dBm.

The coaxial cables used are of standard RG400 and their insertion loss are presented in Fig. 3.20. For example at 8 GHz the 1.5 m coaxial cable has an insertion loss of 3.7 dB or 2.34 dB/m. The 1.2 m cable was chosen to connect the antenna mounted on the rotating tower because it has a higher flexibility than the 1.5 m cable. The disadvantage is that the 1.2 m shows a higher insertion loss than the 1.5 m cable because the cable is thinner. The ripples are caused

by an adapter used to connect two 0.6 m cables to obtain a 1.2 m cable. The antennas under test are the horn antenna, the same type used for the receive antenna, the monopole and the axis-symmetrical self-complementary antenna. The rotation-symmetrical antenna was not used because its high mechanical sensitivity.

It is to observe in Fig. 3.19 that the measurement is done for a distance of 1.0 m between the antennas. The 1.5 m distance was not chosen because at 1.5 m distance the pulse signal was strongly covered by noise. The measurements could not have been performed accurately at this distance. A solution to this problem would have been to use a wide band low noise amplifier (LNA) between the oscilloscope and the receive antenna. The tower has an azimuth step motor that allows it to rotate. The azimuth step motor of the tower is controlled remotely. The azimuth angle of the tower is varied between 0 and 180 degrees as showed in Fig. 3.19 and the time behavior of the channel is observed. As mentioned in chapter 1.1, the UWB antenna is considered as part of the channel.

For the post-processing of the pulse an ad hoc digital emulator for an RF chain was designed. This emulator is composed of a filter, amplifier and a mixer. These blocks can be used repeatedly during the post-processing, For example, the filter can be used as a pre-selection and a bandpass filter. The filter and amplifier is based on the fast Fourier transformation (FFT) while the mixer is based on multiplication in time domain. The amplifier was used also to compensate the cable and the path loss from Fig. 3.19.



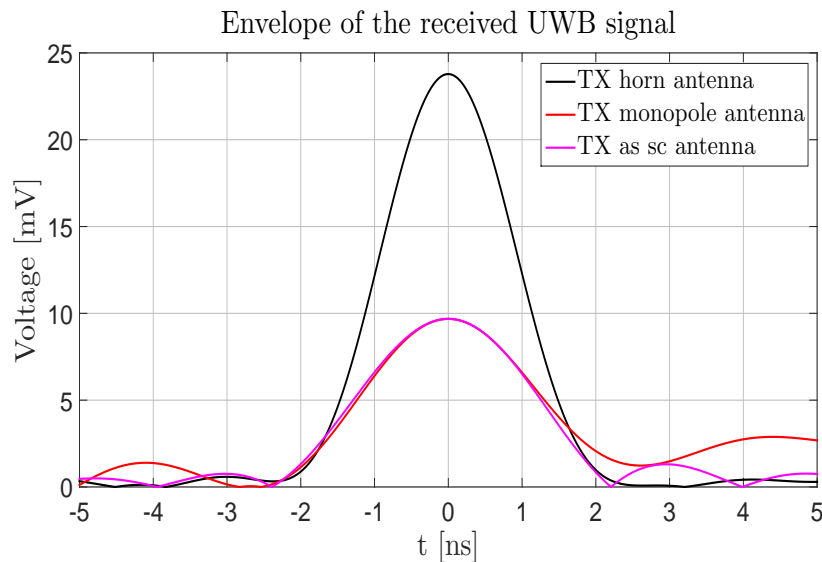
**Figure 3.21:** UWB test signal. In Fig. (a) the realized UWB test signal is presented. This signal was measured at the port of horn antenna placed on the mast in Fig. 3.19. In Fig. (b) the filtered version of the signal from Fig. (a) is presented.

Fig. 3.21a shows the realized pulse, measured at the horn antenna on the mast in Fig. 3.19. As a transmit antenna a similar horn antennas was used is in Fig. 3.9. The peak value of the transmitted pulse is chosen 500 mV. This value was chosen because it is close to the value used in the commercial UWB systems, that is 200 mV, but at the same time ensures that the measurement can be performed accurately at 1.0 m without the use of amplifiers. The center frequency used is 7.9872 GHz, which corresponds to channel 9<sup>2</sup> from the IEEE 802.15.4a standard. The

<sup>2</sup>Channel 9 is the mandatory channel in the high frequency band. The high frequency band is delimited by channel 5, 6.4896 GHz, and channel 15, 9.4848 GHz.

### 3 Realization and characterization of the designed UWB antennas

pulse values were not compensated with the cable losses to emphasize the total losses in the system, which amount to 34.0 dB. With this information and with the cable losses from 3.20 the path loss at 1.0 m is estimated to 26.7 dB. Fig. 3.21b shows the filtered version of the pulse from 3.21a. The pulse in Fig. 3.21 presents low distortion and good agreement the IEEE 802.15.4a standard. This pulse is therefore used in the following as reference pulse.



**Figure 3.22:** The envelope of received UWB signal with the horn, monopole and axis-symmetrical self-complementary antenna used as transmit antennas in Fig. 3.19. The azimuth angle is 90 degrees, the carrier frequency is 7.9872 GHz and the peak value of the transmitted signal is 500 mV.

In Fig. 3.22 the envelope of the received signal with the horn antenna, monopole antenna and axis symmetrical self-complementary antenna used as antennas under test in Fig. 3.19, and with the same signal parameters as those used in 3.21. In this case the signal was corrected with the cable losses in order to distinguish the main lobe from the side lobes. The side lobes stem from the down conversion in conjunction with the band pass filtering. The azimuth angle was chosen to be 90 degrees which means that the transmit and the receive antenna are in line of sight. This choice was made because the peak value of the received signal is maximum at this angle in comparison to other angles and thus the measurement is the most accurate at this angle. From Fig. 3.22 it is seen that the signal does not present any temporal dispersion. This means that neither the antenna nor the channel causes any dispersion on the signal when the setup in 3.19 is used. This result does not exclude dispersion at other frequencies. In order to observe temporal dispersion at other frequencies a frequency sweep may be performed. This is left for future work.

With the purpose to obtain information concerning the sight of the antennas a azimuth angle sweep between 0 and 180 degree was performed. The results are presented in Fig. 3.23. These angles were chosen because a very small signal is expected for the horn and the axis-symmetrical antenna in the azimuth angle range between 180 and 360 degree. In order to compare the measurements with each other also for the monopole antenna the same angle range was used although for the monopole a high signal strength is expected for the angle range 180 and 360 degree. The signal parameters are the same as those used for Fig. 3.22. What is seen in Fig. 3.23 is the absolute value of the filtered received signal. The values of the signal were

compensated with the cable losses. From these results it is concluded that the horn antenna has the smallest sight while the monopole antenna has the largest sight. The monopole has the largest sight because the monopole antennas are omnidirectional. On other hand the horn antennas have a high directivity. The sight of the axis-symmetrical self-complementary antenna shows the highest uniformity in the line of sight regarding the pulse width. The slot of this antenna ensures that the electric field maintains its vertical polarization in the proximity of the radiating system. The knowledge gained from this experiment is that the two antennas, the monopole and the axis-symmetrical self-complementary antennas, are guaranteed to function properly at distances bellow 1 m between the transmitter and receiver with a satisfiable antenna sight assuming that no amplifier is used in the transmitter and receiver. Because of the measurement cables involved, which have the losses showed in 3.20, the same performance is not guaranteed at distances higher than 1 m. If a power amplifier is used in the transmitter and a LNA is used in the receiver, then higher distances may be achieved, for example as high as 35 m if the transmission takes place on channel 7 [34].

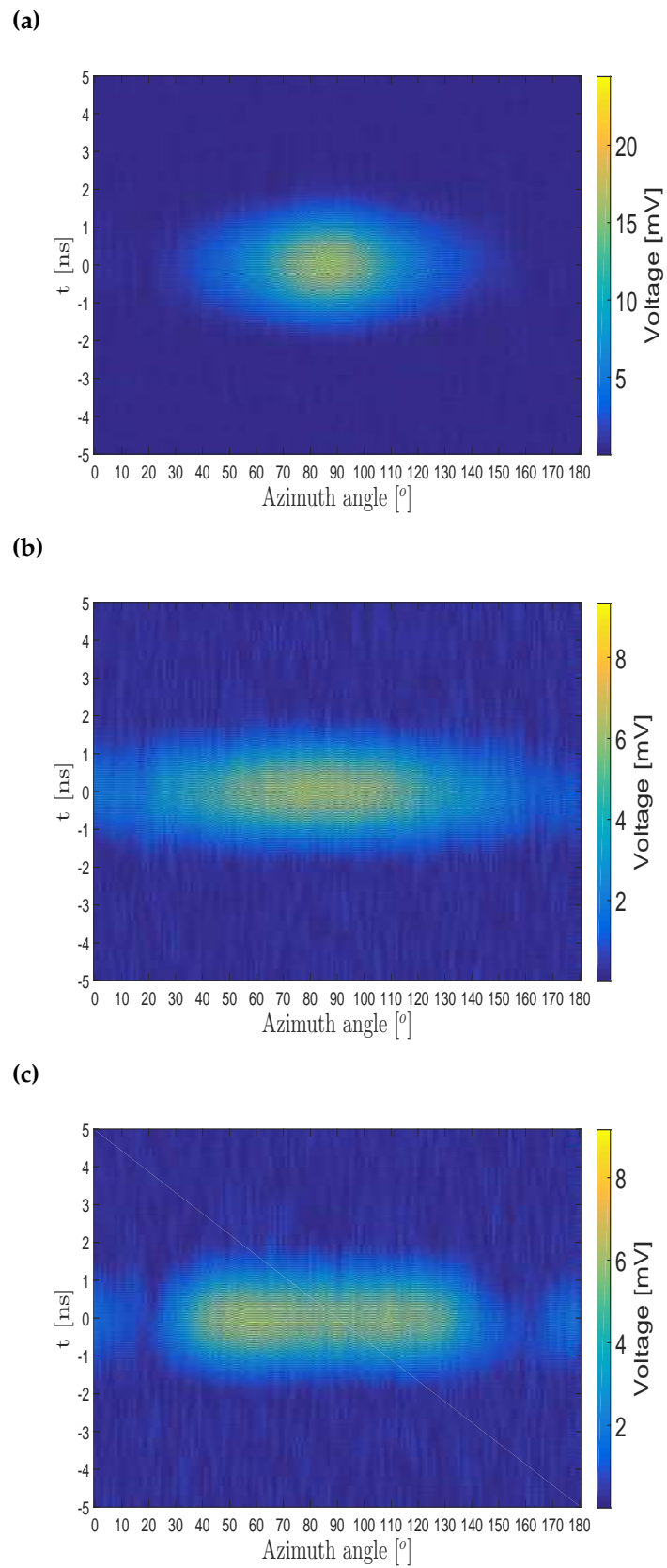


**Figure 3.23:** The measurement results for different azimuth angles. In Fig. (a) the horn antenna is used as TX antenna. In Fig. (b) the monopole is used as TX antenna with the DGS toward the horn. In Fig. (c) the axis-symmetrical self-complementary antenna with vertical polarization is used as TX antenna.



## 4 Summary

In this work self-complementary antennas for use in UWB systems were studied both from a theoretical and a practical point of view. At first, two principles were introduced. These principles guide the antenna designer in fulfilling the goals of the design. Afterwards, three types of self-complementary antennas were introduced. It was proposed in this work to construct these antennas using symmetry operations, for example, translation, rotation reflection and inversion. These symmetry operations are consistent with the 3D - modelers in simulation tools and with the operations used by the gerber standard. Additionally a balun was needed for the rotation-symmetrical self-complementary antenna. This balun was designed in microstrip technology.

The simulator was used in order to improve the design of the antennas and to verify their electromagnetic properties. Before using the simulator some test structures were studied in order to understand the behavior of the simulator. By the use of the simulator it was possible to select the shape of the antenna structures for prototyping.

It was observed that other known UWB antennas do satisfy the self-complementary principle if their geometry fulfills certain conditions, like for example the apex angle of the bow tie antenna should be 90 degrees.

Prototypes for the designed antennas were realized and measured. Before the actual measurements were conducted on the prototypes, some observations were made for the microstrip balun and for the measurement accuracy. The measurement results for the microstrip balun presented good agreement with the design. The achieved impedance at the output was only  $8 \Omega$  less than the goal. A redesign of the balun with a smaller width of the strip at the output would increase the output impedance. The influence of the SMA connector stubs and of the small ground plane on the measurement accuracy was also studied. It was observed that in order to achieve accurate measurements the SMA connector stubs on the top needed to be removed or connected to ground through vias. The plane-symmetrical self-complementary antenna had a small ground plane. This antenna behaved like a symmetrical antenna. It was not possible to measure it accurately because of the cable currents, although the presented measurements of the reflection coefficient was satisfying. A solution to mitigate the cable currents was found by realizing out of this antenna a monopole by introducing in this case a round ground plane. Other solutions would have been to integrate a wide band balun in the feeding system during the design phase.

The measurements on the prototype were performed in an indoor environment. The indoor environment provides a realistic environment in which the antennas are tested. In comparison to the anechoic chamber the measurement in a indoor environment is less accurate due to the presence of scatterers. From the measurement results, the rotation-symmetrical self-complementary antenna showed the most satisfying results regarding the reflection coefficient

but poor results regarding the gain because of the lack of measurement accuracy. The measurement accuracy for this antenna at high frequencies for a source power level of 0 dBm was poor. This is because the used cables had a high insertion loss at high frequencies. A solution would have been to redo the measurements at a higher source power level. Regarding the reflection coefficient of all the designed antennas the measurement results were predicted relatively well by the simulation. Because the SMA connector was not used during the simulations, the simulation results deviated from the measurement results. The measurements results were better than the simulation results. Further, it was observed that the realized prototype for rotation-symmetrical self-complementary antenna was mechanically unstable after a period of time. This was because of the fact that the adhesion of the copper foil to the substrate was weakened by the strain produced by the solder. A redesign of the rotation-symmetrical self-complementary antenna with a lower input impedance, for example  $100 \Omega$ , would have solved this problem. This would have resulted in a larger strip width of the balun at the output. Finally the impedance of the rotation-symmetrical self-complementary antenna was presented. The impedance was not constant, it had a ripple of  $30 \Omega$  in the frequency band of operation. This is mainly because during the derivation of the self-complementarity principle the medium was not taken into account. This left an open door for future design refinement.

Measurements in time domain were also performed with the purpose to study the temporal dispersion of the channel and the sight of the antennas. In order to achieve this, a test signal was needed. The test signal was designed in order to comply with the IEEE 802.15.4a standard. The signal does not need to have the width equal to the reference pulse prescribed by the IEEE standard. The width may be higher than that of the reference signal. From this point of view the standard offers a degree of flexibility in designing the signal to accommodate the system environment. From the time domain measurements no dispersion was observed because on the one hand the distance between the antennas was small and on the other hand few dispersive materials were present on the channel. The test was done only at one carrier frequency. It remains for future work to perform measurements for a high number of carrier frequencies to achieve a higher yield. An angle sweep was performed in order to test the sight of the antennas. The monopole showed the largest sight because a monopole is an omnidirectional antenna. The sight of the axis-symmetrical self-complementary antenna was the most uniform due to the good polarisation of the radiating system.

Self-complementary antennas are a current subject of interest for the scientific community. It is hoped that the technique based on symmetry operations together with the results presented in this work offers a contribution on the self-complementary antennas to the antenna scientific community.

# A The duality principle and the origin of the magnetic currents

In the literature and scientific works the term magnetic current is encountered, for example in [2] and in [18]. It is not a coincidence that this term is encountered when the duality principle is also mentioned. Using the interpretation of Maxwell's equations from [8] and a transformation likewise from [8] called Fitzgerald-Transformation<sup>1</sup> the term magnetic current is explained.

The starting point are the two Maxwell equations, the local Faraday induction law and the local Ampere-Maxwell law:

$$\vec{\nabla} \times \vec{E} = -\partial_t \vec{B}, \quad (\text{A.1})$$

$$\vec{\nabla} \times \vec{H} = \vec{j} + \partial_t \vec{D}. \quad (\text{A.2})$$

The right sides represent vortex sources. For example the vortex source for the magnetic field is the charge current that flows and the fluctuation of the electric flux density also termed displacement current [7].

The Fitzgerald-Transformation is:

$$\vec{E} \rightarrow Z \vec{H}, \quad \vec{H} \rightarrow -\frac{\vec{E}}{Z}, \quad (\text{A.3})$$

$$\vec{B} \rightarrow -Z \vec{D}, \quad \vec{D} \rightarrow \frac{\vec{B}}{Z}. \quad (\text{A.4})$$

where  $Z$  is the medium wave impedance [5]. Assuming that the medium is homogeneous, linear, and isotropic the equations transform into

$$\vec{\nabla} \times \vec{H} = \partial_t \vec{D}, \quad (\text{A.5})$$

$$\vec{\nabla} \times \vec{E} = -(Z \vec{j}) - \partial_t \vec{B}. \quad (\text{A.6})$$

The new term that is present on the right side of the second equation is called magnetic current and represents a source of the electric field. It is to observe that this term has the dimension of voltage divided by surface. The magnetic current has no physical meaning. It is the result of applying the duality principle on the Maxwell's equations.

<sup>1</sup>The transformation is named after the Irish physicist George Francis Fitzgerald (1851-1901).

The same observation is experienced if the two wave equations, namely the wave equation for the electric field strength and the wave equation for the magnetic field strength, applied to an homogeneous, linear and isotropic material, are transformed using the same transformation:

$$\Delta \vec{E} - \frac{1}{c} \partial_t^2 \vec{E} = \vec{\nabla} \left( \frac{\rho}{\epsilon} \right) + \mu \partial_t \vec{J}, \quad \Delta \vec{H} - \frac{1}{c} \partial_t^2 \vec{H} = \vec{\nabla} \left( \frac{\rho}{\epsilon Z} \right) + \mu \partial_t \left( \frac{\vec{J}}{Z} \right), \quad (\text{A.7})$$

$$\Delta \vec{H} - \frac{1}{c} \partial_t^2 \vec{H} = -\vec{\nabla} \times \vec{J}, \quad \Delta \vec{E} - \frac{1}{c} \partial_t^2 \vec{E} = \vec{\nabla} \times (Z \vec{J}). \quad (\text{A.8})$$

These observations offer another point of view for the same problem with the same results. For example an electric dipole can be replaced with an (equivalent) magnetic dipole that radiates the same power as the electric dipole. Another example of the use for the duality principle is to be found in [1] where in the transformation the velocity is used and not the characteristic wave impedance.

In the above equations  $\Delta$  means the Laplace-operator,  $\partial_t$  means the partial derivative with respect with time,  $\rho$  is the electric charge density,  $\vec{J}$  is the electric current density,  $\epsilon$  is the permittivity of the material,  $\mu$  is the permeability of the material and  $c$  is the velocity of the wave in the material. For free space propagation the material parameters are replaced with the free space parameters and the source terms are set to zero.

## B The mean electromagnetic energy flux

The starting point for deriving a definition for the mean electromagnetic flux density is represented by the Poynting vector<sup>1</sup> as obtained from Maxwell's equations:

$$\vec{S} = \vec{E} \times \vec{H}. \quad (\text{B.1})$$

The electric field strength and the magnetic field strength depend both on a space coordinate, here denoted by  $\vec{r}$ , and a time coordinate, denoted by  $t$ . For the time behavior the fields are assigned an oscillation at a given angular frequency,  $\omega$ . The following expressions are used:

$$\vec{E} = \vec{E}(\vec{r}) \cos(\omega t) = \text{Re} \left\{ \underline{\vec{E}}(\vec{r}) e^{j\omega t} \right\}, \quad (\text{B.2})$$

$$\vec{H} = \vec{H}(\vec{r}) \cos(\omega t) = \text{Re} \left\{ \underline{\vec{H}}(\vec{r}) e^{j\omega t} \right\}. \quad (\text{B.3})$$

The underline means that the respective quantity is a complex number and the operator  $\text{Re}\{\cdot\}$  gives the real part of a complex number. The expression for the Poynting vector becomes:

$$\begin{aligned} \vec{S} &= \text{Re} \left\{ \underline{\vec{E}} e^{j\omega t} \right\} \times \text{Re} \left\{ \underline{\vec{H}} e^{j\omega t} \right\} \\ &= \left( \frac{\underline{\vec{E}} e^{j\omega t} + \underline{\vec{E}}^* e^{-j\omega t}}{2} \right) \times \left( \frac{\underline{\vec{H}} e^{j\omega t} + \underline{\vec{H}}^* e^{-j\omega t}}{2} \right) \\ &= \left( \frac{(\underline{\vec{E}} \times \underline{\vec{H}}^*) + (\underline{\vec{E}} \times \underline{\vec{H}}^*)^*}{2} \right) + \left( \frac{(\underline{\vec{E}} \times \underline{\vec{H}}) e^{j2\omega t} + ((\underline{\vec{E}} \times \underline{\vec{H}}) e^{j2\omega t})^*}{2} \right) \\ &= \text{Re} \left\{ \frac{1}{2} (\underline{\vec{E}} \times \underline{\vec{H}}^*) \right\} + \text{Re} \left\{ \frac{1}{2} (\underline{\vec{E}} \times \underline{\vec{H}}) e^{j2\omega t} \right\}. \end{aligned} \quad (\text{B.4})$$

The first term is the mean value of the Poynting vector and the second term is the oscillating part of the Poynting vector. By defining a oriented surface  $\mathcal{A}$  on which the energy flux is distributed the mean power through the surface is defined as:

$$P_{\text{mean}} = \int_{\mathcal{A}} \vec{n} \cdot \vec{S}_{\text{mean}} dA = \int_{\mathcal{A}} \vec{n} \cdot \text{Re} \left\{ \frac{1}{2} (\underline{\vec{E}} \times \underline{\vec{H}}^*) \right\} dA. \quad (\text{B.5})$$

<sup>1</sup>The Poynting vector describes the energy flux density and was named after John Henry Poynting (1852 - 1914).

# C Reciprocity of a system comprising of two antennas

The problem regarding the reciprocity of a system is an interesting one. In a special case the reciprocity theorem states that if the cause and effect are interchanged in a system then the behavior of the system remains the same, if the reciprocity principle holds for that respective system. Deciding upon the reciprocity of a system is not an easy task but it has come to the attention from [13] that by answering one of the three questions it will be possible to decide upon the reciprocity of the system. After formulating the questions an attempt of answering them will be presented.

The three questions do not involve only the reciprocity property of the system but also the losslessness and the time reversibility property of the system. The losslessness property is in direct connection with the power conservation law. The time reversibility property holds for a system if the system is invariant due to time reversal. The three questions are formulated as follows:

Does losslessness and time reversibility imply reciprocity?

Does losslessness and reciprocity imply time reversibility?

Does reciprocity and time reversibility imply losslessness?

For the following argumentation that will follow, the references [7], [8],[10], [13] and [14] were studied. It is important to mention that these references were used also to check the consistency of the argumentation presented here.

The starting point is given by the representation of a general linear N-port system by using the scattering matrix and the normalized input and output power waves:

$$\mathbf{b} = \mathbf{S} \mathbf{a}. \quad (\text{C.1})$$

$\mathbf{a}$  is a  $N \times 1$  vector and contains the input normalized power waves,  $\mathbf{b}$  is a  $N \times 1$  vector and contains the output normalized power waves, and  $\mathbf{S}$  is a  $N \times N$  matrix and represents the scattering matrix of the system. A system comprising of 2 antennas is described using a  $2 \times 2$  scattering matrix. Assuming that the inverse of the scattering matrix exists and the time reversal of the system is defined by conjugating the scattering matrix the three mentioned system properties may be formulated as follows:

Losslessness:  
 $[\mathbf{S}^*]^T = \mathbf{S}^{-1}.$

Reciprocity:  
 $\mathbf{S}^T = \mathbf{S}.$

Time reversibility:  
 $\mathbf{S}^* = \mathbf{S}^{-1}.$

---

The operation represented by  $'^T'$  is the matrix transpose operation, the operation represented by  $'^*'$  is the conjugate complex operation and the operation represented by  $'^{-1}'$  is the matrix inverse operation. The scattering matrix of a lossless system is unitary. The scattering matrix of a reciprocal system is symmetric. The scattering matrix of the time reversed system is equal with the inverse of the scattering matrix of the initial system if the system is invariant to time reversal. From these definitions the above questions are formulated in the following way:

$$[\mathbf{S}^*]^T = \mathbf{S}^{-1} \quad \text{and} \quad \mathbf{S}^* = \mathbf{S}^{-1} \quad \stackrel{?}{\Rightarrow} \quad \mathbf{S}^T = \mathbf{S}. \quad (\text{C.2})$$

$$[\mathbf{S}^*]^T = \mathbf{S}^{-1} \quad \text{and} \quad \mathbf{S}^T = \mathbf{S} \quad \stackrel{?}{\Rightarrow} \quad \mathbf{S}^* = \mathbf{S}^{-1}. \quad (\text{C.3})$$

$$\mathbf{S}^T = \mathbf{S} \quad \text{and} \quad \mathbf{S}^* = \mathbf{S}^{-1} \quad \stackrel{?}{\Rightarrow} \quad [\mathbf{S}^*]^T = \mathbf{S}^{-1}. \quad (\text{C.4})$$

For the first question  $\mathbf{S}^*$  is substituted in the losslessness property with the expression gained from time reversibility of the system so that the following is obtained:

$$[\mathbf{S}^{-1}]^T = \mathbf{S}^{-1}. \quad (\text{C.5})$$

Interchanging  $'^T'$  with  $'^{-1}'$  results in

$$[\mathbf{S}^T]^{-1} = \mathbf{S}^{-1}. \quad (\text{C.6})$$

If the inverse matrices of two matrices are equal then the respective matrices are equal. The following expression is obtained:

$$[\mathbf{S}^T] = \mathbf{S}. \quad (\text{C.7})$$

The scattering matrix is symmetric, the system is reciprocal. This result is obtained also in [13] and in [14].

For the second question  $'^T'$  is interchanged with  $'^*'$  in the losslessness property and the following expression is obtained:

$$[\mathbf{S}^T]^* = \mathbf{S}^{-1}. \quad (\text{C.8})$$

The system is assumed reciprocal and  $\mathbf{S}^T$  is substituted with  $\mathbf{S}$  thus resulting in

$$\mathbf{S}^* = \mathbf{S}^{-1}. \quad (\text{C.9})$$

This is the time reversibility property. The system is invariant due to time reversal.

For the third question, starting from the fact that the system is reciprocal it means that also the time reversed system is reciprocal, if the system is invariant to time reversal as it is assumed true for answering this question. This is obtained by conjugating the reciprocity property which results in:

$$[\mathbf{S}^T]^* = \mathbf{S}^*. \quad (\text{C.10})$$

By substituting the time reversed system with the inverse of the scattering matrix it follows that

$$[\mathbf{S}^T]^* = \mathbf{S}^{-1}. \quad (\text{C.11})$$

Interchanging 'T' with '\*' the following equality is obtained:

$$[\mathbf{S}^*]^T = \mathbf{S}^{-1}. \quad (\text{C.12})$$

This is the losslessness property. The system is lossless.

The obtained observations from applying the matrix formalism are summarized as follows. If the system is lossless and invariant due to time reversal then this implies reciprocity on the system. If the system is lossless and reciprocal then this implies invariance of the system due to time reversal. If the system is reciprocal and invariant due to time reversal then this implies that the system is lossless. When one of the properties in the premise is not true then the implication is also not true.

It was mentioned during the argumentation of the third question that if a system is reciprocal its time reversed version is also reciprocal. The starting point for this demonstration is given by the reciprocity theorem as presented in [13], which it is assumed true for the system  $\mathbf{S}$ :

$$\mathbf{a}_{(a)}^T \mathbf{b}_{(b)} = \mathbf{b}_{(a)}^T \mathbf{a}_{(b)} \quad (\text{C.13})$$

$\mathbf{a}_{(a)}$  and  $\mathbf{a}_{(b)}$  are two input normalized power waves at the input of the system that differ through their distribution and have opposite angles of incidence [13].  $\mathbf{b}_{(a)}$  and  $\mathbf{b}_{(b)}$  are the corresponding output normalized power waves. The relation between them is given by  $\mathbf{b}_{(a, b)} = \mathbf{S} \mathbf{a}_{(a, b)}$ . Conjugating C.13 leads to

$$[\mathbf{a}_{(a)}^*]^T \mathbf{b}_{(b)}^* = [\mathbf{b}_{(a)}^*]^T \mathbf{a}_{(b)}^* \quad (\text{C.14})$$

The time reversed system takes the time reversed output normalized power waves of the initial system and transforms them into the time reversed input normalized power waves of the initial system if the system is invariant to time reversal. With  $\mathbf{a}_{(a, b)}^* \Rightarrow \mathbf{b}_{(a, b)}^*$ ,  $\mathbf{b}_{(a, b)}^* \Rightarrow \mathbf{a}_{(a, b)}$  and  $\mathbf{a}_{(a, b)} = \mathbf{S}^* \mathbf{b}_{(a, b)}$  the equality C.14 becomes:

$$\mathbf{b}_{(a)}^T \mathbf{S}^* \mathbf{b}_{(b)} = \mathbf{b}_{(a)}^T [\mathbf{S}^*]^T \mathbf{b}_{(b)} \quad (\text{C.15})$$

This statement stems from the reciprocity of the initial system, C.13, from which it can be concluded that this statement is also true. On the other hand this can be true only if the time reversed system is symmetric under the assumption that  $\mathbf{b}_{(a)}$  and  $\mathbf{b}_{(b)}$  are arbitrary. This means that the time reversed system must be reciprocal if the initial system is reciprocal.

In order to get an understanding of the presented results the time reversal and its effect on the electromagnetic field and on the matter must be understood. The time reversal may be seen as a symmetry operation, see [15], or as a transformation, both point of views being consistent with each other. It is important to understand that the transformation  $t \rightarrow -t$  is equivalent to the conjugate complex operation in the complex plane. This experience is gained from studying



---

the behavior of the solutions of the Maxwell's equations under the time reversal. Some results are shared for example in [13], [14].

To get another insight on the time reversal an interesting observation is presented. Assuming that a 2 port linear system, described by the  $2 \times 2$  scattering matrix, is lossless, one obtains the following equations:

$$S_{11}^* S_{11} + S_{21}^* S_{21} = 1, \quad (\text{C.16})$$

$$S_{11}^* S_{12} + S_{21}^* S_{22} = 0, \quad (\text{C.17})$$

$$S_{12}^* S_{11} + S_{22}^* S_{21} = 0, \quad (\text{C.18})$$

$$S_{12}^* S_{12} + S_{22}^* S_{22} = 1. \quad (\text{C.19})$$

Conjugating these equations results in

$$S_{11} S_{11}^* + S_{21} S_{21}^* = 1, \quad (\text{C.20})$$

$$S_{11} S_{12}^* + S_{21} S_{22}^* = 0, \quad (\text{C.21})$$

$$S_{12} S_{11}^* + S_{22} S_{21}^* = 0, \quad (\text{C.22})$$

$$S_{12} S_{12}^* + S_{22} S_{22}^* = 1. \quad (\text{C.23})$$

The system remains lossless if the time reversal transformation is applied on it. This observation is explained by the fact that transformations, variations, in time do not change the conservation of energy. The statement follows from the Noether theorems<sup>1</sup>, which relates symmetry operations with conservation laws from a general point of view.

Unfortunately there are some examples that contradict with the presented implication derived from the matrix formalism. One example is the Faraday isolator, a system that comes from the domain of the wave optics, see description in [14], and is based on the Faraday effect, an effect that rotates the polarization of the field. The same effect is also encountered in an antenna system if plasma, like for example the ionosphere, or a magnetic material is present on the channel. The Faraday isolator is invariant due to time reversal and may be assumed lossless. It turns out that this system is not reciprocal. In their nature, the three principles seem independent from each other. This contradiction with the derived implications is dubious and at the moment unexplained.

---

<sup>1</sup>The theorems were named after Emmy Noether (1882-1935), a German mathematician, and were first presented in her work entitled *Invariant Variational Problems* (ger. *Invariante Variationsprobleme*) in 1918.

# D The architecture of the implemented virtual instrumentation application

During the course of this work an application for virtual instrumentation was developed. The development was done in MATLAB<sup>®</sup>. The application is based mainly on mapping the SCPI commands of the instruments to commands of higher abstraction level. In the following figures the architecture of the application is presented. One of the goals was to structure the application in a way that it offers flexibility to change, for example change in the sense of easily adding user defined commands. This is the main reason why the application was structured using concise modules. Both data structures and objects are used during the development. Tests for the functions in which an algorithm is implemented are also present. Due to the MATLAB<sup>®</sup> framework for testing, the test cases are implemented using classes. Measurement data is stored in a database and accessed during the post-processing stage. The implementation of a GUI was deliberately omitted, at least in this presented version.

The motivation to write this application was to provide a custom software to assist the user during the measurements, for example providing a fast way to acquire the raw data from the instruments but at the same time offering the possibility to adapt the application to the users needs.

It is to keep in mind that the presented architecture describes a working version of an application and remains subject to change or improvements, for example if the user wants to add another instrument to the application. It is also important to note that this architecture may be implemented in any programming language, like for example C++, Java or Python. A prerequisite for this is that the libraries written in such languages must dispose of the technology for accessing the commercial instruments, like for example VISA.

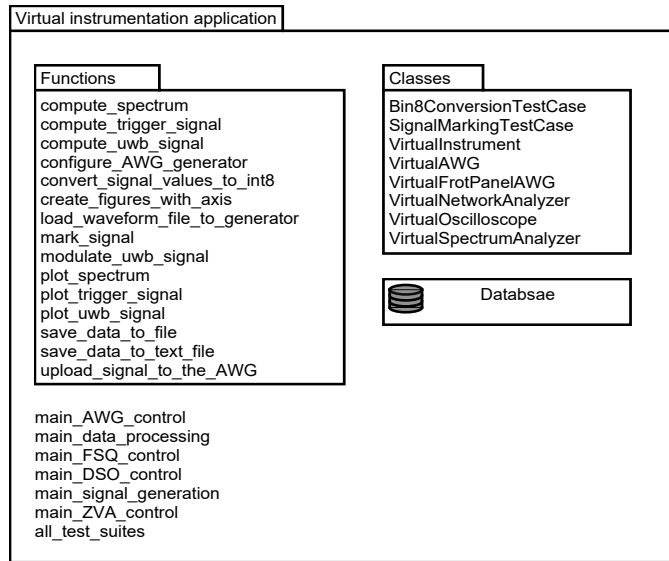


Figure D.1: The modules of the application.

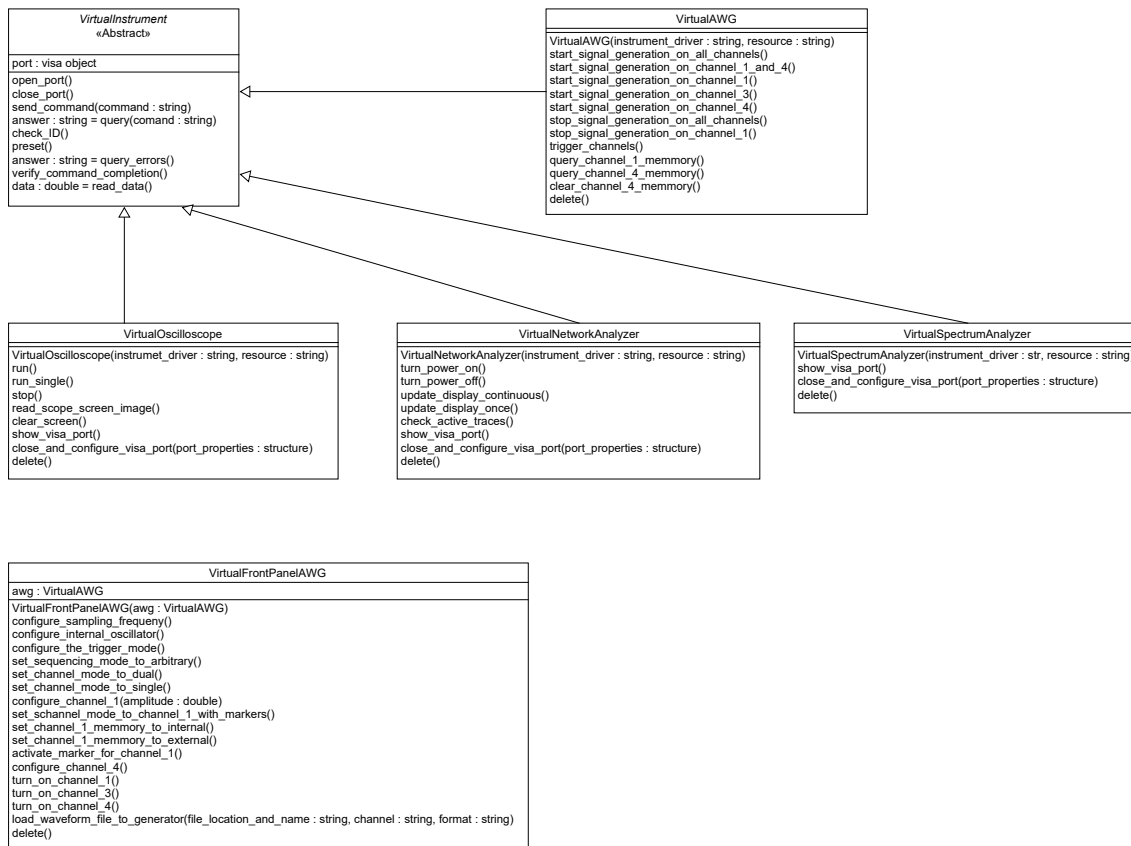


Figure D.2: The class diagram of the application.

## D The architecture of the implemented virtual instrumentation application

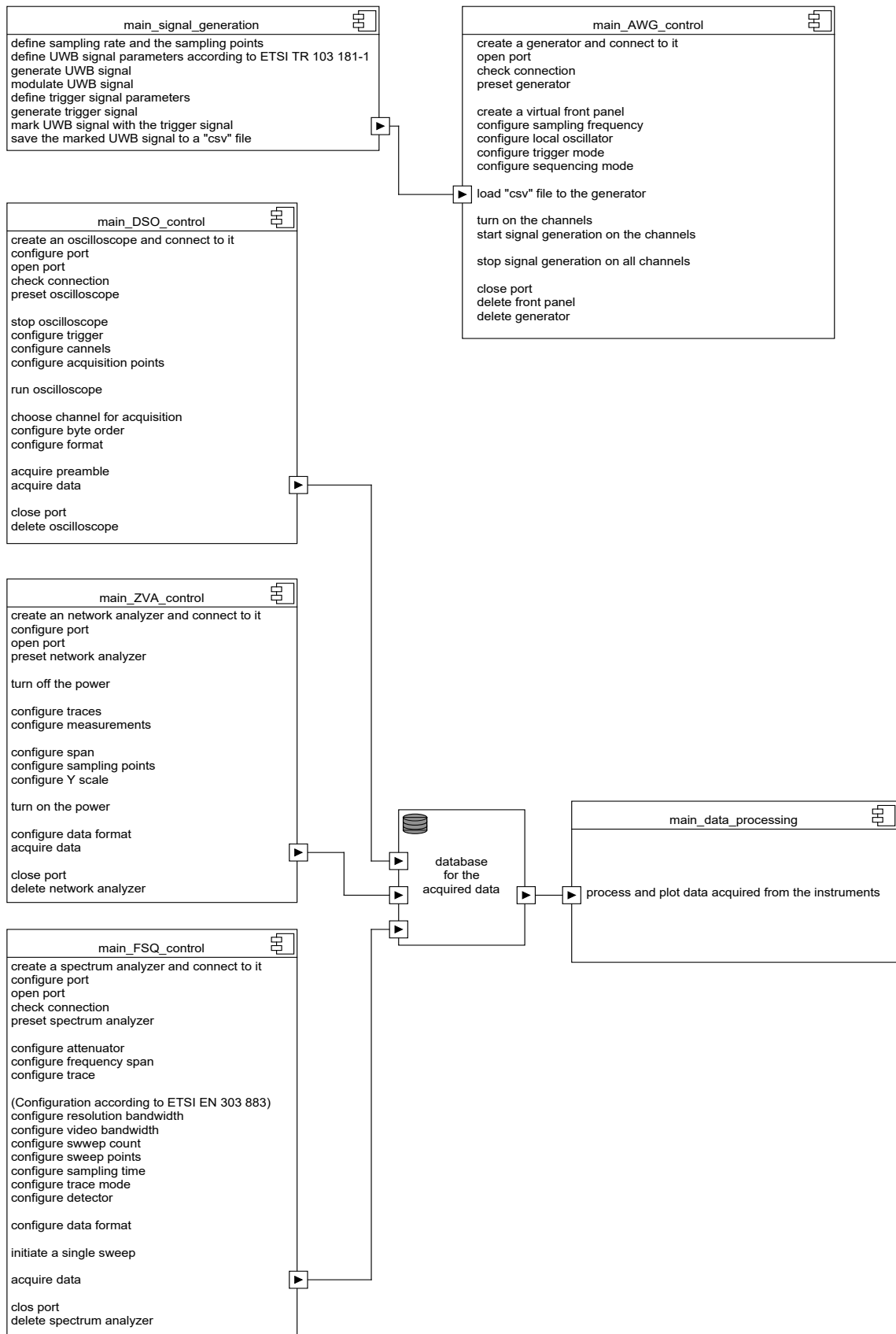


Figure D.3: An example for using the modules of the application from Fig. D.1.

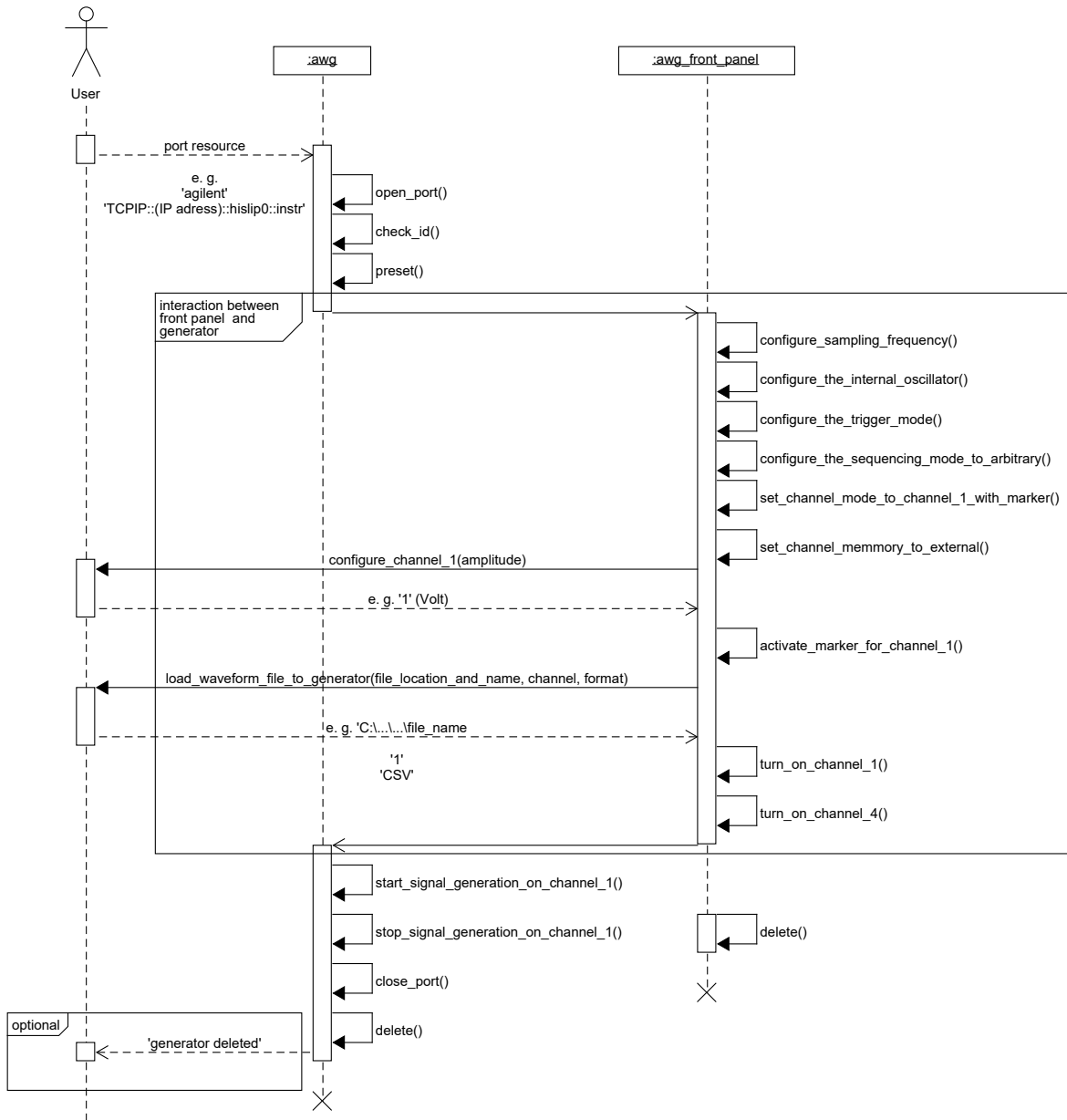


Figure D.4: An example for using the signal generator.

# References

## Books:

- [1] SCHANTZ H. G. *The Art and Science of Ultrawideband Antennas - Second Edition*. Artech House, Boston, U.S., 2015.
- [2] HEILMANN A. *Antennen III*. Bibliographisches Institut AG Hochschultaschenbücher, Mannheim, Germany, 1970.
- [3] VERDONE R. and ZANELLA A. (Editors). *Pervasive Mobile and Ambient Wireless Communications*. Springer, London, England, 2012.
- [4] SIWIAK K. and MCKEOWN D. *Ultra-Wideband Radio Technology*. John Wiley & Sons, Ltd, West Sussex, England, 2004.
- [5] MECKLENBRÄUKER C. and LASSER G. *Wellenausbreitung*. Institute of Telekommunikations, TU Wien, Wien, Österreich, 2013.
- [6] KRISCHKE A. and ROTHAMMEL K. *Rothammels Antennenbuch 13. Auflage 2013*. DARC Verlag GmbH, Baunatal, Deutschland, 2014.
- [7] PRECHTL A. *Vorlesungen über die Grundlagen der Elektrotechnik Band 2*. SpringerWien-NewYork, Wien, Österreich, 2008.
- [8] PRECHTL A. *Vorlesung über Elektrodynamik*. Institute of Electrodynamics, Microwave and Circuit Engineering, TU Wien, Wien, Österreich, 2010.
- [9] MOLISCH A. F. *Wireless Communications, second edition*. John Wiley & Sons Ltd ., U. S. A., 2011.
- [10] POZAR D. M. *Microwave Engineering, Fourth Edition*. John Wiley & Sons, Inc., University of Massachusetts at Amherst, 2011.
- [11] MONGIA R. K., BAHL I. J., BHARTIA P. and HONG J. *RF and Microwave Coupled-Line Circuits, Second Edition*. Artech House, Boston, London, 2007.
- [12] SEVICK J. *Transmission Line Transformers*, . Scitech publishing Inc., U. S. A., 2001.
- [13] HAUS H. A. *WAVES AND FIELDS IN OPTOELECTRONICS*. Prentice-Hall, Inc., Englewood Cliffs, New Jersey, 1984.
- [14] REIDER G. A. *Photonik, Eine Einführung in die Grundlagen, 3. Auflage*. Springer-Verlag Wien, Österreich, 2012.
- [15] FEYNMAN R. P., LEIGHTON R. B. and SANDS M. *The Feynmann lectures on physics: Mainly mechanics, radiation and heat*. Addison-Wesley Publishing Company, Inc., 1963.
- [16] GLOVER I. A. and GRANT P. M. *Digital Communications - Third Edition*. Prentice Hall, England, 2010.

---

## Scientific papers:

- [17] KLEMP O., SCHULTZ M. and EUL H. Novel Logarithmically periodic planar antennas for broadband polarization diversity reception. *International Journal AEU of Electronics and Communications*, 59:268–277, April 2005.
- [18] MUSHIAKE Y. Self-Complementary Antennas. *IEEE Antennas and Propagation Magazine*, 34:23–29, December 1992.
- [19] SIPAL V., JOHN M., NEIRYNCK D., MCCLAUGHLIN M. and AMMANN M. Advent of Practical UWB Localization: (R)Evolution in UWB Antenna Research. *Antennas and Propagation (EuCAP) 8<sup>th</sup> European Conference*, April 2014.
- [20] DUNCAN J. W. and MINERVA V. P. 100:1 Bandwidth Balun Transformer. *IRE Proceedings*, pages 156–164, October 1959.
- [21] CLIMER B. Analysis of suspended microstrip taper baluns. *IEE Proceedings*, 135:65–69, April 1988.
- [22] MÄKINEN R. M. and KELLOMÄKI T. Body Effects on Thin Single-Layer Slot, Self-Complementary, and Wire Antennas. *IEEE Transactions on Antennas and Propagation*, 62: 385–391, January 2014.
- [23] ANZAI D., KATSU K., CHAVEZ-SANTIAGO R., WANG Q., PLETTEMEIER D., WANG J. and BALASINGHAM I. Experimental Evaluation of Implant UWB-IR Transmission With Living Animal for Body Area Networks. *IEEE Transactions on Microwave Theory and Techniques*, 62: 183–191, January 2014.
- [24] GUO L., CHEN X. and CLIVE PARINI. Time Domain Behaviours of A Small Quasi-Self-Complementary UWB Antenna. *IEEE Microwave Technology and Computational Electromagnetics*, pages 66–69, November 2009.
- [25] ZHU X., YONGQIANG H., QUAN Y. and KECHU Y. A survey on impulse-radio UWB localization. *Science China Information Sciences*, 53:1322–1335, 2009.
- [26] GIBSON P. J. The Vivaldi Aerial. *Proceedings of the Ninth European Microwave Conference*.
- [27] LAMECKI A., BALEWSKI L. and MICHAL MROZOWSKI. An Efficient Framework For Fast Computer Aided Design of Microwave Circuits Based on the High-Order 3D Finite-Element Method. *Radioengineering, Proceedings of Czech and Slovak Technical Universities and URSI Committees*, 23:970–978, December 2014.
- [28] RUMSEY V. H. Frequency independent antennas. *Publisher or Institute*.
- [29] QING X., CHEN Z. N. and CHIA M. Y. W. Parametric Study of Ultra-Wideband Dual Elliptically Tapered Antipodal Slot Antenna. *Institute for Infocomm Research*.
- [30] LI S., WANG D., CAO W. and LI M. Design of Ultra-wideband bow-tie antenna in UHF band. *2016 11th International Symposium on Antennas, Propagation and EM Theory (ISAPE)*.

## Scientific works:

- [31] AYŞE ADALAN. Impulse Radio Ultra-Wideband Technology for Healthcare Applications. Doctoral thesis, Institute of Telecommunications, TU Wien, June 2013.

- [32] PHILIPP K. GENTNER. Compact On-Chip UWB Antennas for Short Range Connectivity. Doctoral thesis, Institute of Telecommunications, TU Wien, April 2013.
- [33] AMNOIY RUENGWAREE. Design of UWB Radar Sensors. Doctoral thesis, University of Kassel, November 2007.
- [34] DRAGOMIR CHINGOV. Ranging precision of an existing UWB transceiver with a custom designed antenna. Master thesis, Institute of Telecommunications, TU Wien, November 2016.

### **Standards:**

- [35] AMENDMENTS TO IEEE STD 802.15.4A. Part 15.4: Wireless Medium Access Control (MAC) and Physical Layer (PHY) Specifications for Low-Rate Wireless Personal Area Networks (WPANs). IEEE Computer Society, August 2007.
- [36] ETSI EN 302 065-1. Part 1: Requirements for Generic UWB applications. European Telecommunications Standards Institute, April 2014.
- [37] ETSI EN 303 883. Short Range Devices (SRD) using Ultra Wide Band (UWB); Measurement techniques. European Telecommunications Standards Institute, November 2016.
- [38] UCAMCO. The gerber file format specification. December 2016.

### **Patents:**

- [39] WILLIAM H. NESTER. Microstrip notch antenna. U.S. Patent 4,500,887, February 1985.
- [40] PHILIP S. CARTER. Wide band, short wave antenna and transmission line system. U. S. Patent 190,555, February 1938.

### **Miscellaneous:**

- [41] EUROPEAN COMMISSION. Commission Decision of 21 February 2007 on allowing the use of radio spectrum for equipment using ultra-wideband technology in a harmonised manner in the Community. Official Journal of the European Union, February 2007.
- [42] EUROPEAN CONFERENCE OF POSTAL AND TELECOMMUNICATIONS ADMINISTRATIONS. CEPT Report 45. CEPT, June 2013.
- [43] FEDERAL COMMUNICATIONS COMMISSION. First Report and Order. FCC, April 2002.
- [44] ETSI TR 103 181-1. Short Range Devices (SRD) using Ultra Wide Band (UWB); UWB signal characteristics and overview CEPT/ECC and EC regulation. European Telecommunications Standards Institute, July 2015.
- [45] ROGERS CORPORATION. RO400<sup>®</sup> Series High Frequency Circuit Materials. Data sheet, August 2015.
- [46] EVONIK RESOURCE EFFICIENCY GMBH. Rohacell<sup>®</sup> HF. Technical information, February 2017.
- [47] ANSOFT CORPORATION. High Frequency Structure Simulator. User's guide for software version 10, June 2005.
- [48] ÖVE. ÖVE Zeitschrift. Österreichischer Verband für Elektrotechnik, July 2016.



# List of acronyms

<b>Akronym</b>	<b>Meaning</b>
ANSYS	ANalysis SYStem
AOA	Angle of Arrival
AWG	Arbitrary Waveform Generator
BAN	Body Area Networks
CEPT	European Conference of Postal and Telecommunications Administrations
CLK	Clock signal
CMOS	Complementary Metal Oxide Semiconductor
DGS	Defected Ground Structure
DSO	Digital Storage Oscilloscope
EDA	Electronic Design Automation
EIRP	The equivalent isotropically radiated power
EN	European Norm
ETSI	European Telecommunications Standards Institute
FCC	Federal Communications Commission
FFT	Fast Fourier Transformation
GUI	Graphical User Interface
IEEE	Institute of Electrical and Electronics Engineers
HFSS	High Frequency Structure Simulator
IoT	Internet of Things
IR	Impulse-radio
LNA	Low Noise Amplifier
MAC	Medium Access Control
PEC	Perfect electric conductor

## List of acronyms

---

PHY	Physical layer
PPDU	PHY Protocol Data Unit
RF	Radio frequency
RX	Receiver
SDA	Serial Data Analyzer
SCPI	Standard Commands for Programmable Instruments
SFD	Start of Field Delimiter
SHR	Synchronization header
SMA	SubMiniature version A
TOA	Time of Arrival
TDOA	Time Difference of Arrival
TDR	Time Domain Reflectometry
TRG	Trigger signal
TX	Transmitter
UWB	Ultra-wideband
UHF	Ultra High Frequency
VISA	Virtual Instrument Software Architecture
VCO	Voltage Controlled Oscillator
VSWR	Voltage Standing Wave Ratio
WPAN	Wireless Personal Area Network

Hiermit erkläre ich, dass die vorliegende Arbeit gemäß dem Code of Conduct – Regeln zur Sicherung guter wissenschaftlicher Praxis, insbesondere ohne unzulässige Hilfe Dritter und ohne Benutzung anderer als der angegebenen Hilfsmittel, angefertigt wurde. Die aus anderen Quellen direkt oder indirekt übernommenen Daten und Konzepte sind unter Angabe der Quelle gekennzeichnet.

Die Arbeit wurde bisher weder im In- noch im Ausland in gleicher oder in ähnlicher Form in anderen Prüfungsverfahren vorgelegt.

Wien, June 7, 2017

Horia Botezan.